CRITICAL REVIEW

A comprehensive review on recent laser beam welding process: geometrical, metallurgical, and mechanical characteristic modeling

Seyedeh Fatemeh Nabavi[1] · Anooshiravan Farshidianfar[2] · Hamid Dalir[1]

Abstract

Demands for improved productivity, efficiency, and quality pose challenges to the welding industry, significantly the laser beam welding process. As the materials become increasingly sophisticated in their chemical composition to provide ever-better functionally specific properties, a more complete and precise understanding of how such materials can join for optimal effectiveness and efficiency will become essential. The objective of the present study is to review the current literature and discuss future trends. This thorough review study provides a comprehensive systematization and corresponding advances of constituent technologies on laser beam welding process modeling (LBWPM), including types of modeling including characteristics of weld joint (geometrical, metallurgical, and mechanical), monitoring (pre-process, in-process, and post-process), length scale (macroscale, mesoscale, and microscale), and approach of modeling (empirical-based and theoretical-based). The relevant case studies will be evaluated, discussed, and compared. In the end, the general trends, and strong indications of LBWPM, seen in the future, will be discussed. The current study also provides a good foundation for future research and creates awareness of the developmental direction of laser beam welding process modeling in manufacturing industries.

Keywords Laser beam welding process modeling (LBWPM) · Characteristic modeling · Geometrical · Metallurgical · Mechanical

1 Introduction

Permanent joining techniques such as welding are one of the critical and essential manufacturing methods that can be applied to improve product design and decrease production costs. However, it still meets many issues. Laser beam welding or LBW process, as a relatively newly developed method, with advantages of high accuracy, fast weld speed, and localized high concentrated heat input, has attracted tremendous interest in recent decades. The practical applications of this process in numerous industries (such as aerospace, automotive, shipbuilding) into various materials (including steels, titanium alloys, and aluminum alloys, and

different techniques (for instance, autogenous welding, laser-arc hybrid welding, and filler wire welding)) of LBW have been studied significantly [1].

A review on the recent progress in laser beam welding of magnesium alloys was provided by Cao et al. [2]. The microstructure and metallurgical defects encountered in laser beam welding process of magnesium alloys such as porosity, cracking, oxide inclusion, and loss of alloying elements were reviewed [2]. It also highlights the challenges associated with the weldability of magnesium alloys, indicating the need for further scientific investigation to address these issues. Thus, it can be inferred that the study conducted by Cao et al. did not include mechanical, metallurgical, and geometrical characteristic modeling of LBW. The current study, which is the subject of discussion, is focused on these aspects of LBW and aims to fill the gap left by the previous study.

In a comprehensive review conducted by Blackburn in 2012, LBW of titanium alloys, particularly for aerospace applications, was examined. Various aspects of LBW were explored, covering the operating principles and components of laser sources, including insights from quantum mechanics

✉ Seyedeh Fatemeh Nabavi
  snabavi@purdue.edu

✉ Hamid Dalir
  hdalir@purdue.edu

1   School of Mechanical Engineering, Purdue University, 585 Purdue Mall, West Lafayette, IN 47907, USA

2   Toronto M5S 3G8, Canada

and molecular vibration formulas [3]. Key characteristics of laser light, such as its monochromatic nature and coherency, were thoroughly investigated, with specific attention given to the Gaussian laser beam function. The study also delved into the fundamental phenomena of laser light interaction with metals, encompassing absorption, conduction, melting, vaporization, and plasma formation, all analyzed through the lens of local thermodynamic equilibrium. The investigation extended to laser welding fundamentals, equipment costs, safety considerations, and advantages of keyhole laser welding, as well as conduction-limited laser welding. Furthermore, the study explored potential process parameters for keyhole laser welding, divided into laser source/ focused beam, workpiece, and filler material aspects. While this research encompassed the laser weldability of titanium alloys, touching on topics like embrittlement, cracking, hydrogen porosity, and processing porosity, with a focus on prevention methods, it is essential to note that the study did not include characteristic modeling of laser beam welding processing. Such modeling would have covered mechanical, metallurgical, and geometrical aspects, representing a crucial area that warrants further exploration in future research.

The prospects of laser beam welding technology in the automotive industry for the use of the lightweight materials was reviewed based on materials consideration such as aluminum alloys, magnesium alloys, and titanium alloys by Hong and Shin [4]. In this comprehensive study, a comparative analysis between laser welding and resistance spot welding of galvanized steel was conducted [4]. The comparison involved modifying the weld configuration, adjusting the element composition, employing a pulse laser, and eliminating the zinc coating. Furthermore, the practicality of implementing of these innovative techniques in an industrial setting was thoroughly explored. Extending this investigation beyond galvanized steel, the application of laser welding in magnesium alloys, aluminum alloys, titanium alloys, and even dissimilar materials was examined. In addition to discussing the feasibility of these techniques, the microstructural changes and defects that arise during the laser welding process for these various materials were discussed. Although the mechanical characteristics of the welds, such as hardness, shear strength, and tensile strength were considered in this study, but laser beam modelling in mechanical characteristics and other characteristic modeling such as geometrical and metallurgical were not considered.

Subashini et al. [5] provided the investigation on the role of filler addition in the laser-MIG hybrid welding (LMHW) process compared to autogenous laser welding (ALW) for 10-mm-thick maraging steel plates. In this study, the welding setup, in comparison with ALW, the effect of microstructure, mechanical characteristics, fracture toughness, and advantages of LHW were considered and discussed [5]. In other words, this study emphasized the benefits of

using filler wire in the laser-MIG hybrid welding process for 10-mm-thick maraging steel plates and the characteristic modeling of LBW, which is one of the critical aspects in terms of controlling the process was not considered in the presented study. Thus, a comprehensive study, which provides valuable insights for metallurgical, mechanical, and geometrical characteristic modeling of laser beam welding process, is needed.

The status of laser beam welding/brazing of aluminum alloy to steel were investigated by [6]. This study covers an analysis of the three main aspects including the (1) process of laser beam welding/brazing, (2) microstructure of intermetallic reaction layer, and (3) mechanical characteristics [6]. In the first part of study, the different aspects of the laser welding/brazing process when joining aluminum alloy to steel, including details about the selection of the laser source, temperature control during the process, and the choice of filler metal for effective bonding between the dissimilar metals (Fe/Al), were presented. In the second section of study, the microstructure of the intermetallic reaction layer formed during the laser welding/brazing process between aluminum alloy and steel was investigated, and the microstructure for optimizing the welding/brazing parameters was examined. Although, this study analyzed the mechanical characteristics of the Fe/Al joint after laser welding/brazing. This includes factors such as joint strength, toughness, and resistance to different types of loads or stresses, but the mechanical characteristics, metallurgical characteristics, and geometrical characteristics models of LBW process were not considered and discussed. Thus, a valuable contribution on review of characteristics models of LBW process including mechanical, metallurgical, and geometrical models is required.

Sadeghian and Iqbal [7] presented an insightful review of challenges and recent advancements in dissimilar laser beam welding of steel-cooper, steel-aluminum, aluminum-copper, and steel-nickel for electric vehicle battery (EV) systems. The focus of study is on the joining process of battery cells considering interconnect joints, which are critical for functionality and efficiency of the battery system including (1) importance of joints in EV battery systems, (2) advantages of LBW in EV battery manufacturing, (3) challenges with dissimilar materials, (4) undesirable weld microstructures, (5) various material combinations, (6) analysis of joint characteristics, and (7) influence of process parameters and interlayers/coating [7]. Thus, it can be concluded that mechanical, metallurgical, and geometrical characteristic modeling of LBW, which is the focus of the current study, was not considered in the study of Sadeghian and Iqbal [7].

The LBW process is mainly influenced by several factors, including welding processing parameters, laser beam quality, interactions between the irradiation and the material, and environmental fluctuations. The results are distributed over

a wide area, and thus, it is still difficult to comprehensively explored and predict the characteristics of the LBW process and their impact on the performances of joint characteristics. Under extreme LBW thermal cycle, the metallurgical characteristics of the weld joint and surrounding internal stress have significantly changed, which is different from the base metal and investigated by another study [8]. The noticeable challenges with the LBW process are controlling characteristics of welded parts, including geometrical, metallurgical, and mechanical characteristics, as well as weld defects.

The geometry of the weld or fusion zone is considered as the weld geometrical characteristics. It is reported that weld geometrical characteristics affect other characteristics of weld. For instance, it is proven that increasing the geometrical characteristics such as the radius of weld toes and decreasing the values of flank angle led to the improvement of the butt welded's fatigue life and fatigue strength [9]. The fracture peak load of the weld is increased by the increase in fusion zone dimensions [10]. Another study shows that notch weld geometry significantly influences the fatigue failure of weld [11]. Other geometrical characteristics of weld, e.g., width, affect directly on the fracture behavior of weld [12]. Thus, since weld performance and other characteristics are influenced by geometrical weld characteristics, this characteristic is considered in masses of previous studies in the LBW modeling area.

Weld metal characteristics are mainly controlled by metallurgical characteristics. These characteristics of the weld are considerably changed depending on its chemical composition. Metallurgical weld characteristics refer to characteristics including grain size, alloying elements, and microstructures resulting from the welding process in the weld joints. It is a fact that grain size has a considerable impact on mechanical characteristics [13]. Small grain size and the existence of martensite in the weld fusion zone resulted in higher hardness in the weld fusion zone. Formation of martensite, which has poor corrosion resistance, leads to weak corrosion resistance in the weld metal. In contrast, the increase of austenite microstructure with good resistance provides strong corrosion resistance in the weld fusion zone [14]. Studies revealed that the toughness of weld metals is improved by increasing the acicular ferrite [15]. The existence of grain boundary ferrite lowers the toughness of weld metal [16]. Therefore, the effect of alloying elements, microstructure, and grain size on weld performance is discussed, which reveals the significant impact of metallurgical characteristics of weld metal on its performance. Thus, a demand for a comprehensive study on presented metallurgical characteristics models is required to detect its behavior during welding and performance of weld.

Weld characteristics, which define the mechanical behavior of welds, are considered as weld mechanical characteristics, which affect weld performance directly. It is reported that the joint performance strength decreases moderately when a lower and smaller region of residual stress is induced [17]. The residual stress (as a weld mechanical characteristic), which is produced by rapid temperature variation during the welding process, is often crucial for the life cycle behavior of structures, especially for key connection regions in offshore and marine applications [18]. Studies revealed that an increase in weld hardness led to a decrease in yield strength, impact toughness, and tensile strength [19]. Thus, it is shown that mechanical characteristics play prominent role in laser beam–welded part's performance in different ways dramatically.

The appropriate modeling of the LBW process is a critical factor in accomplishing desired characteristics of the weld joints. The comprehension model for the LBW process is obligatory for proper employment and optimization of these welding techniques. The modeling of the LBW process is intrinsically problematic, as it must comprise the rapid cooling rates and high-temperature gradient because of the high energy density of laser beams. Furthermore, such a process involves various physical mechanisms that are strongly coupled, for instance, mechanisms of phase transition, laser-material interaction and absorption, and energy transfer in all four phases, including solid, liquid, gas, and plasma phases [20]. Thus, proper and applicable models have an impact on the investigation of the LBW process and are required for understanding the process better.

Although demands for high-performance welds have been increasing in various application areas, and masses of studies have been focused on LBW process modeling (LBWPM), currently, limited literature have focused on detailing based on geometrical, metallurgical, and mechanical characteristics. Moreover, while a few attempts reviewing of the LBW process can be found in the literature [21–25], a comprehensive study of the whole presented different types of modeling of the LBW process is not yet reported. One interesting feature worth mentioning is that, in almost all relevant cases reported in the literature, there has been a review of dissimilar joining of aluminum alloys to steels [21], laser welding of NiTi [23], laser welding process and strength enhancement of carbon fiber–reinforced thermoplastic composites and dissimilar metal joint [24], as well as the suppression of the solidification cracks in the laser welding process by controlling the grain structure and chemical compositions [25]. At the same time, none of them focused on LBWPM types or laser beam–welded characteristics as the aim of the study. It can be concluded that previous research dealt with general features of weld, not modeling or specific characteristics of laser beam–welded parts.

In summary, the perception of LBWPM leads to an increase in the performance of laser beam–welded joints. There needed to be more research on the review of LBWPM. In the current study, a comprehensive review of types of

LBWPM, including characteristics of weld, including geometrical, metallurgical, and mechanical, will be presented in Section 2. It will be discussed that LBWPM can be classified on preprocess, in-process, and post-process based on the monitoring. Different methods of LBWPM based on governing equations and physical material properties modeling will be presented. Geometrical characteristic modeling, including weld width, penetration, and deformation, is studied in Section 3 by comparing different case studies. Section 4 represents metallurgical characteristic modeling of the LBW process, for instance, solidification mode, phase transformations, and morphology. Mechanical characteristic modeling includes strength, hardness, and residual stress modeling in Section 5. Finally, the gap of studies and future trends of LBWPM and conclusions are presented in the last section.

2 Types of LBW process modeling

Since laser beam welding or LBW process is one the sensitive processes and various factors in it will lead to the creation of various joint characteristics, the modeling of this process can be categorized in different aspects, including types of characteristics, monitoring, length scale, and methods. In this section, each of these classifications will be introduced and discussed in detail.

2.1 Characteristics of weld joint approach

Since laser beam welding is thermal-based welding, different characteristics, including geometrical, metallurgical, and mechanical weld, can be considered in the process modeling. This characteristic-based classification of LBWPM is introduced in Fig. 1. The geometry of weld, including weld width [26], weld depth [27], and distortion [28, 29], are considered as a geometrical characteristic of weld in LBW process modeling. Laser beam–welded parts can have different

metallurgical characteristics, such as morphology [30] or microstructure [31], which can be considered as an output of the model. Mechanical characteristics of weld, including residual stress [32], strength [33], and hardness [34], are some of the output of modeling, which determines the performance of welded parts. All the abovementioned types of modeling will be present in the following subsections.

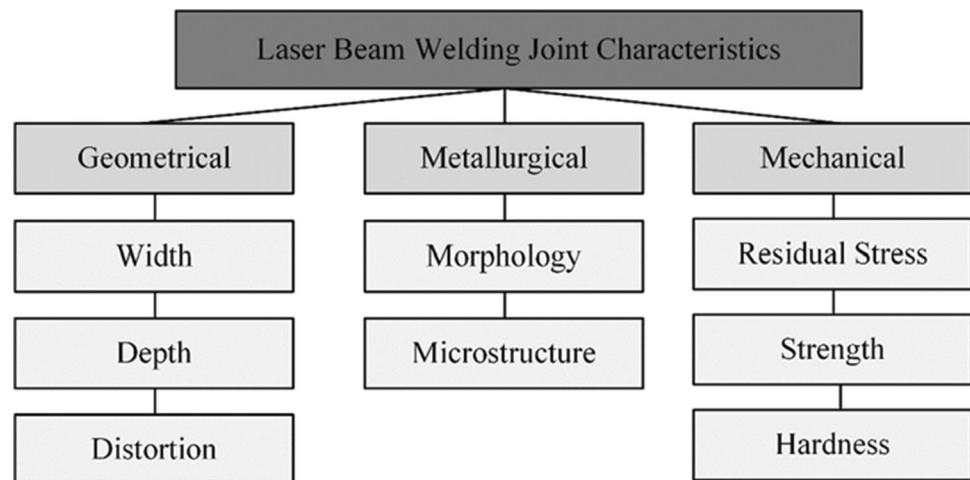#### 2.1.1 Geometrical characteristics

Geometrical characteristics of the weld are one of the most intuitive reflections of the welding process, and most of fundamental LEWPM research usually refers to this topic inevitably. For instance, the welding production efficiency is usually optimized if full penetration and desirable weld width can be achieved in a single pass [35]. Thus, it is enormously essential to achieve specific geometrical features in a welding process.

Weld geometry varies throughout the whole thickness, and relying solely on representations of penetration and surface width to assess the modeling seems oversimplified. Different geometrical features of a weld bead can be investigated. However, the three most noticeable features are the weld width (*W*), weld penetration (*P*), and distortion (*D*), which are shown schematically in parts A and B of Fig. 2, respectively.

Considering the fusion (FZ) and heat-affected zones (HAZ), the weld width is defined as the width of the fusion zone, whereas the weld penetration is the height of the fusion zone. As an example, the measured weld width and penetration for specimens are shown in part A of Fig. 2 [36]. Some recent studies which modeled the width and penetration of laser beam–welded joints will be presented and discussed with split details in Section 3.1.

Distortion is defined as the permanent deformation of the weld joint after the welding process. In the LBW process, distortion is one of the most critical geometrical

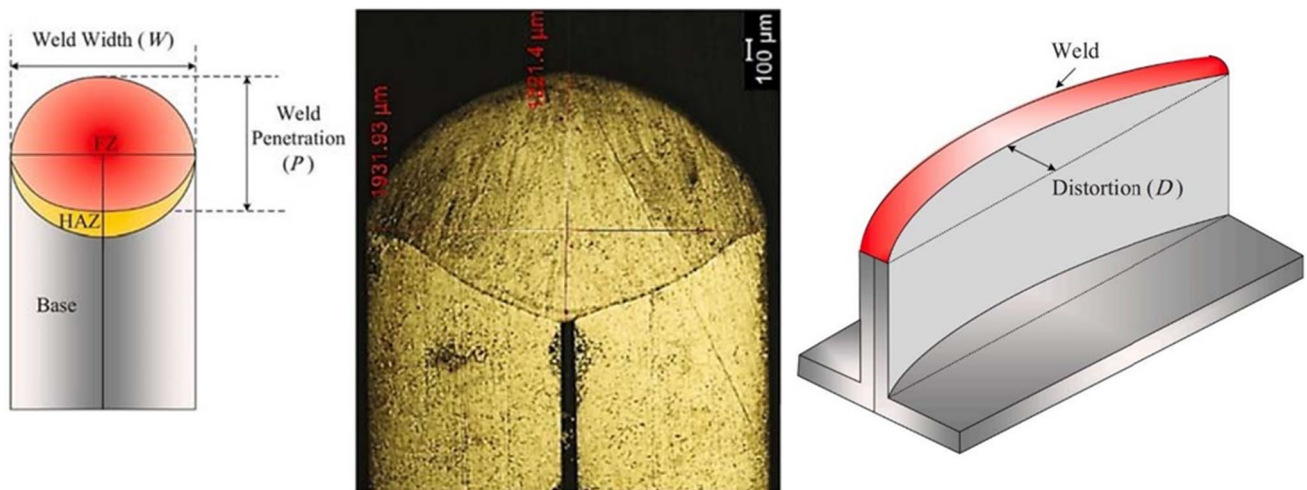**Fig. 1** Types of LBWPM based on weld joint characteristics

Fig. 2 Laser beam welding (LBW) geometrical characteristics. **A** The schematic and the microscopic view of weld width (*W*) and weld penetration or penetration (*P*). **B** Schematic of weld distortion (*D*) [36]

characteristics that is considered in different manufacturing applications. For instance, in plate heat exchangers, assembly problems arise if distortion occurs in the welded plates. In addition, the presence of distortion affects the fluid flow pattern in the exchanger and can even lead to the reduction of thermal efficiency. Therefore, as much as possible, the conditions should be such that the distortion created in the welded plates is minimized. Studies classified distortion of weld joints into two general categories: (1) in-plane (transverse contraction, longitudinal contraction, and rotational distortion) and (2) out-of-plane (angular distortion, longitudinal bending, buckling distortion), which are shown schematically in Fig. 3 [37]. In Section 3.2 some noticeable studies which modeled the deformation of the LBW process are considered and compared with each other's in different terms.

2.1.2 Metallurgical characteristics

Weld metallurgical characteristics, on which the operating performances of welding joints stand, have always been the fundamental evaluation criteria of joint characteristics. The metallurgical characteristic of the fusion zone (FZ) affects

other characteristics of laser beam–welded objects, such as mechanical characteristics. A coarse columnar structure of FZ is harmful to the mechanical characteristics of weld [38]. On the other hand, the formation of fine equiaxed grains in FZ has two significant advantages: (1) Fine equiaxed grains in the FZ reduce the susceptibility to solidification cracking during the LBW process, and (2) fine equiaxed grains improve the mechanical characteristics [39]. In addition, it was found that the microstructure, related to the mechanical performance of the welds, is mainly influenced by the metal compositions, cooling rate, and temperature gradient [40].

Metallurgical characteristics of the laser beam welding (LBW) process can be classified into two categories, including (1) weld metal solidification or WMS (microstructure within grains (MWG) or solidification mode (SM) and grain structure size (GSS) or morphology) and (2) post-solidification or PS (considering phase transformations (PT)), which will be defined in the following subsections.

Solidification mode and phase transformations During the solidification of materials, four types of morphology are observed, such as (1) planar, (2) cellular, (3) columnar dendritic, and (4) equiaxed dendritic as shown in parts A, B,
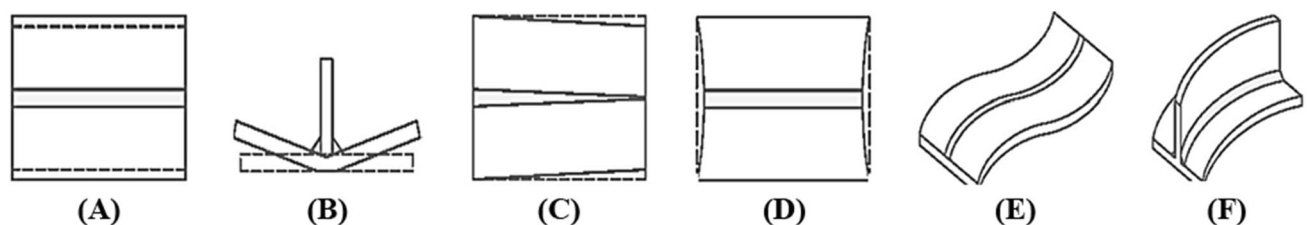

Fig. 3 Types of distortions. **A** Transverse shrinkage. **B** Angular distortion. **C** Rotational distortion. **D** Longitudinal shrinkage. **E** Buckling distortion. **F** Longitudinal bending distortion [37]

C, and D of Fig. 4. According to a study [39], in order to provide a stable solidification mode in stable conditions, the following relationship must be approved:

$$\frac{G}{R} \geq \frac{\Delta T}{D_\mathrm{L}} \tag{1}$$

where ΔT is the temperature difference along the boundary layer and is equal to $\Delta T = T_\mathrm{L} - T_\mathrm{S}$ Also, D_L is the liquid diffusivity coefficient. The speed of movement of the middle layer solid liquid layer is called the "solidification growth rate" or R. "Temperature gradient" or G in liquid metal is the difference in the temperature profile. With the increase of the solidification growth rate and temperature gradient, the solidification modes will be transferred from planar to cellular, cellular to columnar, and finally from columnar to equiaxed dendrite, as shown in part E of Fig. 4.

In the laser beam welding process, which is a laser material processing, both the cooling rate and the growth rate are very high and temperature gradient is very small. Therefore, columnar or equiaxed dendritic modes are created in the solidification process of LBW [43]. For stainless steel, one the most famous metals in the LBW process, solidification modes, and microstructure is based on Cr_{eq}/Ni_{eq} in Table 1,
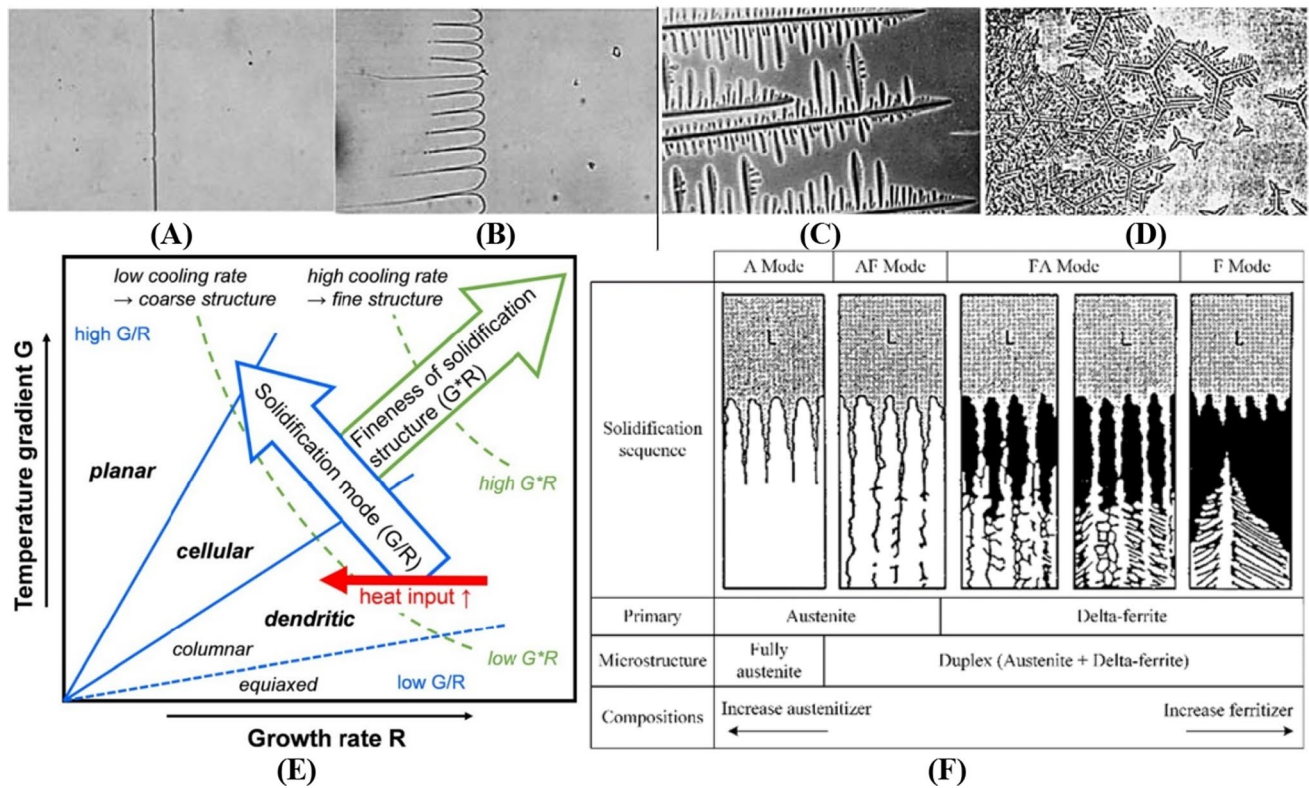

Fig. 4 Basic solidification modes; **A** Planar of carbon tetrabromide. **B** Cellular of carbon tetrabromide. **C** Columnar dendritic of carbon tetrabromide. **D** Equiaxed dendritic of cyclohexanol [41]. **E** The effect of solidification growth rate or R and temperature gradient or G on solidification modes [39]. **F** Solidification modes of austenitic stainless steel weld joints [42]

Table 1 Solidification modes based on equivalent Cr_{eq}/Ni_{eq} and related microstructures [44]

Solidification mode	Equivalent ratio	Reaction	Microstructure
A, fully austenite	$Cr_{eq}/Ni_{eq} < 1.25$	$L \rightarrow L+A \rightarrow A$	Fully austenitic
AF, austenite ferritic	$1.25 < Cr_{eq}/Ni_{eq} < 1.48$	$L \rightarrow L+A \rightarrow L+A+(A+F)_{Eut} \rightarrow A+F_{Eut}$	Ferrite at cell and dendrite boundaries
FA, ferritic austenite	$1.48 < Cr_{eq}/Ni_{eq} < 1.95$	$L \rightarrow L+F \rightarrow L+F+(F+A)_{Per/Eut} \rightarrow F+A$	Skeletal and/or lathy ferrite resulting from ferrite to austenite transformation
F, ferritic	$1.95 < Cr_{eq}/Ni_{eq}$	$L \rightarrow L+F \rightarrow F \rightarrow F+A$	Acicular ferrite or ferrite matrix with grain boundary austenite and Widmanstatten side plates

Table 2 Constitution elements, partition coefficients, and low melting phases of 304L-316L welded [44]

S. No	Constituent	Temperature (°C)	Partition coefficient		Low melting phases	
			δ	γ	Structure	Melting point (°C)
1	Sulphur	1365	0.091	0.035	Eutectic Fe-FeS	988
					Eutectic Ni-NiS	630
2	Phosphorous	1250	0.23	0.125	Eutectic Fe-Fe3P	1048
					Eutectic Ni-Ni3P	875
3	Silicon	1300	0.77	0.52	Eutectic Fe-Fe2Si	1212
					Eutectic NiSi-Ni3Si2	964
					NiSiγ	996

Table 3 The relationship of Cr_{eq}/Ni_{eq}

Row	Formula	Ref
1	(Cr + 1.37Mo + 1.5Si + 2Nb + 3Ti)/(Ni + 0.31Mn + 22C + 14.2N + Cu)	[45]
2	(Cr + Mo + 1.5Si + 0.5Nb)/(Ni + 0.5Mn + 30(C + N))	[46]
3	(Cr + Mo + 0.7Nb)/(Ni + 35C + 20N + 0.25Cu)	[47]

Table 2, and part F of Fig. 4. The Cr_{eq}/Ni_{eq} is also defined based on different studies in Table 3.

Morphology Grain size or morphology is another metallurgical characteristic of the fusion zone in the laser beam welding process. It is reported that by increasing $G \times R$ (which is defined as "cooling rate or CR"), the grain size decreased. Studies indicated that a higher cooling rate provides finer cellular or dendritic structure [39]. The eutectic spacing or λ_E, primary dendritic arm spacing (PDAS) or λ_1, and secondary dendritic arm spacing (SDAS) or λ_2 are three main parameters, which are considered in morphology or grain size in LBW process modeling as shown in parts A, B, C, and D of Fig. 5 [48].

2.1.3 Mechanical characteristics

An effective weld is as strong as that of the weakest of the two different metals being connected, that is, it has enough strength to prevent the junction from failing during the weld [49]. Hence, the exploration of the mechanical characteristics of welded joints is one of the most essential and valuable aims that allow to determine their performance and functional properties. For technical reasons, welded joints
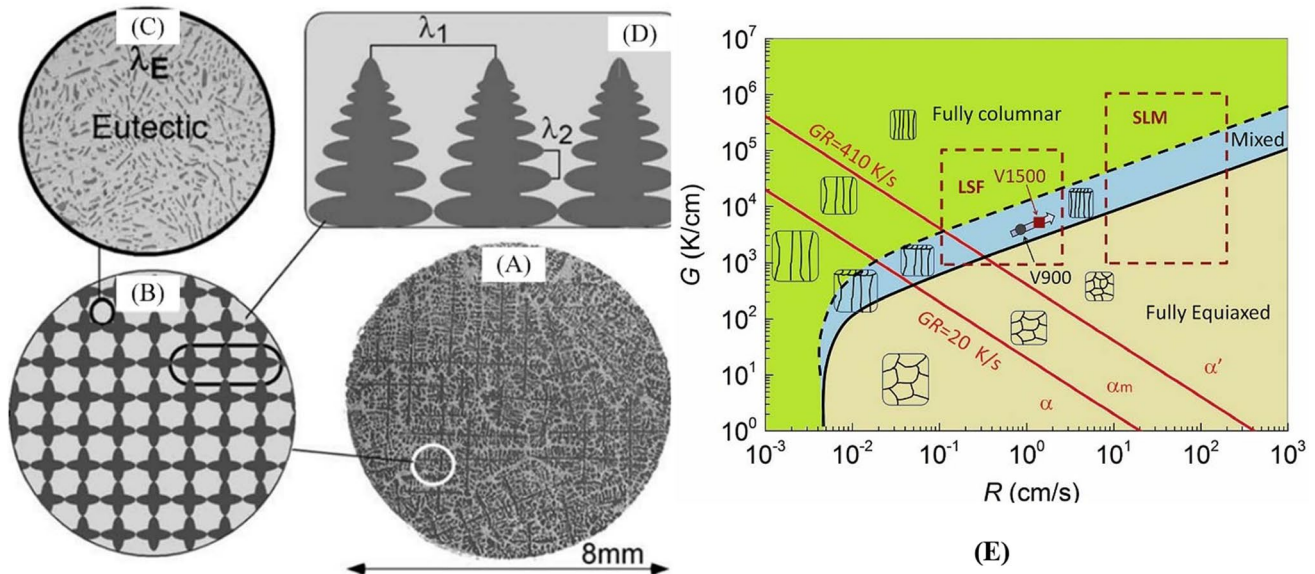

Fig. 5 Microstructure; (A) Cross-section of eutectic structure. (B) Schematic of grain structure. (C) Eutectic spacing or λ_E. (D) Primary dendritic arm spacing (PDAS) or λ_1 and secondary dendritic arm spacing (SDAS) or λ_2. (E) The CET based on growth rate (R) and gradient temperatures (G) [48]

require proper mechanical characteristics, including tensile strength, hardness, and residual stress. Such weld joints are applied in the construction of sensitive and expensive applications, for instance, power steam stations, chemical tankers, apparatus, and chemical plants [50].

The tensile strength is employed to estimate the tensile characteristics of the weldments [51]. The tensile strength is lower when the weld metal joint has poor loading capacity and weld quality. If the weld metal is high, toughness can possess better tensile strength [52]. Regarding importance of this area, some studies have been focused on the modeling weld joint strength, including the ultimate tensile strength (UTS), yield stress, and the strain corresponding to the UTS, which will be presented in Section 5.1.

Unfavorable weld joint hardness is an undesirable quality [53]. Several investigations demonstrated the changes weld joint hardness in the weld metal resulted in laser beam welding process. The LBW process caused a drastic increase in the weld metal hardness (388 HV) and coarse prior austenite grain bainite region (390 HV) compared to the hardness of base metal (BM) (below 200 HV). Both of the applied PWHT variants reduced the hardness of these areas of welded joints to the BM level [51]. It is reported that hardness is around 60% higher at FZ than at BM, being maximum at supercritical HAZ due to its highly refined microstructure, and HAZ softening was not observed (Mansur, de Figueiredo [54]. The presented models of hardness profile in LBWPM are provided in Section 5.2.

Residual stress that results from welded joints is another noticeable factor that needs to be considered in the mechanical characteristics of laser beam–welded structures. It is well known that tensile residual stresses in welded structures can be as high as the yield strength of the material, and they have a detrimental effect on the weld performance. The combination of tensile welding residual stresses and operating stresses to which engineering structures and components are subjected can promote failure by fatigue. Conversely, compressive residual stresses could have a favorable effect on fatigue life. However, spectrum loading may relax part of the residual stress field, which will affect the final fatigue life [55]. Regarding the importance of this area, some scholars have conducted in-depth research on the modeling of residual stress resulting from the LBW process, which will be discussed in Section 5.3.

2.2 Monitoring approach

Monitoring plays a critical role in LBW process modeling, and its impact is multifaceted, significantly influencing the modeling process. The monitoring contributes and impacts LBW process modeling with different ways including (1) model validation, (2) parameter calibration, and (3) model development and improvement. Monitoring the laser beam

welding (LBW) process plays a critical role in providing real-time insights into crucial welding parameters, including power, speed, temperature, and material characteristics. These real-time results serve as invaluable tools for validating and enhancing the precision of LBW process models. By comparing the predictions of these models with the actual monitoring results, researchers can make refinements to improve the model's accuracy.

Part A of Fig. 6 showcases how the monitoring process, in combination with metallographic testing, can be employed to validate the numerical model's accuracy in predicting the weld depth in the laser beam welding process [56]. In addition to this, a multifaceted approach is utilized, incorporating both unisensor and multisensor monitoring, as well as convolutional neural network (CNN) models for predicting weld depth. Optical coherence tomography sensors, such as photodiode signals, are considered for validation, as illustrated in part B of Fig. 6 [26]. During the monitoring phase, high-speed cameras (Mini UX30, FASTCAM, Japan) and photodiodes are employed as input sensors in study [26]. The high-speed camera operates at an impressive frame rate of 10,000 frames per second. To mitigate the interference caused by laser-induced plasma and plumes during image acquisition, a diode laser beam is directed onto the specimen surface. In front of the camera lens, a band-pass filter and a neutral density filter are installed. A comprehensive view of the monitoring and experimental setup for this study is presented in part C of Fig. 6, outlining the intricate details of the equipment and processes involved.

Monitoring plays a pivotal role in fine-tuning or parameter calibration process models for laser beam welding (LBW). Through the careful analysis of monitored data in conjunction with the model's input parameters, researchers gain the ability to make precise adjustments to model coefficients or constants, ensuring that the model accurately reflects the specific conditions of the LBW process under investigation. In a previous study conducted by Stache et al. [57], laser beam position calibration within the LBW process was addressed. This calibration process was designed to alleviate the shortcomings associated with traditional methods and was accomplished through the utilization of a system-incorporated camera. Two distinct techniques were introduced for automatic calibration, both of which overcame previous limitations. The first technique involved calibration at the laser wavelength, wherein the system autonomously generated laser spots, assessed their positions and potential offsets, and ultimately employed an affine model for compensation. The second technique revolved around a specifically coded test pattern designed for camera wavelength calibration. This approach enhanced accuracy. For a comprehensive view of the scanner system with the integrated camera used for position estimation and the experimental results showcasing the precision achieved through
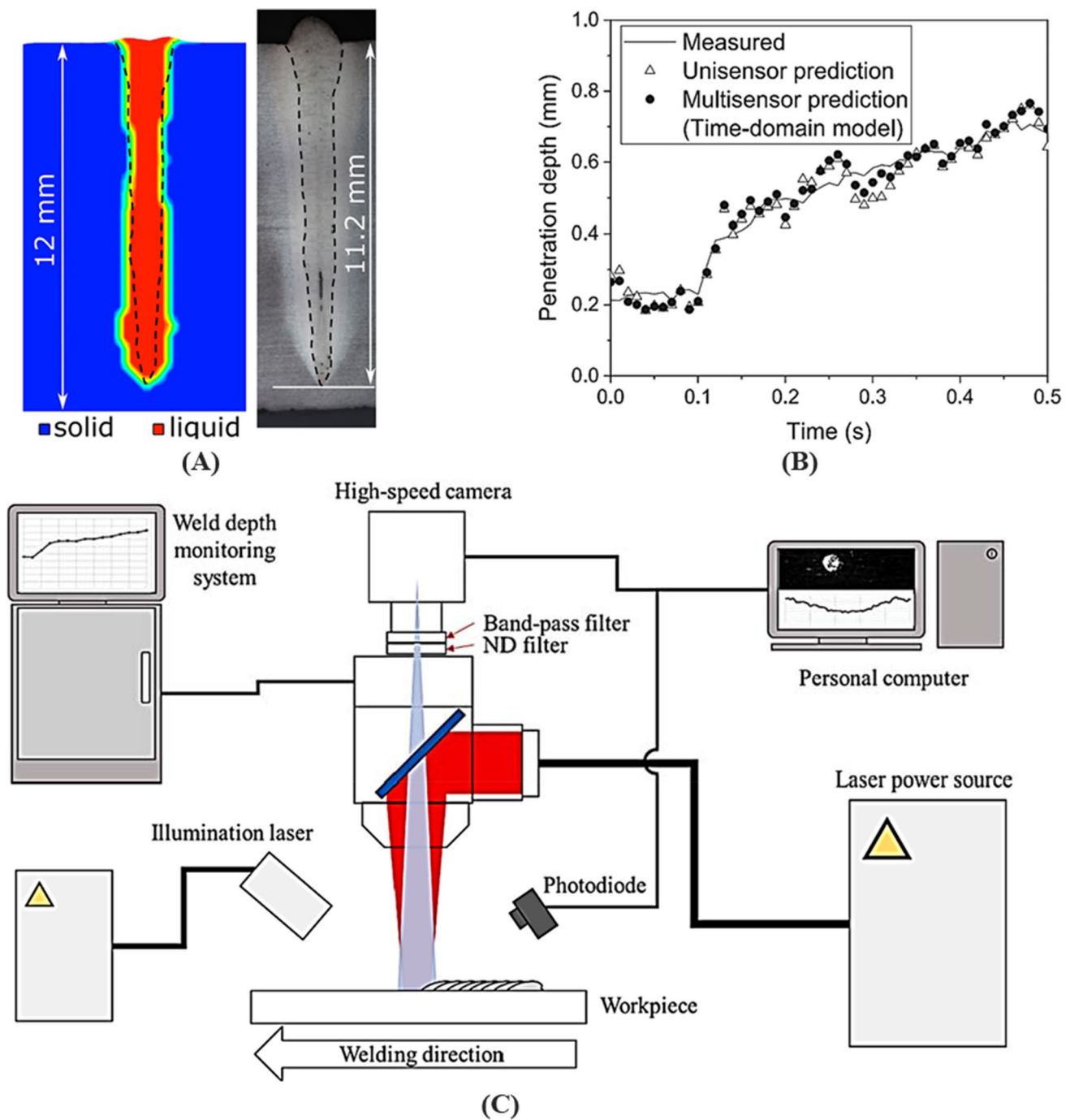
Fig. 6 The model validation with monitoring method for laser beam welding method. **A** Numerical model for weld depth [56]. **B** Machine learning model for weld depth. **C** Schematic diagram of the monitoring experimental setup [26]

calibration, please refer to parts A and B of Fig. 7, which provide a visual representation of the system's schematic and the associated results.

The results derived from the monitoring stage play a crucial role not only in the development of initial models but also in enhancing existing ones. This approach is invaluable in unraveling the intricate interactions within the welding process, ultimately contributing to the creation of more precise and anticipatory models. An illustrative study introduced an innovative weld pool edge detection technique that relies on off-axial green illumination lasers in combination with a coaxial image capture system comprising a CMOS camera and optical filters. To maximize the effectiveness of this approach, a comprehensive edge detection algorithm
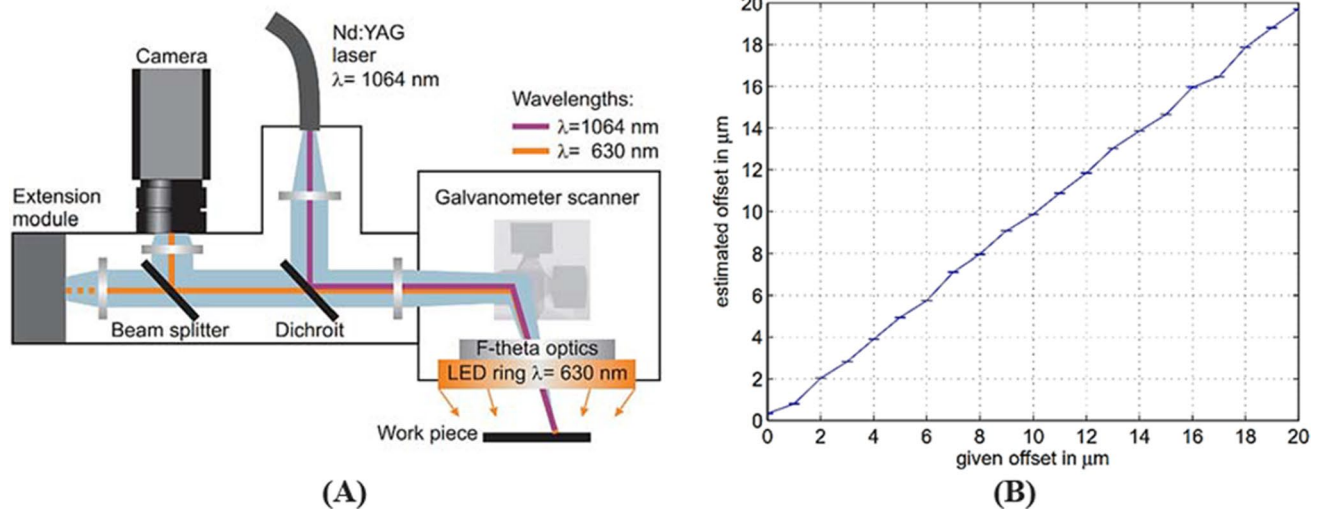
Fig. 7 Parameter calibration with monitoring. **A** The schematic of monitoring system. **B** The experimental results showcasing the precision achieved through calibration [57]

was developed, based on a localized maximum gradient of greyness search method and linear interpolation. This algorithm was meticulously designed to enhance the accuracy of the extracted weld pool geometry and width. These measurements were subsequently validated by comparing them with actual welding width measurements and predictions generated by a numerical multiphase model [58]. For a more detailed investigating of the monitoring and experimental setup, as well as the results showcasing the weld width obtained from the model and the online monitoring, please refer to parts A and B of Fig. 8, which provide a visual representation of the setup and the outcomes.

In this section, the classification of LBWPM is considered based on the monitoring approach. The purpose of monitoring the LBW process is to check the presence of defects and ensure the health of the weld joint. Based on the monitoring process, LBWPM can be classified into three stages, including (1) pre-process, (2) in-process, and (3) post-process [59]. These categories are shown in Fig. 6. The summary of LBWPM based on monitoring aims, signals, and technology in different stages is provided in Table 4.

Expanding upon the insights provided by Cai et al. [59], it becomes evident that LBW modeling can be categorized according to the specific monitoring types applied. This
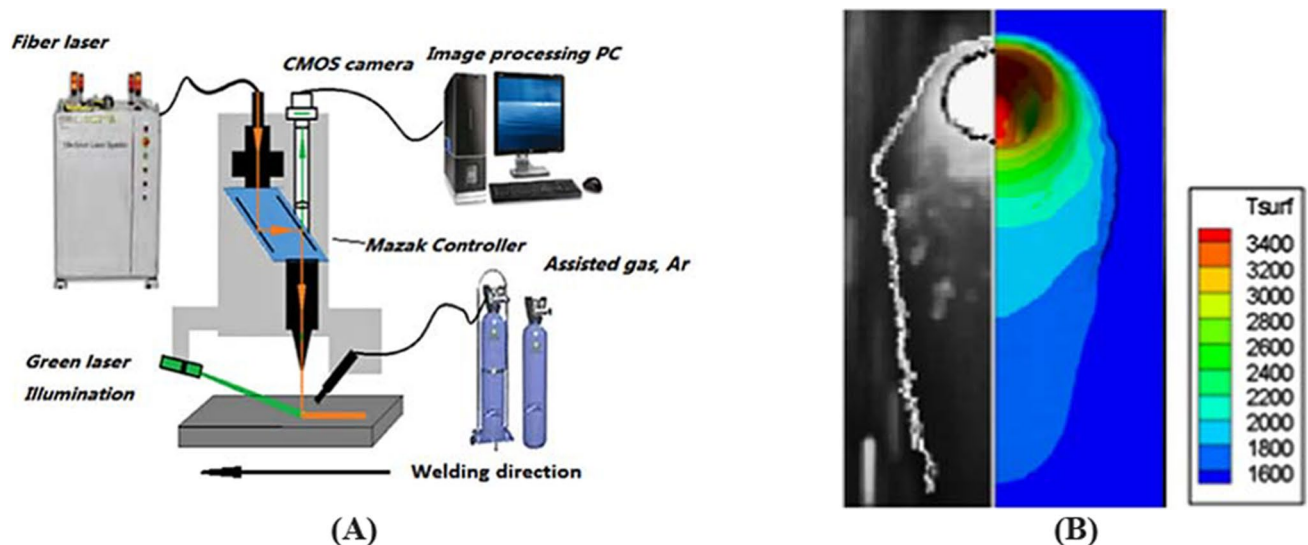

Fig. 8 The laser beam welding model development and improvement with monitoring. **A** The schematic of monitoring and experimental setup. **B** Weld width result of model and on-line monitoring [58]

Table 4 LBWPM based on monitoring aims, signals, and technology in different stages [59]

Monitoring stages	Qualities				
	Measuring weld characteristics	Examples		Signal	Technology
Pre-process	Geometrical	Gap measurement, seam tracking		Optical	Machine vision
					Laser triangular
In-process	Geometrical	Weld pool width, penetration, and keyhole geometry		Acoustical, optical, electrical, thermal	Part B of Fig. 4
	Defects	Surface cracking			
Post-process	Geometrical	Width, penetration, and distortion		Acoustical and optical	Machine vision
	Defects	All types of internal cracking, LOF, porosity			Destructive and nondestructive inspection
	Mechanical	Yield strength, fracture force			Metallurgic tests
	Metallurgical	Microstructure and grain size			Laser triangulation

categorization allows to classify the LBW modeling process into three distinct categories: (1) pre-process, (2) in-process, and (3) post-process models as shown in part A of Fig. 9.

- Pre-process models: These models encompass aspects related to the preparatory stages of LBW process. Notably, they involve gap measurement and seam tracking. Monitoring during these phases primarily falls under the pre-process category. For instance, modeling gap measurement and seam tracking is vital to ensuring precise alignment before initiating the welding process.

- In-process models: In this category, the focus shifts to the dynamic aspects of the LBW process. Elements such as weld pool width, penetration depth, keyhole geometry, and surface cracking are classified as in-process models. Real-time monitoring is essential for these parameters to ensure optimal welding conditions. As an example, weld pool width can be effectively modeled by employing an optical camera monitoring system during the ongoing welding process. Surface cracking can be detected and modeled using techniques like acoustical emission, providing critical feedback to prevent defects.
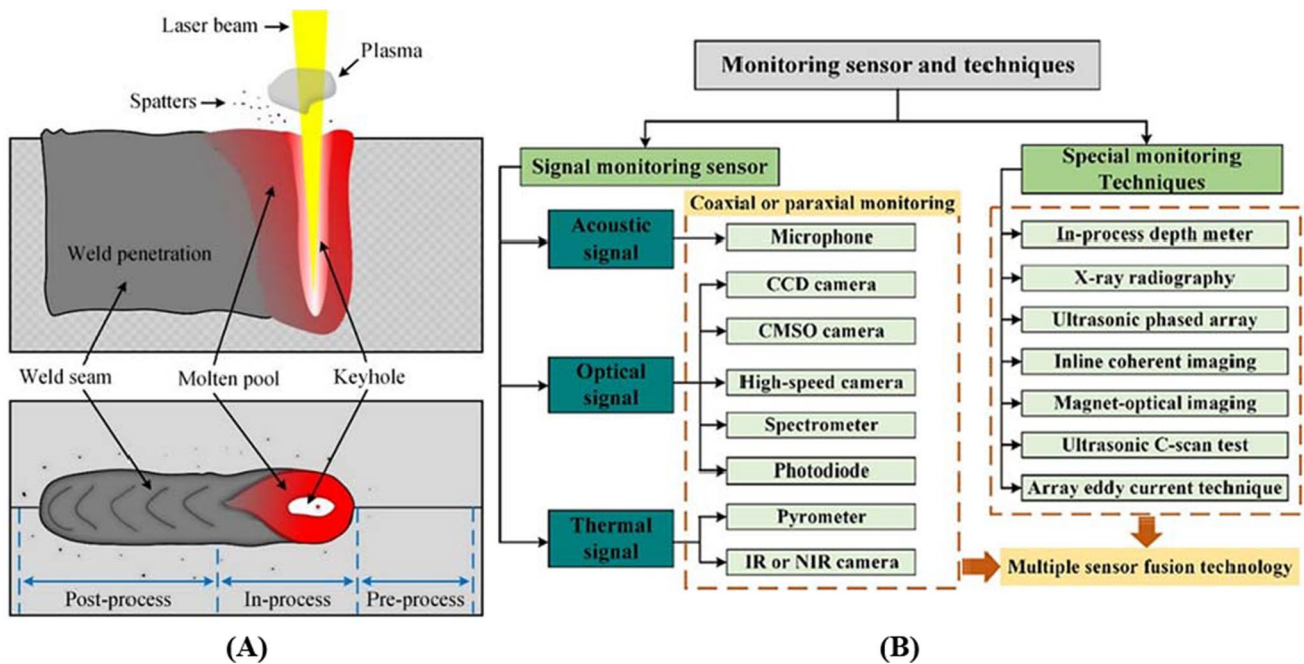

Fig. 9 Monitoring approach. **A** The schematic of the LBW process and types of monitoring. **B** The classification of sensors and techniques [59]

- Post-process models: Post-process models are concerned with characteristics and assessments that occur after the LBW process is completed. Key among these is the evaluation of mechanical characteristics of welds, including yield strength and fracture force. Such attributes are typically determined through destructive tests performed once the welding process has concluded. Similarly, metallurgical characteristics, such as microstructure and grain size, are examined through methods like SEM, EDX, and XRD. Defects, like internal cracking, lack of fusion (LOF), and porosity, are also monitored in the post-process phase. Radiography tests and metallurgic examinations play a significant role in modeling these characteristics.

By considering the monitoring types involved, the LBW process can be effectively classified into three distinct stages: pre-process, in-process, and post-process. Each stage represents a critical facet of the overall welding process, contributing to its successful execution and quality assurance.

The aim of pre-process models is mainly to provide some weld features, which are provided before applying the laser beam to the workpiece. It is reported that weld geometrical characteristics such as the seam tracking problem and scanning the joint gap between workpieces to ensure that the laser beam spot focuses on the gap center to obtain reliable joints can be obtained by pre-process models using optical signals with machine vision and laser triangular technologies as mentioned in Table 4 [60].

The in-process models focused on some characteristics of the weld zone, which were created during the LBW process. Some weld geometrical characteristics (such as weld width, penetration, and keyhole geometry) and defects (including surface cracking) are detected during the LBW process by using various technologies (shown in part B of Fig. 9) with different signals including acoustical, optical, electrical, or thermal. By analyzing these signals and characteristics, the quality of the weld seam can be predicted and adjusted [61].

The post-process models refer to the models, which provide some characteristics after finishing the LBW process,

including geometrical (weld width, penetration, and distortion), metallurgical (microstructure, grain size), mechanical (yield strength, fracture force), and defects (all types of internal cracking, LOF, porosity) [62]. These characteristics are modeled by employing various technologies (such as machine vision, destructive and nondestructive inspection, metallurgic tests, and laser triangulation) with the help of acoustical and optical signals, as shown in Table 4.

It should be noted that to create a model of the LBW process, the data must be monitored and collected by one of the introduced technologies. Next, the data will be analyzed by different methods and models. Thus, LBW process modeling can be classified based on the monitoring methods in three pre-process, in-process, and post-process kinds, as shown in Fig. 7. The presented models can also be analyzed in two categories: (1) static and (2) dynamic (offline or online). The static models are independent of time, while dynamic models depend on time. The characteristics output of static models is not influenced by time.

The dynamic models, which define the weld characteristics based on time, are divided into offline and online kinds. In online models, online signals consider in the model directly from the initial step until the last steps of the LBW process. In other words, all momentary environmental changes affect output characteristics. In offline LBWPM, the signal of the initial step or just one or two specific steps will be detected and considered in the model, and the characteristics will be provided based on selected steps, not all (Fig. 10). Thus, fluctuations or momentary changes are not considered in the models.

2.3 Length scale

Although laser beam welding has been applied in different applications and masses of papers investigated the LBW modeling, the physics of this process is still the subject of many current research projects. This is because of the complexity of the LBW process, which includes a variety of different coupled physical phenomena that appear in a small zone of the melt pools. Process disturbances may even cause variations in the weld zone and non-equilibrium physical

Fig. 10 Classification of laser beam welding modeling studies based on process monitoring stage
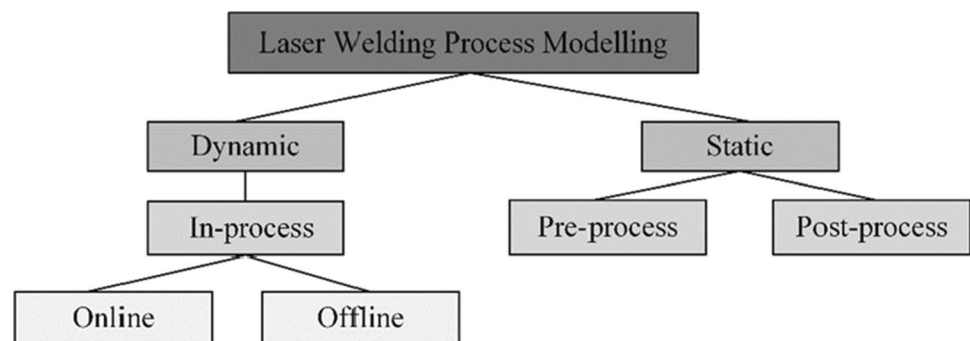
and chemical metallurgical process, which exhibits multiple modes of phenomena making this challenge worse. An investigation categorized LBW physical phenomena into five mechanisms, including (1) absorption, (2) heat conduction, (3) vapor dynamic, (4) melt dynamics, and (5) phase transitions, as shown in Fig. 11 [63].

As shown in Fig. 11, in the absorption mechanism of LBW, Frensel absorption, multiple reflections, vapor and plasma absorption, and temperature-dependent optical properties are involved. The heat conduction mechanism of the LBW process includes convective and conductive heat flux and melting and evaporation enthalpy. Pressure waves and the Bernoulli effect are two phenomena, which can be considered in the vapor dynamic mechanism of the LBW process. Phase transitions, which are one the most complex mechanisms of the LBW process, include melting and solidification, evaporation and condensation, vapor pressure on the interface, and mass flux between phases.

The melt dynamics mechanism of the LBW process includes melt expulsion, spilling formation, Marangoni convection, and temperature-dependent material properties (which will be discussed in Section 2.4.2). The fluid dynamics of the melt pool during the LBW process, including vertical and horizontal views, are shown in parts A and B of Fig. 12 [64]. The velocity field shows waves of liquid melt running down the front of the keyhole. A periodical change in the keyhole diameter will be produced because of these waves, which leads to keyhole oscillations. Around the keyhole, the liquid melt is accelerated, while the melt flow hits the backflow from the back of the melt pool at about two-thirds the length (Turbulences
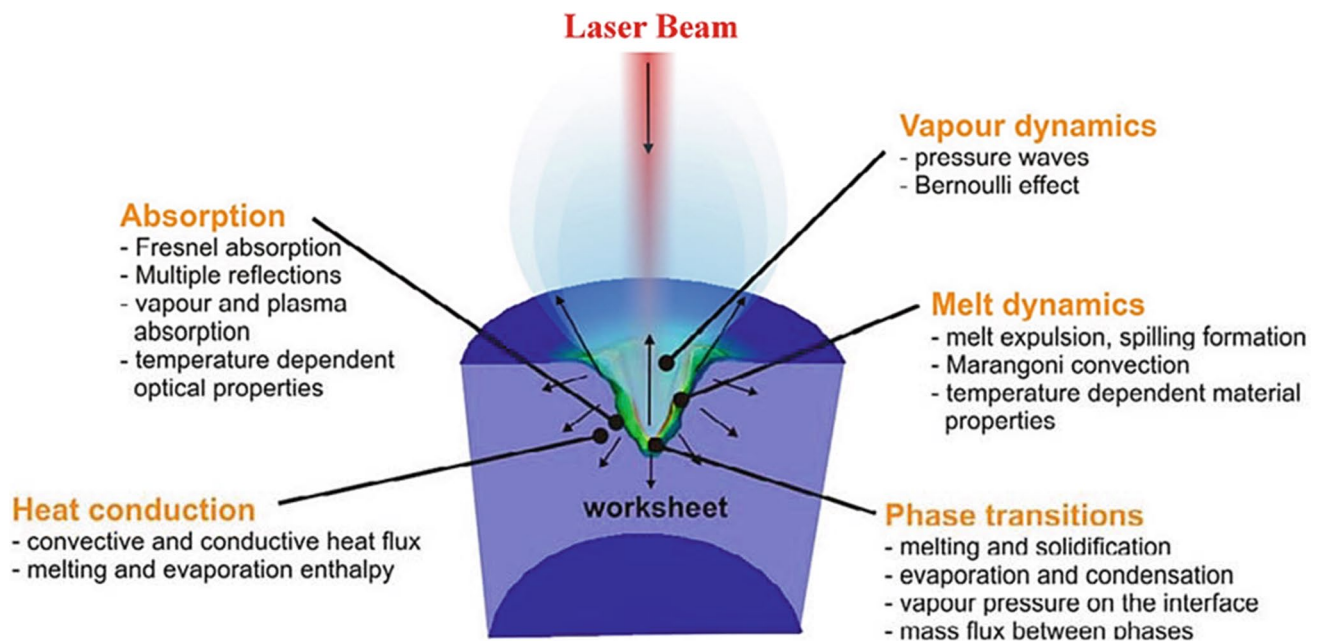

Fig. 11 The five coupled physical phenomena mechanisms in the laser beam welding process [63]
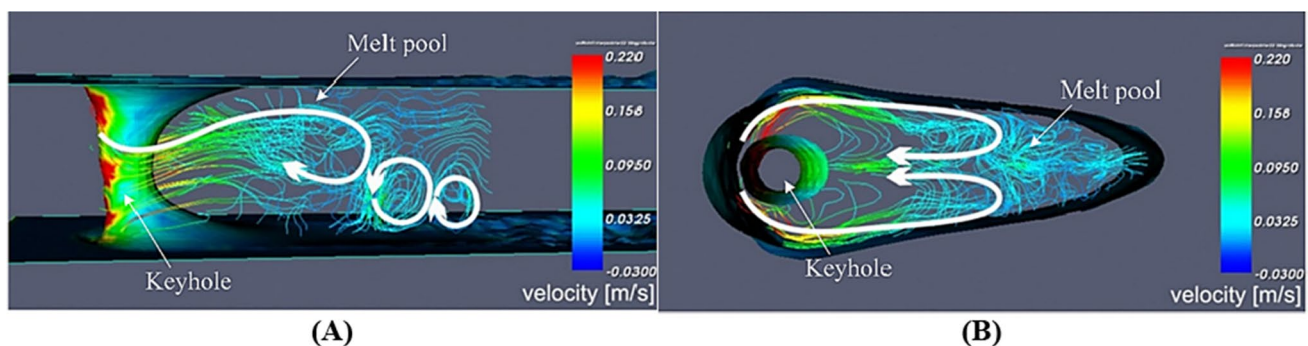

Fig. 12 Fluid dynamics of the melt pool during laser beam welding. **A** Vertical view. **B** Horizontal view [64]

appear in the lower rear part). The flow patten of the melt pool in the upper part is more laminar [63].

To decrease the complexity of the LBW process, some of the phenomena are considered decoupled or neglected in some models [63]. Most of the time, the presented models are only capable of analyzing one of the geometrical, mechanical, and metallurgical characteristics or physical characteristics of the LBW process with one or some mechanisms. The conduction, radiation, and convection mechanisms are considered to model geometrical characteristics (such as weld width and depth) of laser welding of magnesium alloys, as shown in part A of Fig. 13 [65]. Integrated process–structure–property–performance modeling, including metallurgical characteristics of weld with consideration of Marangoni flow, is presented in another study, as shown in part B of Fig. 13.

Comparing parts A and B of Fig. 13, it can be concluded that based on length scale, the LBW process modeling can be categorized in (1) macroscale, (2) mesoscale, and

(3) microscale (as shown in part C of Fig. 13). The macro-thermomechanics, process modeling, and performance modeling with the scale of $\sim 10^{0}$ to $\sim 10^{-2}$ m is considered as macroscale. Mesoscale models include the scale of $\sim 10^{-2}$ to $\sim 10^{-4}$ m and thermo-fluid dynamics and meso-mechanics mechanisms. Microscale is models with the scale of $\sim 10^{-4}$ to $\sim 10^{-6}$ m, such as a microstructure model. Thus, it can be concluded that each mechanism and each characteristic modeling is categorized in different length scale models.

2.4 Method approach

Based on the method of extracting the model and the solution of it or its approach, laser beam welding process modeling is divided into (1) empirical-based (EB) and (2) theoretical-based (TB), as shown in Fig. 14. Theoretical-based LBW models are built based on the theory that governs the laser beam welding process. The studies in this field can be classified into two categories: (1) exact and (2) numerical.
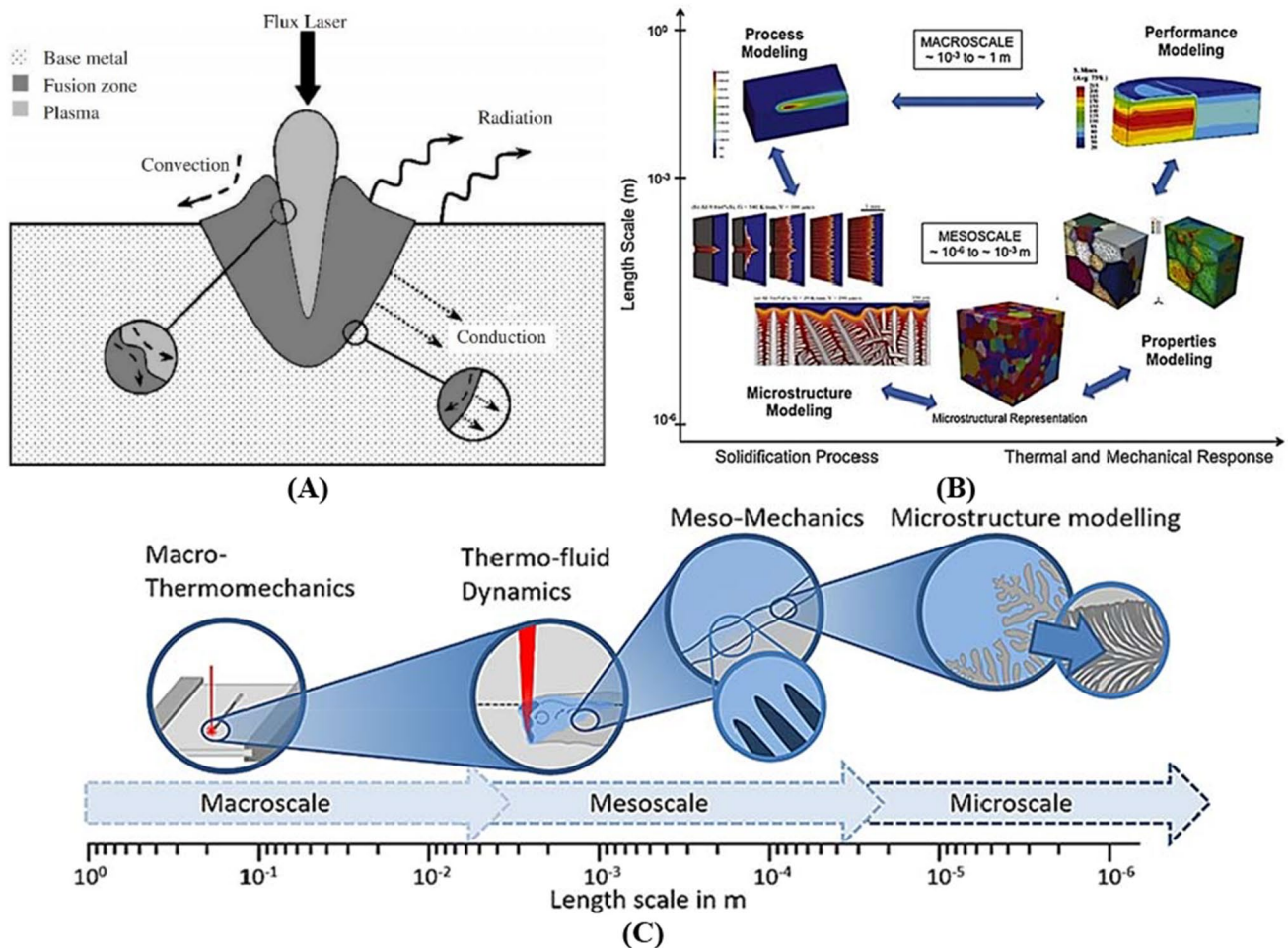

Fig. 13 Laser beam welding models. A The convection, conduction, and radiation mechanism consideration [65]. B Integrated process–structure–property–performance modeling and simulation approach and associated length scales [66]. C LBWPM based on the scales considered [67]
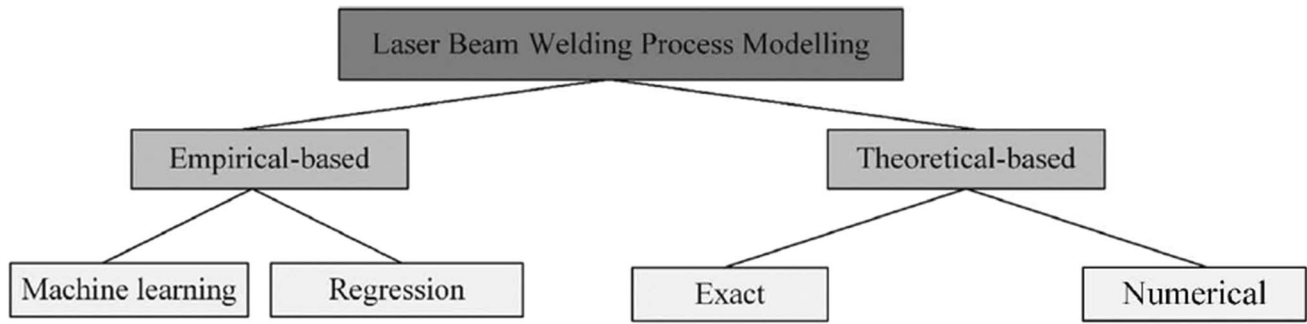
Fig. 14 Classification of LBWPM based on method approach

In exact models, the process outputs are modeled from the existing balance between the input, output, and waste energy of the laser beam welding process and the exact solution of the resulting equation. Numerical models such as finite element methods, some numerical software, and other methods have also been presented in some studies to solve the theoretical equation governing the process. Some governing equations, which can be considered in the LBW theoretical-based models, are presented in Section 2.4.1.

The other category comprises empirical-based laser beam welding process models. These models are divided into two general groups, including (1) machine learning or modern and (2) regression or traditional. If the laser beam welding process is modeled based on machine learning methods such as fuzzy, neural network, and genetic algorithm, the provided model is placed in the machine learning groups. One of the simplest methods for conducting LBW process models is the regression model. In this method, a model called regression model is extracted from fitting the curve between the input and output of the LBW process.

2.4.1 Some of the applicable mathematical equations

To conduct theoretical-based models for the LBW process, some governing equations are presented in this section. The conservation equations of continuity, momentum, energy, and mass fraction are satisfied in the laser beam welding process, as provided in Table 5. Besides these equations, all the mechanisms of heat transfer in fluids, including conduction, convection, and radiation, are evident in the laser beam welding process as discussed in Section 2.3. The forces acting on the workpiece are surface tension, buoyancy force, Marangoni convection, and gravity [68].

The nonlinear heat transfer governing equation, which can be considered in conducting the LBW process modeling, is as follows [70].

$$\rho c \frac{\partial T}{\partial t}(x, y, z, t) = -\nabla . q(x, y, z, t) + Q(x, y, z, t) \tag{6}$$

where ρ is the density of the materials, c is the specific heat capacity (J/(g °C)), T is the current temperature (°C), q is the

Name	Equations	Number
Continuity equation	$\frac{\partial \rho}{\partial t} + \frac{\partial}{\partial x}(\rho v_x) + \frac{\partial}{\partial y}(\rho v_y) + \frac{\partial}{\partial z}(\rho v_z) = 0$	(2)
Momentum equation	$\frac{\partial}{\partial t}(p v_x) + \frac{\partial}{\partial x}(p v_x^2) + \frac{\partial}{\partial y}(p v_x v_y) + \frac{\partial}{\partial z}(p v_x v_z) =$ $= \frac{\partial}{\partial x}\left(\mu \frac{\partial v_x}{\partial x} - p\right) + \frac{\partial}{\partial y}\left(\mu \frac{\partial v_x}{\partial y}\right) + \frac{\partial}{\partial z}\left(\frac{\partial v_x}{\partial z}\right) - M \frac{(1-f_L)^2}{f_L^2 + B} v_x$ $\frac{\partial}{\partial t}(p v_y) + \frac{\partial}{\partial x}(p v_x v_y) + \frac{\partial}{\partial y}(p v_y^2) + \frac{\partial}{\partial z}(p v_x v_y) =$ $= \frac{\partial}{\partial x}\left(\mu \frac{\partial v_y}{\partial x}\right) + \frac{\partial}{\partial y}\left(\mu \frac{\partial v_y}{\partial y} - p\right) + \frac{\partial}{\partial z}\left(\frac{\partial v_y}{\partial z}\right) - M \frac{(1-f_L)^2}{f_L^3 + B} v_y$ $\frac{\partial}{\partial t}(p v_z) + \frac{\partial}{\partial x}(p v_x v_z) + \frac{\partial}{\partial y}(p v_y v_z) + \frac{\partial}{\partial z}(p v_z^2) =$ $= \frac{\partial}{\partial x}\left(\mu \frac{\partial v_z}{\partial x}\right) + \frac{\partial}{\partial y}\left(\mu \frac{\partial v_z}{\partial y}\right) + \frac{\partial}{\partial z}\left(\mu \frac{\partial v_y}{\partial z} - p\right) - M \frac{(1-f_L)^2}{f_L^3 + B} v_y + pg(T - T_0)$	(3)
Energy equation	$\frac{\partial}{\partial t}(pH) + \frac{\partial}{\partial x}(p v_x H) + \frac{\partial}{\partial y}(p v_y H) + \frac{\partial}{\partial z}(p v_z H) =$ $= \frac{\partial}{\partial x}\left(K \frac{\partial T}{\partial x}\right) + \frac{\partial}{\partial y}\left(K \frac{\partial T}{\partial y}\right) + \frac{\partial}{\partial z}\left(\frac{\partial T}{\partial y}\right) + q_{\text{laser}}$	(4)
Mass fraction equation	$\frac{\partial}{\partial t}(pw) + \frac{\partial}{\partial x}(p v_x w) + \frac{\partial}{\partial y}(p v_y w) + \frac{\partial}{\partial z}(p v_z w) =$ $= \frac{\partial}{\partial x}\left(pD \frac{\partial w}{\partial x}\right) + \frac{\partial}{\partial y}\left(pD \frac{\partial w}{\partial y}\right) + \frac{\partial}{\partial z}\left(pD \frac{\partial w}{\partial z}\right)$	(5)

Table 5 Some of the applicable equations for LBW modeling [69]

heat flux vector (W/mm^2), Q is the internal heat generation rate (W/mm^3), x, y, and z are the coordinates in the reference system (mm), t is the time (s), and ∇ is the spatial gradient operator. The nonlinear isotropic Fourier heat flux constitutive equation is employed [70]:

$$q = -k\nabla T \tag{7}$$

where k is the temperature-dependent thermal conductivity (J/(mm s °C)).

2.4.2 Physical material property modeling

Besides mechanisms presented in Section 2.3, the LBW process is a solidification process with a combination of thermodynamic physical phenomena and kinetic reactions, which lead to the creation of different metallurgical, mechanical, and geometrical characteristics in the weld zone [43, 71]. The schematic diagram of this deduction is shown in part A of Fig. 15. Considering this, equilibrium phases, such as ferrite and austenite, of metallurgical characteristics are extracted with thermodynamic process properties, such as the melt pool temperature and phase diagram (part C of Fig. 15). The behavior of changes between phases and morphology (or metallurgical characteristics) in the thermal LBW process is obtained with considering of kinetic reaction parameters, such as cooling rate and heating rate using time–temperature transfer (TTT) diagrams and solidification diagrams as shown in part B of Fig. 15.

Other metallurgical and crystallographic characteristics, such as atomic structure and materials arrangement, will be available by scanning electron microscope test (SEM) [71]. By having crystallographic details or metallurgical characteristics, mechanical characteristics and geometrical characteristics of the weld will be obtained. These characteristics also indicate the performance of the LBW process. Therefore, practically, by having the temperature details of the process, the weld joint performance will be investigated.

Considering Fig. 15, the laser beam welding process modeling is a thermo-mechanical-metallurgical process, which is based on temperature; thus, it is expected to assume physical material properties of the process as the temperature-dependent in modeling. The physical material properties can be categorized into (1) thermal and (2) mechanical properties. Thermal conductivity, density, and specific heat are thermal material processes, and mechanical material properties include Young's modulus, yield strength, Poisson's ratio, and thermal expansion coefficient. The thermal properties and mechanical properties of low carbon steel (Q235), as an example are shown in parts A and B of Fig. 16. Some studies [72–74] proposed JMatPro software for material properties considered in LBWPM methods.

3 Geometrical characteristic modeling's case studies

As discussed in Section 2.1.1, geometrical characteristic modeling is one of the critical characteristics of the LBW process. In this section, some recent case studies on modeling of these characteristics, including weld width, penetration, and distortion, will be presented in separate subsections as follows.

3.1 Weld width and penetration

Weld width and weld penetrations are two critical weld geometrical characteristics, which was the aim of masses of studies of LBW modeling. According to the shape of weld penetration, LBW is categorized into five penetration modes (or P modes) including (1) conduction; (2) transition; (3) keyhole: partial; (4) keyhole: full (wide root); and (5) keyhole: full (thin root). The weld shape and schematic of this category is provided in Table 6.

The conduction mode of the LBW process has some advantages, including no cracks, porosity, and undercut with no spatter [90]. On the other hand, the keyhole laser beam welding mode has more applications than the conduction mode [91, 92]. These modes are separated based on applied power density on the weld area. The power density is defined as laser power divided by laser beam area. In the keyhole mode, the power density is high enough to vaporize material and produce a hole in the melt pool, while, in the conduction mode, the power density is insufficient to provide vaporization [93]. The boundary between keyhole and conduction modes is unclear and is defined as a transition mode. The transition mode is influenced by the material thermal properties, including melting temperatures, thermal conductivities, density, specific heat capacity, latent heat of melting, and latent heat of vaporization [76]. All three conduction, transition, and keyhole modes were based on power density for different materials, including stainless steel 304L, aluminum 2024-T3, and mild steel S355 in parts A, B, and C of Fig. 17, respectively.

The schematics, experimental and numerical, of three modes of keyhole laser beam welding, including partial penetration; full penetration: wide root; and full penetration: thin root, are shown in parts A to F of Fig. 18. In part A of Fig. 18, the conductive melting is provided by redirecting downward flow upwards for partial penetration. When the melt is redirected upwards sufficiently, preventing any melt from flowing backward to form humps, and the upward flow and melt solidification behind the keyhole are not high enough to form a root concavity, a flat root
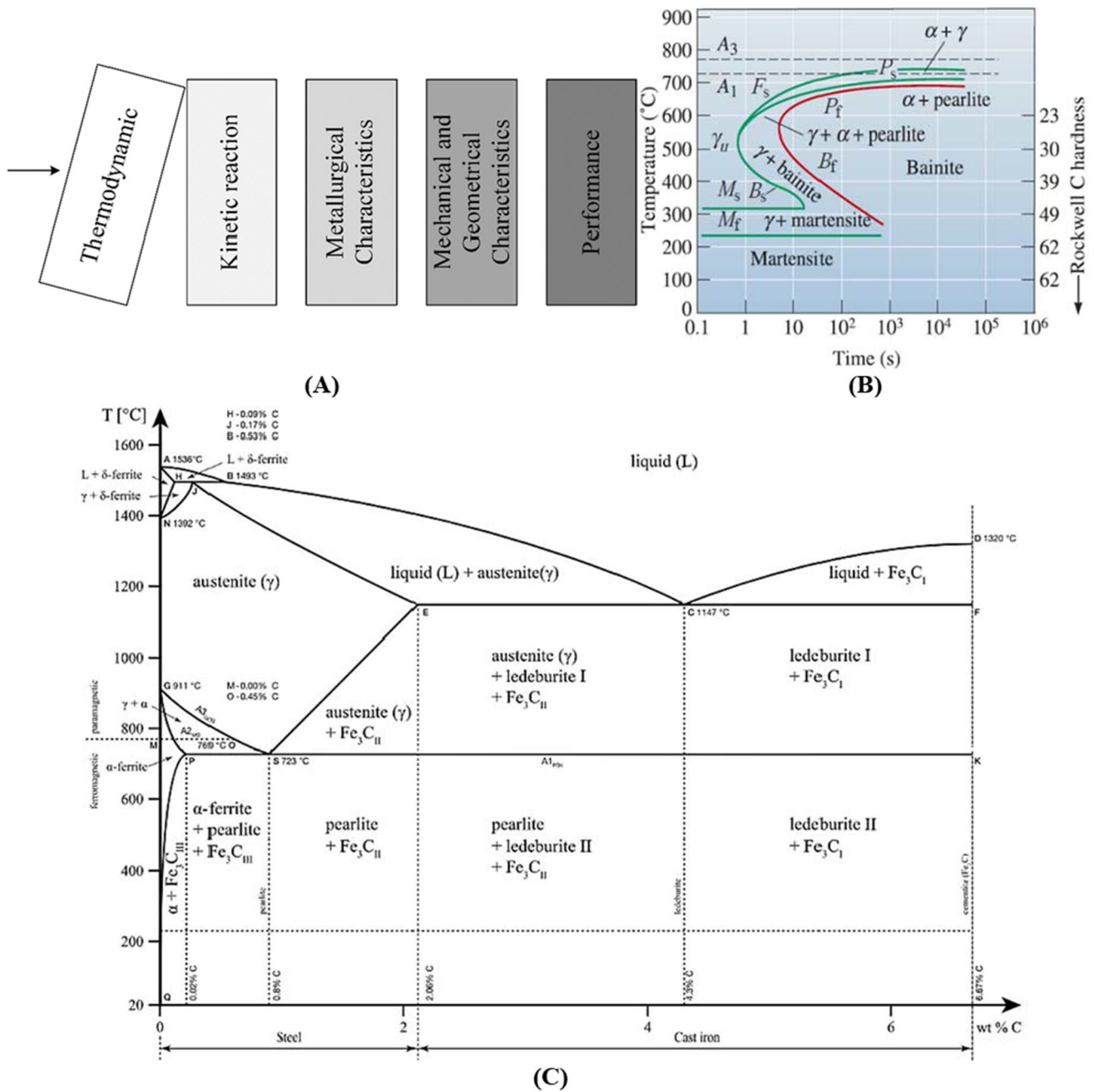
Fig. 15 **A** The relationship between thermodynamic properties, kinetic reactions, metallurgical, mechanical, and geometrical characteristics and the performance of laser beam welding process. **B** Time–temperature transformation (TTT). **C** Phase diagram [71]

will be formed, as shown in part B of Fig. 18. A wider melt width allows more melt to flow after the keyhole exit, allowing inappropriate amounts of melt to flow to the end of the melt pool so that humps may form, as shown in part C of Fig. 18.

Different types of modeling were studied for five laser beam welding penetration modes and weld width during the last decades. The summary of presented studies based on the material of base metal, thickness, types of modeling

(monitoring, approach, and methods), weld width, weld penetration, and error of verification of model is provided in Table 7. In this table, Post, Off, Num, ML, Reg, *W*, and *P* refer to post-process, offline, numerical, machine learning, weld width, and weld penetration of the LBW process, respectively.

Melt pool behavior and transmission mechanism during the LBW of dissimilar metals was studied by a 3D transient numerical model (FLUENT) by considering of fluid flow,
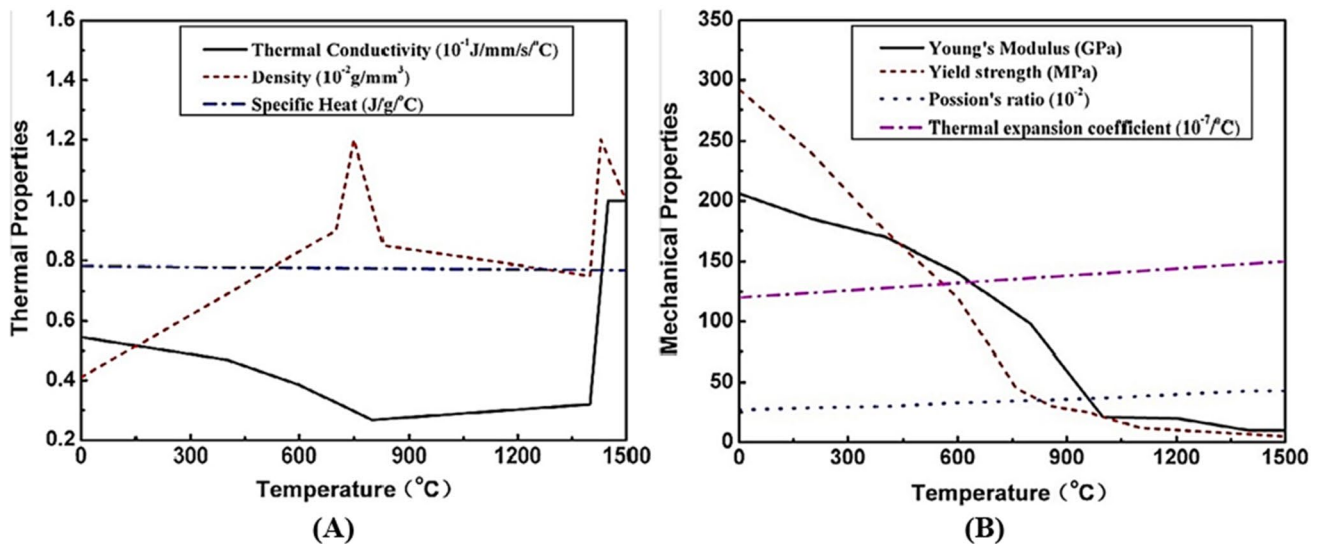
Fig. 16 Physical properties versus temperature of **A** thermal properties and **B** mechanical properties for low carbon steel (Q235) [70]

heat transfer, keyhole evolution, and mass transport [94]. The effects of recoil pressure and surface tension on the keyhole wall, convection, diffusion, and keyhole formation on the mass transfer were considered in this study. The processing parameters included laser power (1800–2000 W), welding speed (0.055–0.075 mm/s), beam focus, and heat input (26.67–32.73 J/mm). The model was validated by another study with a heat input of 36.3 J/mm, as shown in part A of Fig. 19 [95]. Furthermore, the simulation detail is also provided in part B of Fig. 19.
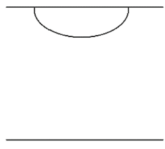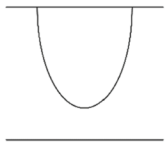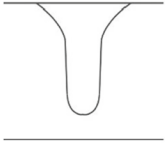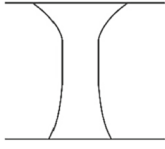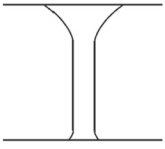
Maximum geometrical characteristics, including weld width and weld penetration, were reported 1.383 mm and 1.4 mm, respectively. The maximum liquid velocity and temperature of the molten pool were provided at 30.1 m/s and 3800 K, respectively, with laser power of 2000 W. Based on this study, it is concluded that convective heat transfer was dominant, and convection and diffusion were the main mechanisms of metal mass transport. It is also reported that a decrease of heat input per unit area leads to decrease in fluid flow, element diffusion, and thickness of the intermetallic transition layer. Another numerical model based on ANSYS FLUENT software combined with a high-speed camera was studied on geometrical characteristics of weld and its relationship with inconsistent thermodynamic behaviors of keyhole [96]. Further details are provided in Table 7.

Computational fluid dynamic (CFD) using ANSYS software, which is a numerical modeling considering hybrid conical-cylindrical heat source (shown in part A of Fig. 20) concerning the heat transfer, molten fluid flow weld pool dynamics, and cooling rate phenomena, was studied [97]. The material was stainless steel 316LN with a thickness of 5.5 mm, and the processing parameter was laser power (1–3.5 kW), which leads to a variation of Marangoni number

(1813–22,623) and Péclet number (26.38–135.08). By considering heat loss including convection and radiation heat transfer, the maximum error between experimentally measured and the predicted model was 11% (part C of Fig. 20). According to the recoil pressure contour and velocity field (part B of Fig. 20) and cross-sectional view of the laser keyhole (part C of Fig. 20), it is concluded that once the material surpasses the evaporation temperature, metallic vapor starts expelling from the cavity formed due to intense laser power density. The direction of the vapor flow is towards the outflow boundary. As the keyhole forms, the recoil pressure in contact with the vapor plume drives down along the keyhole wall forming a circulation loop. There is variation in the velocity values around the keyhole, as the value is dependent on the processing parameters. The maximum pressure for the maximum weld temperature was reported to be around 133 kPa, which was in agreement with previous studies [98, 99].

Considering Table 7, a summary of models based on weld width, penetration, and types of modeling and error, it can be deduced that both post-process (Post) and in-process, including online (On) and offline (Off), are studied for various materials such as different types of steels, Al alloy, Cu alloy, and polymer with a thickness of 0.2–20 mm. Different approaches, such as exact and numerical (Num) methods like FEM-based software (FLUENT, ANSYS, CFD, COMSOL), finite difference method–based techniques, and machine learning (ML) approaches such as Fuzzy, CNN, ANN, GABP, PCA/GA, as well as empirical-based methods (Empirical) like Regression, SVR, and ANOVA, are conducted to predict weld width and weld penetration with an error range of 0.001–66%, which indicates a high broadband range.

Table 6 Classification of the laser beam welding process based on penetration modes (P modes)

| Row	P Mode	Weld shape	Schematic	Reference
1	Conduction	Horizontal elliptic: Wide at the top + shallow penetration and very low aspect ratio		[75, 76]
2	Transition	Vertical elliptic: Wide at the top + medium penetration and low aspect ratio		[75, 76]
3	Keyhole: Partial	Bell shape: Wide at the top + Semi-cylindrical in penetration		[77-81]
4	Keyhole: Full (Wide Root)	Hourglass shape: Wide at the top and root + Semi-cylindrical in penetration		[77, 82-86]
5	Keyhole: Full (Thin Root)	Wide at the top + Semi-cylindrical in penetration + Minor widening at the root		[77, 83, 85, 87-89]
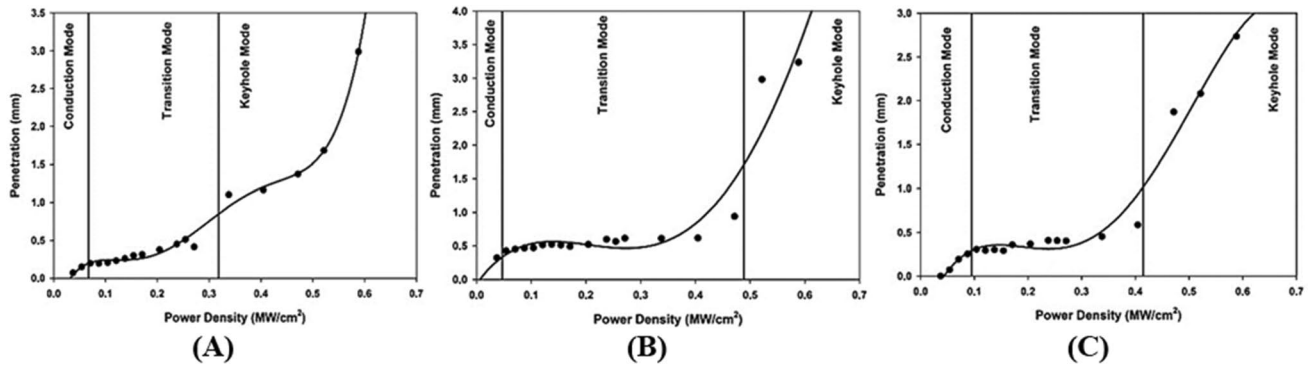
Fig. 17 Penetration depth vs power density of LBW process including conduction, transition, and keyhole modes for **A** stainless steel 304L, **B** aluminum 2024-T3, and **C** mild steel S355 [76]
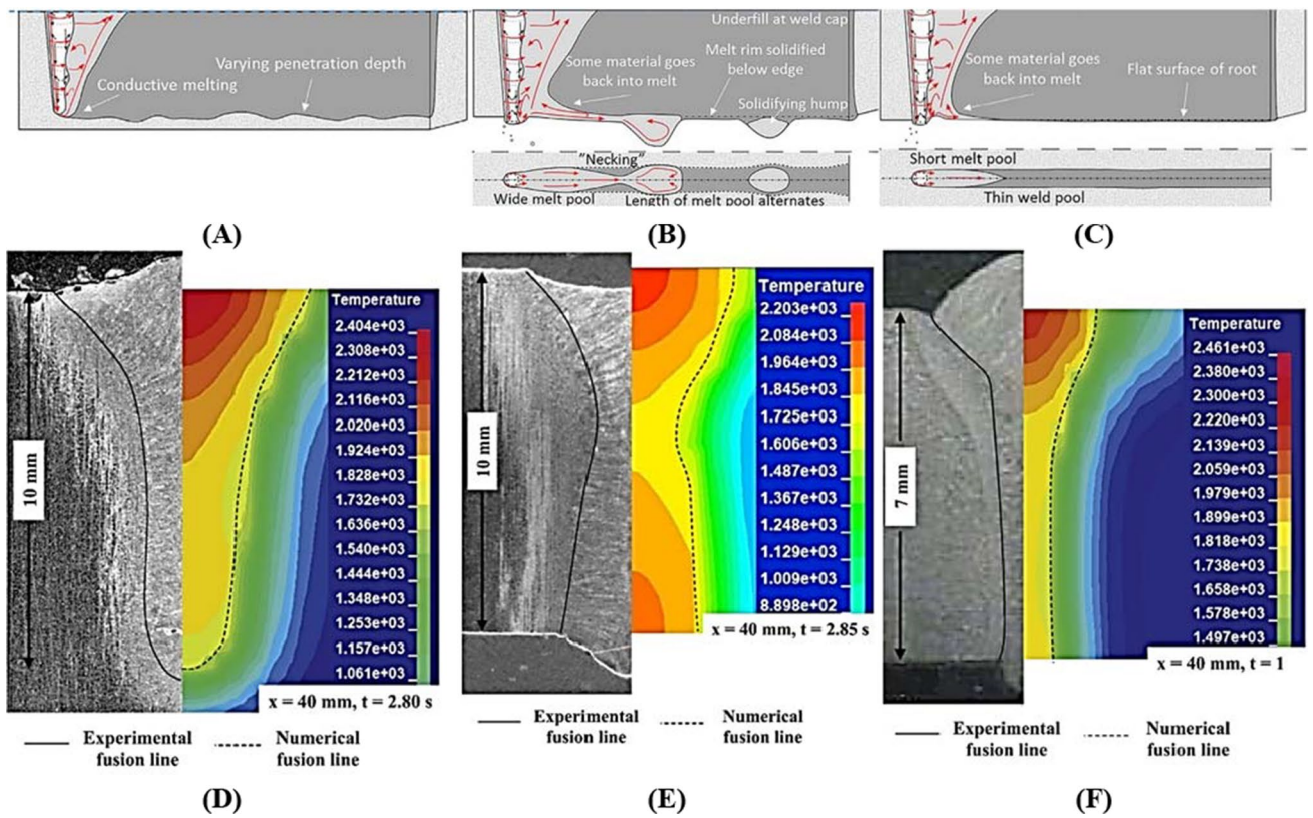
Fig. 18 Different laser beam welding penetration modes. **A** Schematic of partial penetration. **B** Schematic of full penetration: wide root. **C** Schematic of full penetration: thin root. **D** Experimental and numerical of partial penetration. **E** Experimental and numerical of full penetration: wide root. **F** Experimental and numerical of full penetration: thin root [77]

Comparing online models (which have an error of less than 6%) with offline models, it is deducted that online models have an accuracy higher than offline ones. This is because most of the instantaneous changes of the process are considered in them, and the results' output of the models will be compared to experimental results.

3.2 Distortion

During the laser beam welding process, thermal contraction of weld metal, and solidification shrinkage, the workpiece tends to deform [39]. Welding distortion or deformation is one of the geometrical characteristics, which is considered

Table 7 Summary of presented studies based on weld width, penetration, and types of modeling and error

Row	Year	Material	Thickness (mm)	Types of modeling based on			Max			Ref
				Monitoring	Approach	Method	W (mm)	P (mm)	Error (%)	
1	1996	Mild steel 1010–1035	NR	Post	Exact	2D heat conduction	2.8	6.5	NR	[100]
2	1997	Austenitic stainless steel	NR	Off	Exact	Energy absorption mechanism	5	5	37	[101]
3	1999	SS 1020	9.5	Off	Num	FDM	2	9.1	NR	[102]
4	2000	Steel 1018	3.17	Off	Num	FEM	3.8	NR	NR	[103]
5	2001	Al 5182	1	Off	Exact	Heat conduction	0.44	1.35	5.4	[104]
6	2002	Steel	1.6–2	On	ML	Fuzzy	1.77	NR	NR	[105]
7	2004	Austenitic stainless steel	6.5	Post	ML	Fuzzy logic/ANN	NR	6.5	0.45	[106]
8	2004	TC1	1.5	Off	Num	FEM	0.6	1.5	NR	[107]
9	2005	Medium Carbon Steel	5	Post	Reg	ANOVA	2.703	4.407	6.11	[108]
10	2008	WE43	10	Off	Num	FLUENT	2.5	10	NR	[65]
11	2010	SS 304	1.6	Post	ML	ANN	1.45	0.96	4.6	[109]
12	2010	SS 304	6	Post	Reg	ANOVA	NR	3	NR	[110]
13	2010	AA5083	5	Off	Num	ANSYS	2.8	NR	10	[111]
14	2011	SS 304	6	Post	Reg	ANOVA	NR	3.4	10	[112]
15	2015	SS 304/ Mg AZ31B	2	Post	ML	ANN	NR	2.1	3	[113]
16	2015	NR	NR	Off	ML	GABP	0.77	2.176	5.3	[114]
17	2017	NR	NR	Post	Reg	SVR	3.5	NR	1	[115]
					ML	ANN	3.5		2	
18	2018	316L	7	Off	Num	CFD	4.4	7	32.67	[73]
19	2018	Steel S355J2G3	15	Off	Num	CFD/COMSOL	1.5	15	NR	[116]
20	2018	Steel EH36	4	Off	Num	ANSYS	2.125	4	15.6	[117]
21	2019	Ti6Al4V	1	On	ML	PCA/GA	2.12	NR	4.5	[118]
22	2020	TRB	2	On	ML	CNN	NR	1.8	5.4	[48]
23	2020	SS316L	2	Post	ML	GA/BPNN	2.06	NR	0.001	[119]
24	2020	Ti6Al4V	1–1.5	Off	Num	NR	1.5	1	66	[120]
25	2021	HT780 steel	20	Off	Num	FEM	NR	20	NR	[77]
26	2021	Al-Si coated	1.5	Off	Num	CFD/COMSOL	1.6	1.5	NR	[121]
27	2021	Ti-6Al-4 V and Inconel 718	3	Off	Num	NR	1.5	3	22.00	[69]
28	2021	Ti-Grade 5	2	Post	Reg	ANOVA	0.97	0.41	5.00	[122]
29	2021	AA2024	2	Off	Num	COMSOL	2.2	2	5.63	[68]
30	2021	SS316L	10	Off	Num	FLUENT-ANSYS	NR	7.28	NR	[96]
31	2021	DP600-AA6082	3	Off	Num	FEM	1.4	1.383	NR	[94]
32	2021	SS316L	1	Off	Reg	ANOVA	1.98	1.51	54.37	[123]
33	2022	SS316NL	5.5	Off	Num	ANSYS	2.2	5.5	11	[97]

Table 7 (continued)

Row	Year	Material	Thickness (mm)	Types of modeling based on			Max			Ref
---	---	---	---	Monitoring	Approach	Method	W (mm)	P (mm)	Error (%)	
34	2022	SS301L	0.6	Off	Num	FE	0.7	0.6	9.41	[124]
35	2022	Al-Si coated	1.5	Off	Num	ABAQUS	NR	1.5	22.00	[125]
36	2022	SS316L	10	Off	Num	SYSWELD	2.98	2.168	5	[126]
37	2022	iPP	2	Off/Post	Num/Reg	COMSOL/ANOVA	1.7	NR	4.42	[127]
38	2023	Q235B	7.6	Off	Num	FLUENT/ANSYS	6.95	6.71	14.4	[128]
39	2023	AA5754-AA6005	3	Off	Num	COMSOL	4.1	3	10.1	[30]
40	2023	Al 2219	9	Off	Num	ANSYS	6.9	6.5	5	[129]
41	2023	Al 6082	6	Off	Num	ANSYS-FLUENT	3.20	4.5	16	[130]
42	2023	Invar alloy	3	Off	Num	FLUENT	3.29	3	NR	[131]
43	2023	AA6061	5	Off	Num	NR	3.94	5	12	[132]
44	2023	Al-Cu	0.2 Al/1 Cu	Off	Num	Flow-3D	0.32	0.19	15.6	[133]
45	2023	SS 301L	4	Off	Num	CFD	2.80	3	9.90	[134]
46	2023	S A710	6	Off	Num	FEM	4.32	3.15	0.033	[135]

NR not reported, *SVR* support vector regression

a critical issue in the manufacturing process. The distortion restricts and directly affects the assembly and quality of products, especially for thin-plate structures. Thus, the prediction of distortion of laser beam welding is particularly essential for both the design and manufacturing stages. Hence, some studies have been focused on the modeling of distortion, which has been produced during the laser beam welding process, some of these are provided in Table 8.

According to Table 8, the summary of presented distortion models is categorized based on monitoring, approach, and methods with the error of method. The deformation of low carbon steel (Q235) thin-plate (with a thickness of 2.3 mm) was modeled numerically using the thermos-elastic–plastic three-dimensional finite element method [70]. Two types of theories, including large deformation (case A) and small deformation (case B) were considered, as shown in parts A and B of Fig. 21, respectively. The model was verified by experiment specimen with processing parameters including laser power of 2400 W, welding speed of 1.8 m/min, shielding gas flow rate 10 L/mm, and focus length of 200 mm, as shown in part C of Fig. 21. Different results were concluded. Firstly, it is concluded that longitudinal bending is too small, while transverse bending (angular distortion) is noticeable. Secondly, the prediction of case A with large deformation theory matches the measurements in magnitude better than case B (with small deformation theory). Thus, for accurate prediction, the large deformation theory is recommended to simulate the thermo-mechanical behavior of the thin-plate laser beam welding process.

To provide fast prediction of deformation in laser-welded thin sheets, a local solid (with a length of 80 mm) and a global model were studied based on inherent strain theory [136]. The inherent strain theory is defined, as the summation of plastic strain, thermal strain, and creep strain, and strain induced by phase transformation [137]. The schematic of inherent deformation, including in-plane shrinkage and longitudinal bending, is shown in part A of Fig. 22. FEM-based model of thermo-elastic–plastic analysis (procedure is provided in part B of Fig. 22) was validated by experimental results of out-of-plane welding deformation on stainless steel 301 with a thickness of 1.33 mm, laser power of 1500 and 1600 W, and welding speeds of 1.2 and 2 m/min. The deformations of specimens were measured by altimeter, as shown in part C of Fig. 22. The maximum deflection of 15 mm (which is over ten times of plate thickness) is provided via a speed of 2 m/min. Three geometrical imperfections were applied as an initial geometric shape of the plate, including − 10, 0, and + 10, and the range of produced curvature was calculated as shown in part D of Fig. 22. Thus, it is concluded that if the plate has a positive curvature (or convex shape) and negative curvature (or concave shape), it leads to convex and concave final deformation shapes during the LBW process, respectively.
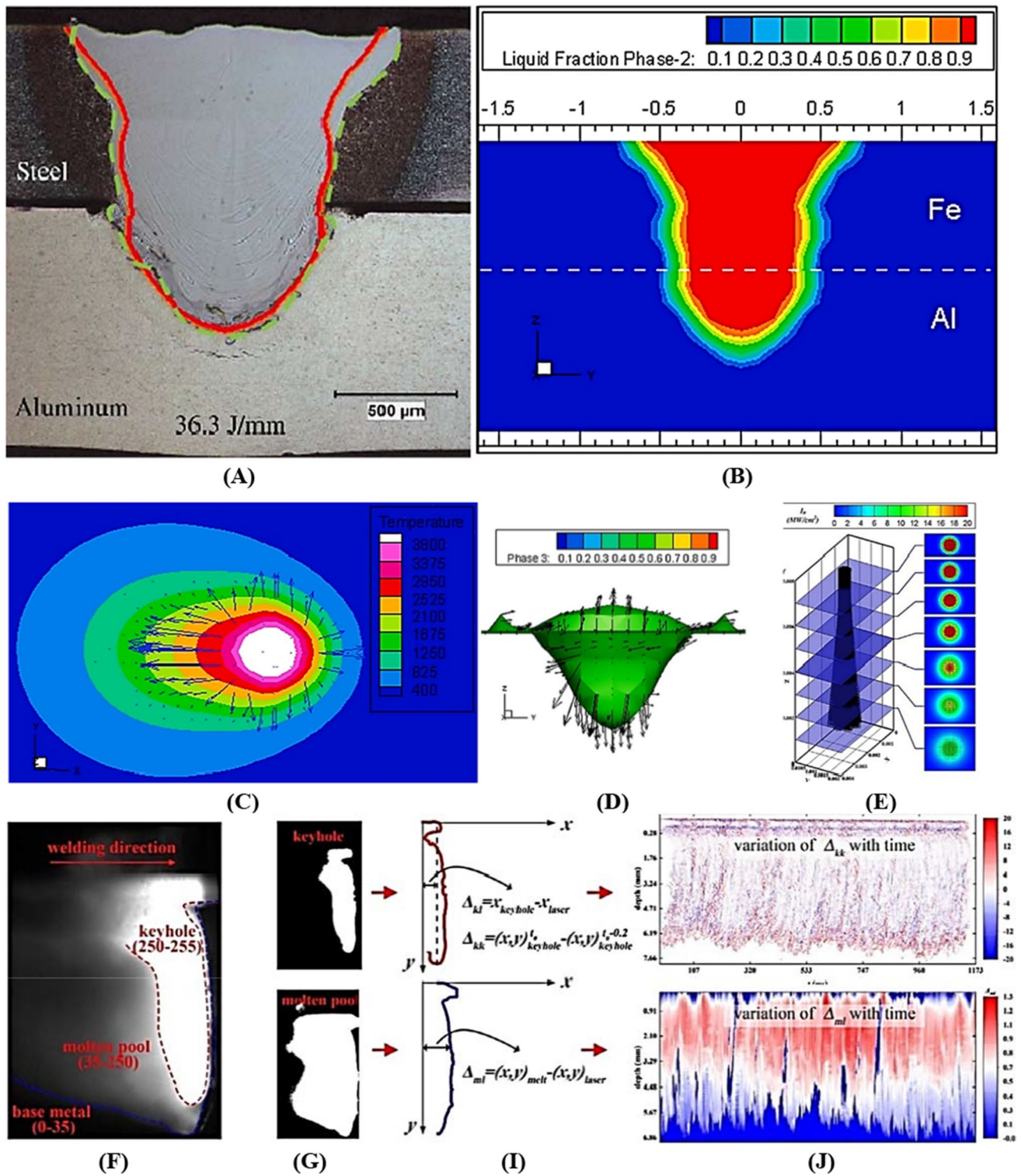
Fig. 19 Numerical LBWPM by FLUENT. (A) Welding experiment specimen with fusion lines (real red line: simulation, green dotted line: experiment) [95]. (B) Cross-section of the simulation [94]. (C) Top view of the temperature and velocity [94]. (D) Iso-surface of the keyhole [94]. (E) Schematic of the ray tracking heat source model [96]. (F) Raw image taken by high-speed camera [96]. (G) Binarized image of the keyhole and molten pool regions [96]. (I) Edge extraction and quantification [96]. (J) Density map made by arranging keyhole (upper) and molten pool (the lower one) [96]
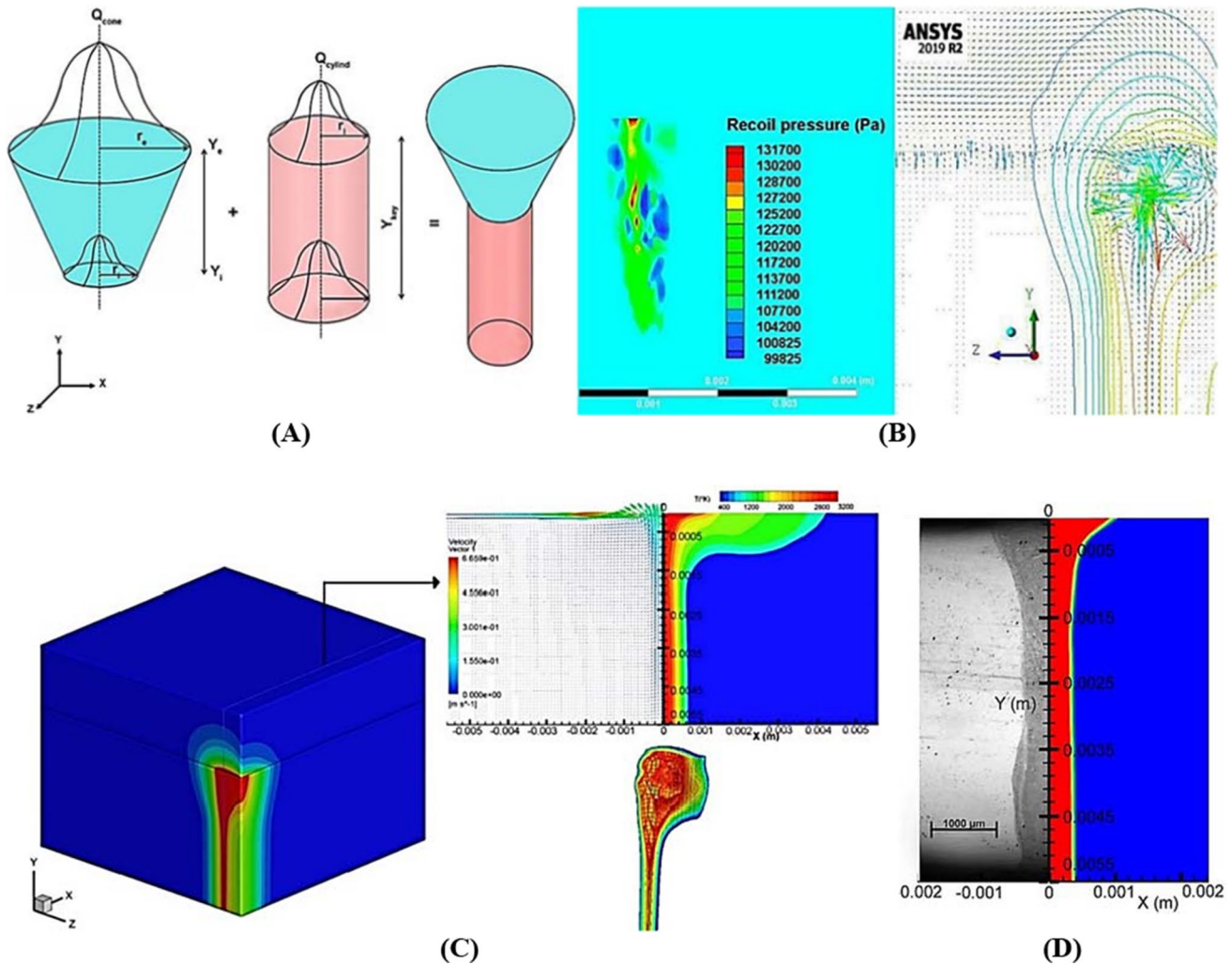
Fig. 20 Numerical LBWPM by ANSYS. **A** Schematic of hybrid conical-cylindrical heat source. **B** Recoil pressure contour and velocity field. **C** Cross-sectional view of laser keyhole. **D** Experimental and predicted weld bead cross-section comparison for laser power 3.5 kW [97]

Considering Table 8, different results can be concluded. Firstly, most distortion modeling is offline in terms of monitoring and numerical approach with commercial FEM-based software such as ANSYS and SYSWELD with all the types of distortions. Secondly, online analytical models did not consider previous distortion models, while just one post-process based on regression (ANOVA) reported no errors. Thirdly, the maximum error of distortion models is 5–38.7%, which is less than 40%, for base metal thickness of 0.6–10 mm and distortions of 0.24–15 mm. This indicates that further studies should be considered to reduce the maximum error of models to predict distortion with higher accuracy.

4 Metallurgical characteristic modeling's case studies

The following subsections, the presented LBW modeling of each of the metallurgical characteristics, including solidification mode, phase transformation, and morphology, will be introduced and discussed.

4.1 Solidification mode and phase transformations

During the solidification of a weld, there is a zone including both solid and liquid phases, a mushy zone in which a tensile strain is included due to its shrinkage and thermal

Table 8 Summary of presented studies based on weld distortion, types of modeling, and error

| Row	Year	Material	Thickness (mm)	Max temp (K)	Types of modeling based on			Types of distortion	Max		Ref
					Monitoring	Approach	Method		Distortion (mm)	Error (%)	
1	2013	NR	3	NR	Off	Num	ANSYS	Out-of-plane deformation	0.52	NR	[138]
2	2014	Q235 Steel	2.3	2873.15	Post Off	Reg Num	ANOVA FEM	Transverse shrinkages, longitudinal shrinkage, out-of-plane deformation	8	NR	[70]
3	2016	SS 316L	5	1723	Off	Num	FEM	Angular deformation	2.5	5.95	[139]
4	2016	SS301	1.33	3487	Off	Num	FEM	Buckling distortion	15	5	[136]
5	2016	Q235 Steel	6	3573	Off	Num	FEM	Longitudinal deformation	0.17	NR	[72]
6	2017	316L	3.8	2783.15	Off	Num	FEM	Angular deformation	0.58	23.4	[140]
7	2017	SS301L	1.33	2123	Off	Num	ANSYS	Transverse/longitudinal deformation	4	NR	[141]
8	2019	SS316L	5	3403	Off	Num	ANSYS	Angular deformation	0.46	5.84	[142]
9	2021	DP 600 Steel	1.6	2523	Off	Num	SYSWELD	Transverse deformation	15	NR	[54]
10	2021	SS 304-AA6082 T6	1.5	723.15	Off	Num	ANSYS	Shrinkage/angular deformation	1.2	38.7	[143]
11	2021	SS 316LN	5.6	2068	Off	Num	SYSWELD	Longitudinal deformation	0.24	NR	[144]
12	2022	SS301L	0.6	2573	Off	Num	FEM	Transverse/longitudinal deformation	2.5	9.41	[124]
13	2022	SS316L	10	1673.15	Off	Num	SYSWELD	Angular distortion	0.47	14.35	[126]
14	2023	AA 5024	1.6	928	Off	Num	Simufact welding	Transverse/longitudinal deformation	1.05	NR	[145]
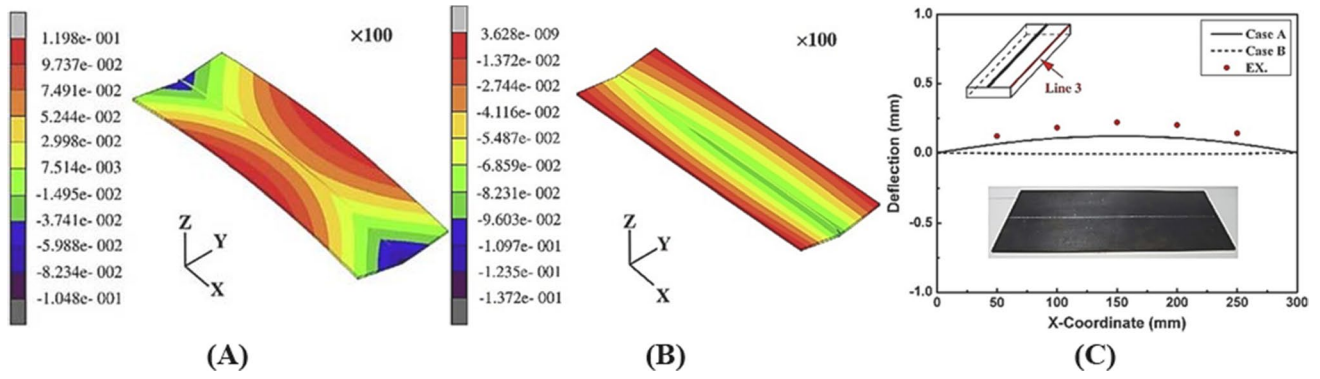
Fig. 21 Modeling of deformation of LBW process. **A** Deformation of modeled of case A. **B** Deformation of modeled of case B. **C** Experimental and modeling of line 3 of cases A and B [70]
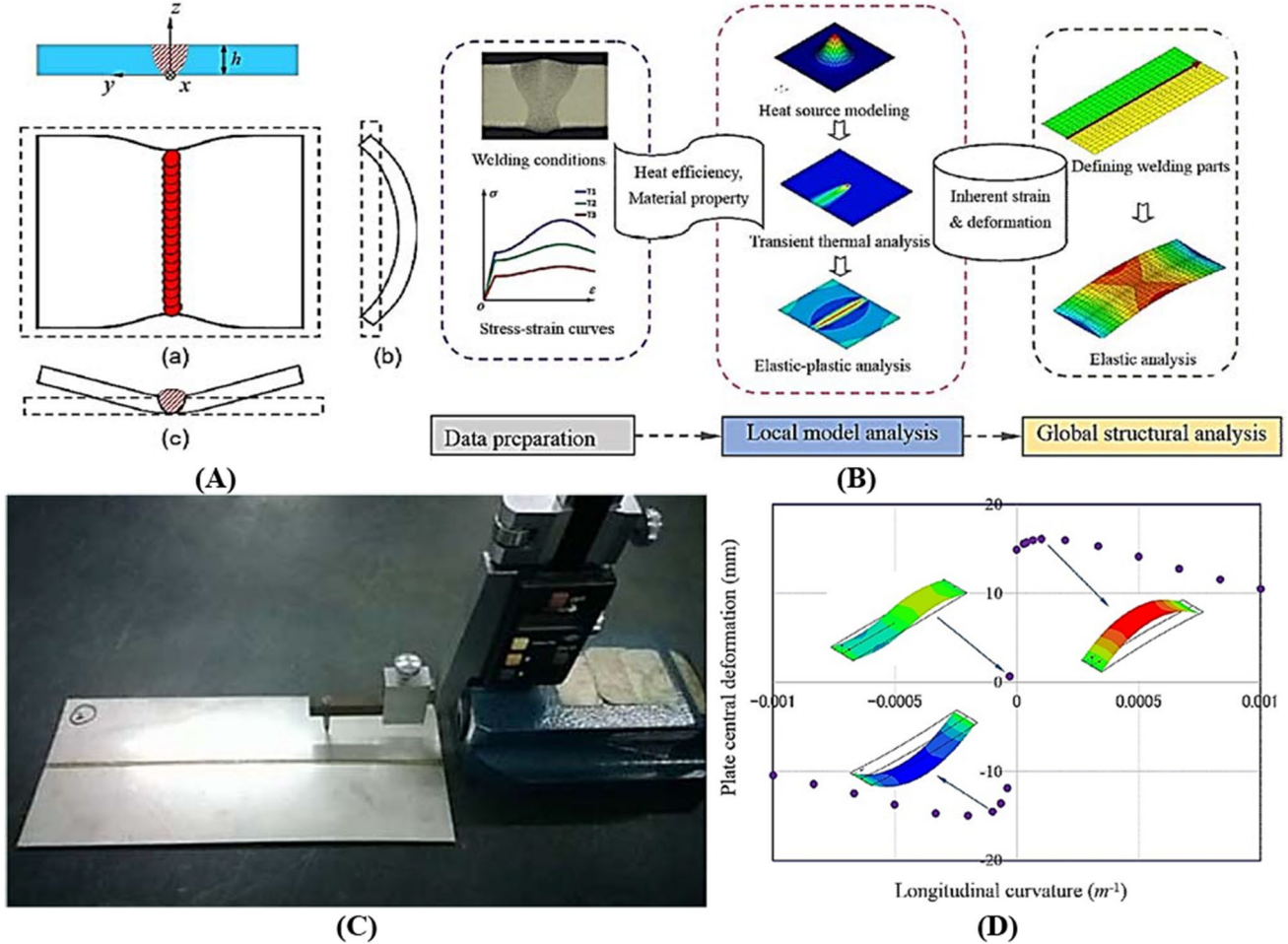

Fig. 22 Modeling of deformation of LBW process. **A** Schematic of inherent deformation including in-plane shrinkage (a) and longitudinal bending (b). **B** The deformation calculation procedure. **C** Experimental set up for measurement. **D** Plane central deformation versis longitudinal curvature [136]

contraction and resistance of the cooler base metal [146]. This strain can cause solidification cracking [147]. The schematic of a mushy zone, axial grains, partially melted metal, and columnar grains is shown in parts A and B of Fig. 23, with a general and detailed view, respectively. Cracking in this zone of the weld is prevented when the flow of the inter-dendritic liquid can compensate for the local deformation. In other words, when the space between the deformed dendrites is filled with enough liquid, the solidification crack is healed [148, 149]. Thus, it can be concluded that solidification mode and phase transformations, which affect the mushy zone, play a critical role in solidification cracking, which is a noticeable criterion for weld performance.

As discussed in "Solidification mode and phase transformations," in pure metal solidification, the solid/ liquid (or S/L) interface is usually planar unless the metal is subjected to sudden supercooling. While the solidification of alloys, the S/L interface can be broken into cellular or dendritic structures. The formation of each of the structures depends on the solidification conditions and the material. As shown in Fig. 24, there are four basic solidification modes, including planar, cellular, columnar dendritic, and equiaxed dendritic modes [147].

Although studies have been focused on metallurgical characteristics of the LBW process modeling, because of the limitations of the monitoring process, the observation of the solidification process during the process in real-time is challenging. Thus, most recent studies proposed numerical methods of modeling, some of which are presented in Table 9. It is reported that primary dendritic arm spacing (PDAS) and secondary dendritic arm spacing (SDAS) are related to G and R based on Kurz and Fisher as follows [152]:

$$\lambda = A \times G_{\mathrm{T}}^{-\mathrm{n}} \times R^{-\mathrm{m}} \tag{8}$$

where A, n, and m are LBW process coefficients, and some of the studies have focused on it. A combination of numerical- and empirical-based methods were considered to model the microstructure of the mixing of steel and aluminum [143]. The models were validated by stainless steel 304 and 6082-T6 aluminum with a thickness of 1.5 mm, laser power of 3750 W, and welding speed of 4.2, 4.8, and 5.4 m/min. The steel and aluminum weld parts were considered, as zones A and B, respectively, as shown in parts A and B of Fig. 25. The calculated versus measured average aluminum concentrations within welds with penetrations depths 240, 320, 500, and 800 μm are presented in part C of Fig. 25. The correlation of the aluminum concentration in the whole weld (Al_{W}) to the average concentrations in zones A (Al_{A}) and B (Al_{B}) is provided in parts D and E of Fig. 25, respectively. Using obtained empirical relations, the average aluminum concentration in zones A and B can be calculated as $Al = 0.82 \times Al_{\mathrm{W}}$ and $Al_{\mathrm{B}} = (0.05 \times (A_{\mathrm{st}}/A_{\mathrm{al}}) + 1.15) \times Al_{\mathrm{W}}$. Thus, it is concluded that there is a significant difference in the Al concentration in the upper and lower zones of the St-Al welds. Because the thermal expansion coefficient and elastic–plastic properties of the weld metal are functions of the Al concentration, both zones should be considered in the computational model.

The summary of presented studies based on weld microstructure and the types of modeling and errors are provided in Table 9. It can be concluded that most of the models are based on offline monitoring processes and numerical approaches with errors of 5.5–22.22%, besides the post-process-based regression model. The materials which have been considered for weld microstructures are various types of steel and Al alloy with thickness of 1.5–10 mm. All the numerical microstructure models are based on finite element methods and software such as SYSWELD, CFD, and ANSYS. Although the maximum
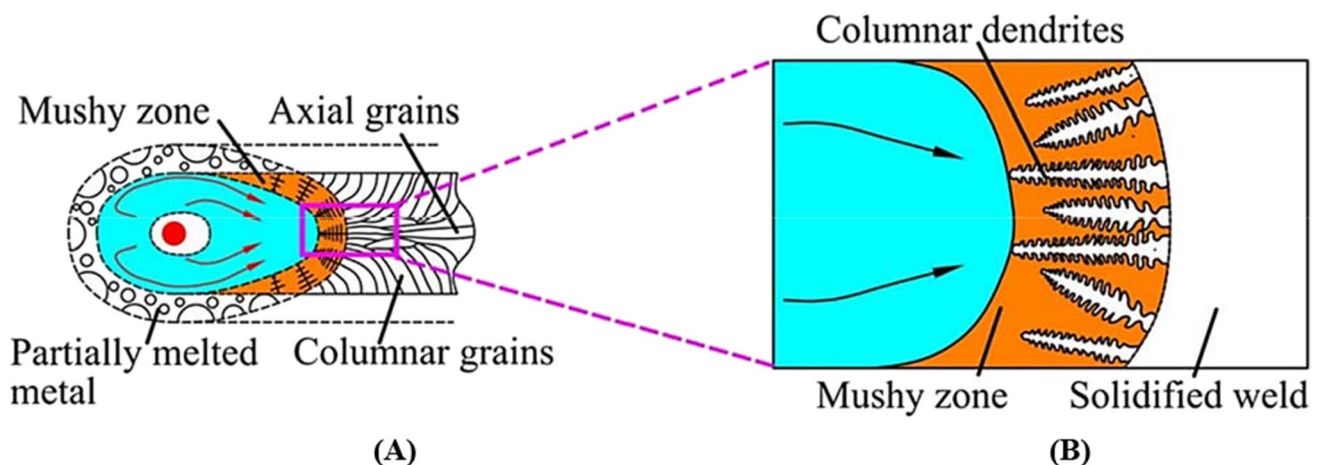

Fig. 23 The schematic drawing of the influence of melt flow on microstructure formation. (**A**) General view including mushy zone, axial grains, partially melted metal, and columnar grains. (**B**) Detailed including mushy zone, columnar dendrites, and solidified weld [150]
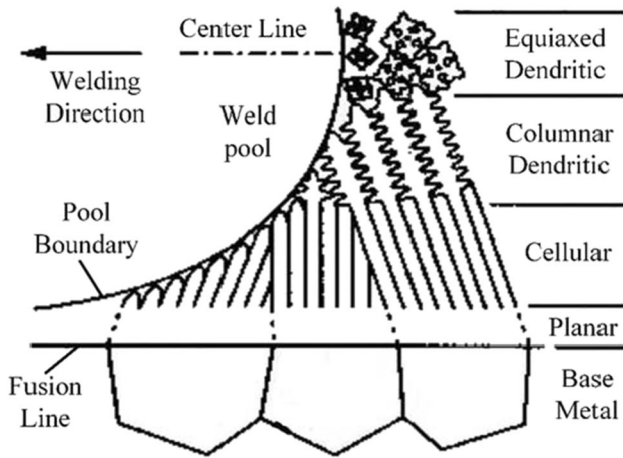
Fig. 24 Schematic of basic solidification mode across the fusion zone including planar, cellular, columnar dendritic, and equiaxed dendritic modes [151]

error of presented models is less than 30%, most of the models did not present a closed-packed formula (except [143, 153]), which can be applied directly to the process to predict weld microstructure and phases. Thus, the lack of closed-pack online formula is revealed for the LBW process.

4.2 Morphology

In the LBW process, the interaction between the laser beam and the molten pool directly affects the weld morphology [150]. Different studies with different models have been considered to model and simulate the dendrite arm spacing (DAS) of the laser beam welding process, some of which are presented in Table 12 with their types based monitoring and approach, error, and details of LBW process.

The solidification of the melt pool of the laser beam process is a nonlinear process, and it is believed that the transient condition was closer to the steady-state than the natural the solidification process [155]. In this study, the phase field (PF) and cellular automata (CA) methods were considered to predict the dendrite growth during solidification process of the LBW. Comparing the model with experimental results, the maximum error of dendrite arm spacing of Al-Cu was reported to be 25% among three different cases, as shown in part A of Fig. 26.

The simulated microstructure of case A is shown in part B of Fig. 26. The density of initial seeds is high, and the diffusion field interaction of neighboring dendrites is strong. Thus, the competitive growth occurs, and some of the grains will survive competition and block others. The PF model was considered in other studies [156–158].

The microstructure images close to the top surface of the melt pool for the laser welding process with a laser power of 2500 W and welding velocity of 2.5 m/min, along with the

Table 9 Summary of presented studies based on weld microstructure and types of modeling and error

| Row | Year | Material | CR_{Max} (K/s) | Thickness (mm) | Types of modeling based on | | | Formula | Max | | Ref |
					Monitoring	Approach	Method		Phases	Error (%)	
1	2016	Q235 Steel	NR	6	Off	Num	FEM	NA	NR	15	[72]
2	2021	SS A387	4000	10	Off	Num	SYSWELD	$Ms\,(°C) = 539 - 423C - 30.4Mn - 17.7Ni - 12.1Cr - 7.5Mo + 10Co - 7.5Si$	NR	5.5	[153]
3	2021	AH36 steel	NR	6	Off	Num	CFD-FEM	NA	NR	22.22	[154]
4	2021	DP 600 Steel	NR	1.6	Off	Num	SYSWELD	NA	Martensite 1%	NR	[54]
5	2021	SS 304-Al 6082-T6	1273	1.5	Post/Off	Reg/Num	ANOVA/ANSYS	$Al_B/Al_W = 0.05\,(A_{st}/A_{al}) + 1.15$ $\alpha = 18.3 + 0.083Al$	NR	NR	[143]

(A)

(B)

(C)

(D)

(E)
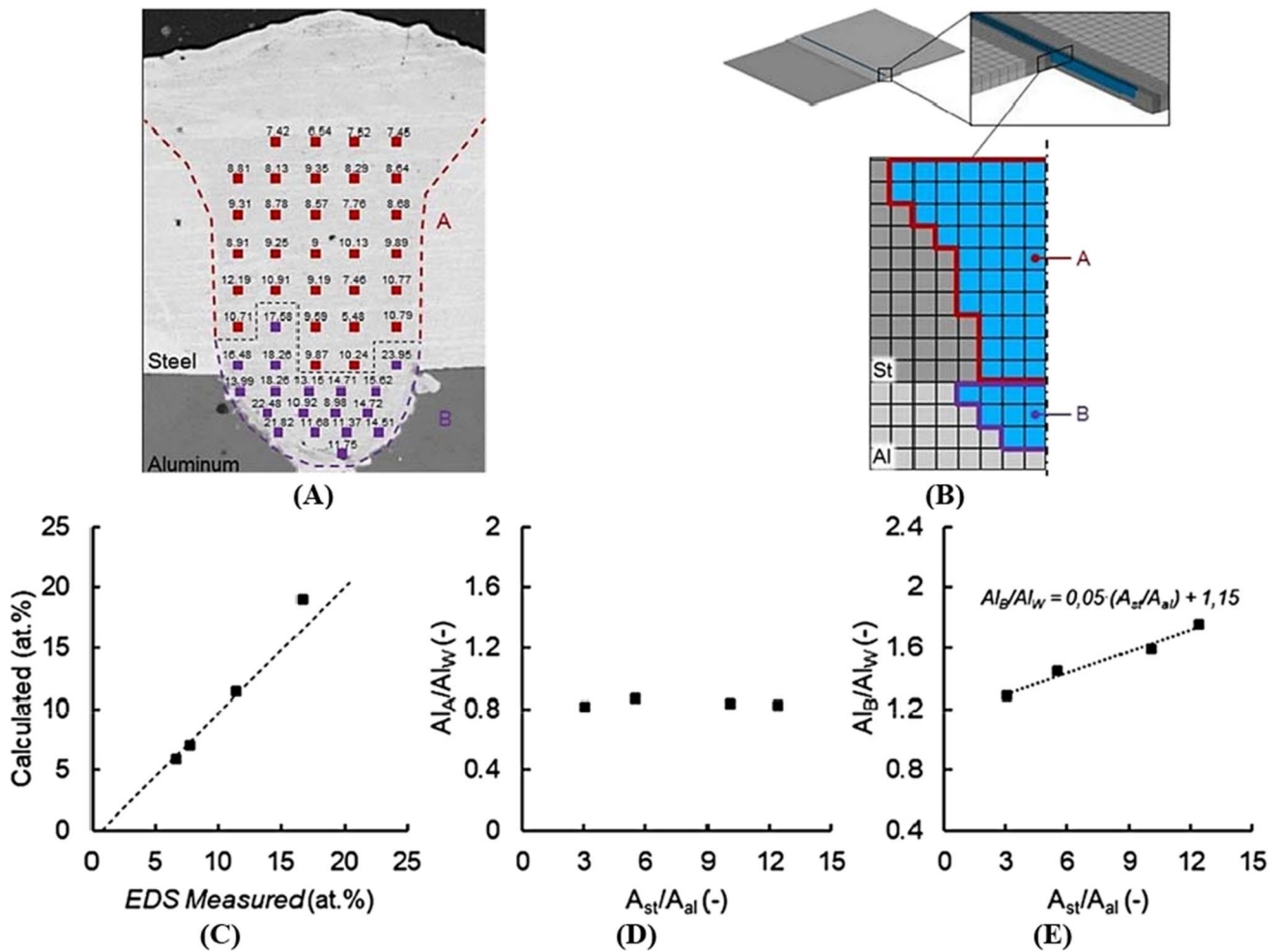
Fig. 25 A EDS analysis of St-Al weld with a penetration depth of 0.5 mm. **B** Zones A and B for the simulations. **C** Calculated versus EDS measured Al concentration in the St-Al weld correlation of the average aluminum concentration in the whole St-Al weld to average aluminum concentrations in **D** zone A and **E** zone B [143]

PF model of it, presented alongside other studies, are shown in parts a and b of Fig. 27, respectively [156]. Regarding Fig. 27, it can be concluded that the phase model can predict the evolution of dendrite growth along the fusion boundary in the laser beam welding process successfully.

Another PF model was established to simulate the columnar-to-equiaxed transition (CET) (shown in Fig. 28) in the entire melt pool of Al-4%wt-Cu alloy 2A12 during the LBW process [158]. The crystalline orientations and heterogeneous nucleation are considered in the proposed model and verified with experimental results in conditions of thickness of 4 mm, laser power of 3000 W, welding speed of 3 mm/s, and defocusing of + 10 mm. EBSD was considered to observe the microstructure of the FZ. Simulation results revealed that crystals initialized as planar ones from the molten pool edge and were then transformed into columnar dendrites during the solidification process.

It was found that dendrites grew toward the center of the fusion zone irrespective of their crystalline orientations. Equiaxed grains grew ahead of columnar dendrites. They gradually formed a belt ahead of columnar dendrites and stopped them from growing. The highest number of equiaxed grains was found at the top edge of the cross-section of the molten pool due to the fastest pulling velocity. The steps of solidification microstructural evolution in the molten pool without CET and with CET are shown in parts a–d and e–m of Fig. 27, respectively. A comparison of FZ microstructure between simulation and experimental results, along with the microstructure of the fusion zone, the microstructure of the equiaxed the grain zone, the microstructure at the center of the equiaxed grain zone, the grain size distribution of the equiaxed grain zone, and the grain size distribution at the center of the equiaxed grain zone are provided in parts a to g of Fig. 28 [158].
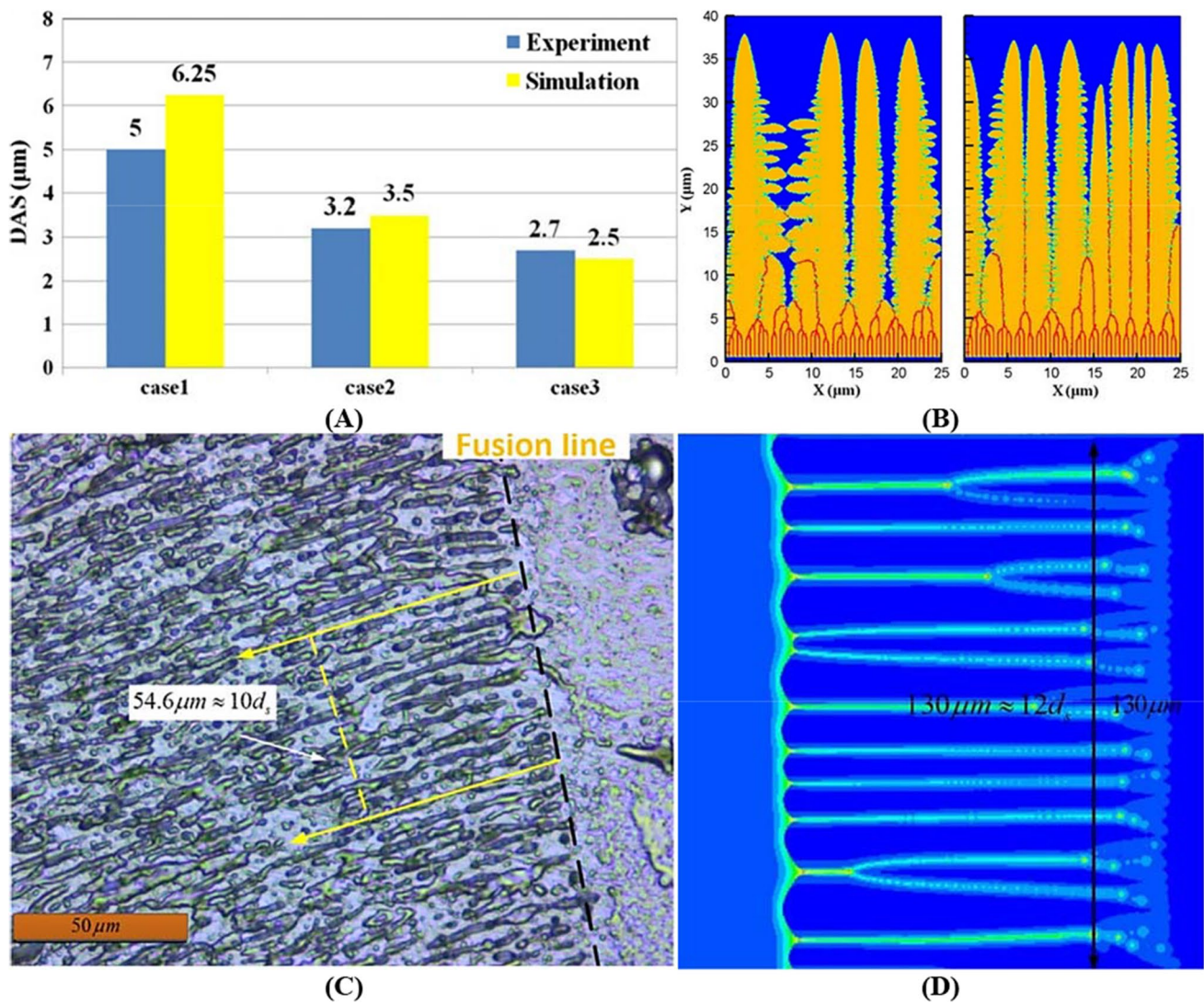
Fig. 26 Microstructures of experimental and simulation results in the laser weld. **A** Experimental and simulated dendrite arm spacing for different cases [155]. **B** Simulated microstructure for laser welding process [155]. **C** Scan image of primary dendrites in the experiment [156]. **D** Dendrite morphology acquired by the phase-field model [156]

As provided in Table 10, it can be conducted that all the presented models are based on offline and numerical methods, including phase field, cellular automata, and finite element methods. The range of predicted grain size is 6.25 to 1000 μm with an error of 1.1–97.8%. Various materials, including steel, Cu alloy, and Al alloy, with the thickness
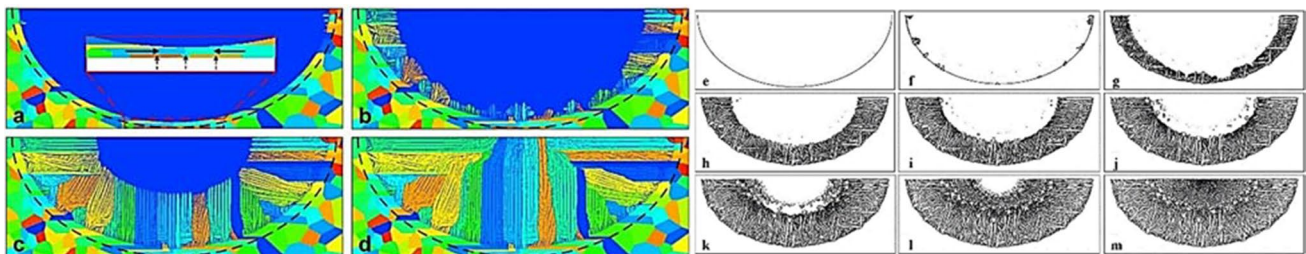

Fig. 27 Solidification microstructural evolution in the molten pool without CET (**a–d**) and with CET (**e–m**) [158]

varying from 1 to 5 mm, have been considered to conduct the model. The maximum cooling rate, which is a critical parameter for modeling, ranges from 410 to 6900 K/s.

5　Mechanical characteristic modeling's case studies

Since mechanical characteristics such as strength, residual stress, and hardness directly affect the performance of weld joints, thus prediction and modeling of them during the LBW process is a crucial issue for welded structure design and life assessment. Therefore, the recent studies, which presented mechanical characteristic modeling of the LBW process, including strength, hardness, and residual stress, will be presented in the following section.

5.1　Strength

Strength is the fundamental mechanical characteristic of laser-welded joints, which directly reflects the welding quality. Some studies have conducted in-depth research on yield strength and ultimate tensile strength of LBWPM, some of which are provided in Table 11. According to Table 11, the presented strength models are

post-process and offline in terms of stage and regression, machine learning, and numerical in terms of the methods. Response surface method (RSM) [160, 161], support vector regression (SVR) [115], kriging [162], and XGBoost [33] are some of methods, which have been provided based on regression analysis to model the strength of laser-welded joints. Neural networks (NN), genetic algorithm (GA) [163], and artificial neural network (ANN) [115, 164] methods have been considered as machine learning categories to conduct models for the prediction of strength in the laser beam welding process (Fig. 29). Different finite element numerical-based software, including ABAQUS [159], ANSYS [143], and SYSWELD [54, 153] have been suggested to model yield strength and ultimate tensile strength of laser-welded joints. Although different studies have proposed numerical modeling for yield stress of the LBW process, it is reported that yield strength is related to grains size [165] with Hall–Petch relations according to follows:

$$\sigma_y = \sigma_0 + k\lambda^{-0.5} \tag{9}$$

where σ_y is the yield strength, and σ_0 and k are LBW process coefficients. It is also investigated that yield stress can be approximated to a linear relationship with Vickers hardness (HV) as follows [32, 166–168].
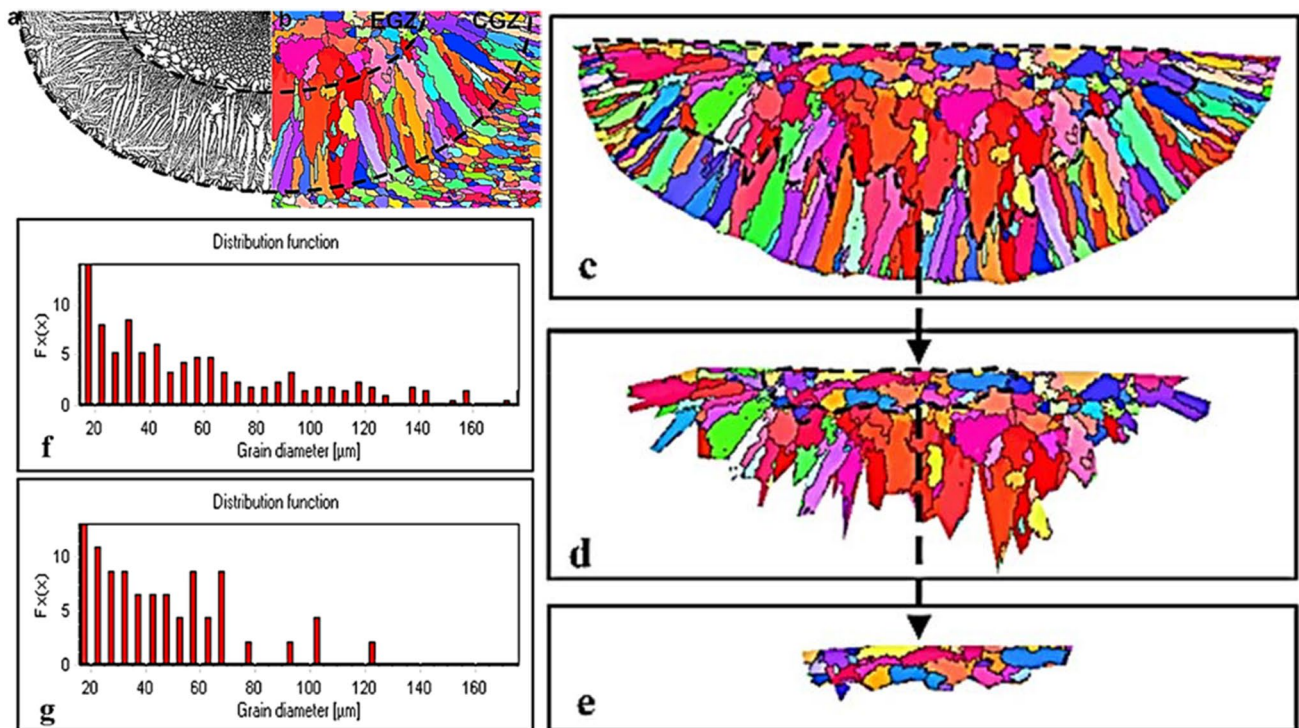

Fig. 28 CET modeling. Comparison of FZ microstructure between simulation (a) and experimental (b) results. (c) Microstructure of the fusion zone. (d) Microstructure of the equiaxed grain zone. (e) Micro-structure at the center of the equiaxed grain zone. (f) Grain size distribution of the equiaxed grain zone. (g) Grain size distribution at the center of the equiaxed grain zone [158]

Table 10 Summary of presented studies based on weld morphology and types of modeling and error

Row	Year	Material	CR_{Max} (K/s)	Thickness (mm)	Types of modeling based on			Formula	Max		Ref
					Monitoring	Approach	Method		GS (μm)	Error	
1	2011	Al-Cu	3300	NR	Off	Num	PF-CA	NR	6.25	25	[155]
2	2017	Al Cu 2024	NR	2	Off	Num	PF	NR	10.8	97.8	[156]
3	2017	Ti-6Al-4 V	410	1	Off	Num	ABAQUS	$d = 54.82 + 1.86 \times E_l$**	1000	1.1	[159]
4	2018	Al Cu 2024	NR	2	Off	Num	PF	NR	8.3	52.01	[157]
5	2021	Al4%Cu alloy 2A12	NR	4	Off	Num	PF	-	10	NR	[158]
6	2022	SS 316 NL	6900	5.5	Off	Num	ANSYS	$SDAS = 25\ CR^{-0.28}$	NR	NR	[97]

**E_l = laser power/laser scanning speed

$$\sigma_Y = c.HV + d \tag{10}$$

where c and d are LBW process coefficients.

Comparing the presented strength modeling of the LBW process in Table 11, it is concluded that the online-based model did not consider in previous studies, and most of the studies are offline and post-process. This leads to the error of 0.9 to 60%, which is a high broadband range, and affects the reliability and accuracy of LBWPM. Another deduction is that the presented models are restricted to particular materials and thicknesses since different materials, including steel, titanium alloy, Al alloy, and polymer with thicknesses of 1–10 mm, are considered in the models. In addition, comparing post-process, regression-based approach, a different formula is presented for an experimental condition such as thickness and types of material (see studies [32, 34, 127, 143, 159, 160]). This indicates that the post-process, regression-based approach is restricted to processing parameters. Thus, if the process parameters change, the previous parameters are not valid for the model, and it is necessary to conduct additional novel based on the new processing parameters.

5.2 Hardness

The hardness is defined as the material's toughness and can be determined by other mechanical characteristics such as tensile strength. Brittleness can be explained as the breaking of the material even at small forces exerted at a particular angle or plane. The experimental analysis proved that brittleness increased with the increase of hardness with a high correlation coefficient [169, 170], especially in the LBW process with the formation of intermetallic compound or IMCs [171]. Thus, the modeling of hardness characteristics of the LBW process is related to weld joint performance directly (brittleness, which leads to fracture and tensile strength).

Considering the critical role of hardness on the performance of weld joints, the summary of hardness models based on monitoring, approach, and methods is provided in Table 11. The presented hardness models are post-process and offline regarding stage and then regression and numerical in terms of methods. ANOVA as a regression-based model and numerical methods, including SYSWELD software (Mansur, de Figueiredo [54], ANSYS software [143], CFD-FEM [154], and FEM [32], have been studied to conduct models of the hardness of laser-welded joints.

A comparison of actual microstructure and hardness values with temperature profile and estimation of martensite fraction provided by numerical simulation is presented by Mansur et al., as shown in part A of Fig. 30 (Mansur, de Figueiredo [54]. After obtaining excellent agreement of FEM-based model with actual macrographic images and microhardness profile, the model indicates that the hardness is around 60% higher at the fusion zone than at base metal. The maximum hardness was detected at supercritical HAZ due to its highly refined microstructure in Dual Phase 600 material with a thickness of 1.6 mm.

The hardness comparison of the experimental and simulation for Vickers hardness for the laser-welded AH36 steel with thickness 6 mm with offline CFD-FEM-based model is shown in part B of Fig. 30 [154]. The fourth-order polynomial function of martensite fraction (F_m) was conducted for hardness calculation as shown in Table 12, where α is a fitting coefficient, which indicates a similar tendency of model and experimental results. The reduction of the hardness model in the fusion zone region is because of the dendrite structure from the melting of the workpiece. It should be noted that the hardness at HAZ was not considered in the study because its hardening mechanism was not modeled.

The hardness of the St-Al weld metal as a nonlinear function of aluminum concentration is modeled with a numerical approach and shown in part C of Fig. 30 [143], which exhibits the effect of Al concentration on weld hardness. Mixing of steel and aluminum within the weld pool during the keyhole LBW process results in a complex microstructure, which has been considered in the process of overlapping laser-welded austenitic stainless steel 304–6082-T6

Table 11 Summary of presented studies based on weld strength and types of modeling and error

Row	Year	Material	Thickness (mm)	Types of modeling based on			Formula	Max Strength (MPa)		Error (%)	Ref
				Monitoring	Approach	Method		UTS	YS		
1	2008	SS 304	3	Post	Reg	RSM	$TS = -4433.90+9102.06\times P-19.9\times S-511.93\times F+13.86\times PS+565.94\times PF-4.32\times S F-3954.102\times P^2$	692	NR	6.98	[160]
2	2008	AA5182	1.4	Post	ML	NN-GA	NR	284.9	NR	0.9	[163]
3	2017	Ti-6Al-4 V	1	Off	Num	ABAQUS	$UTS=90.4+68.7\times d^{-1/2\dagger\dagger}$ $YS=797.1+56.7d^{-1/2}$	915 -	- 839.5	60 54	[159]
4	2017	NR	NR	Post	Reg ML	SVR ANN	NR	60	NR	2 2	[115]
5	2021	Al-Li	2.5–4.5	Post	Reg	XGBoost	NR	293.5	NR	0.8	[33]
6	2021	DP 600 Steel	1.6	Off	Num	SYSWELD	NR	636	373	NR	[54]
7	2021	SS A387	10	Off	Num	SYSWELD	NR	556	NR	5.5	[153]
8	2021	301L-MT	8	Post	Reg	RSM	$TS=743.07-25.99\times A+117.11\times B-67.7\times C-12.72\times AB-32.54\times AC+17.83\times BC-18.34\times A^2-79.54\times B^2-35.9C^{2\ddagger\ddagger}$	777.326	NR	11.04	[161]
9	2021	SS 304-AA6082T6	1.5	Off	Num	ANSYS	Yield strength$=3781\times \exp(-0.05654\times Al)-3773\times \exp(-0.1137\times Al)$ Yield strength$=2.2\times$ Hardness -232	1200	NR	38.7	[143]
10	2021	SS301L-MT	8	Post	Reg	RSM	Tensile strength$=743-25.99A+117.11B-67.7C-12.72AB-32.54AC+17.84BC-18.34 A^2-79.54B^2-35.9C^2$	777.326	NR	11.04	[34]
11	2022	Al 2024T4-Al2024O	2	Off	Num	FEM	$\sigma_Y=-0.0543465\,HV+216.37314^{\S\S}$	450	344	5	[32]
12	2022	SS 301	NR	Post	ML	ANN	NR	NA	3.1	5	[164]
13	2022	Al 6061	2	Post	Reg	Kriging, RSM, RBF	NR	230	NA	9.93	[162]
14	2022	iPP	2	Post/Off	Reg/Num	ANOVA/COMSOL	$\sigma_{0.5\%\,CB}=10.78-0.01P-0.006919S+0.000959P^2$	9	NA	10.52	[127]

†† where d is average width of prior-β grains

‡‡ A is welding speed, **B is** laser power, C is wire feed rate, AC is the parameter interaction, **and** B^2 and C^2 are the second order effect

§§ c and d are fitting parameters and σ_Y is the yield stress
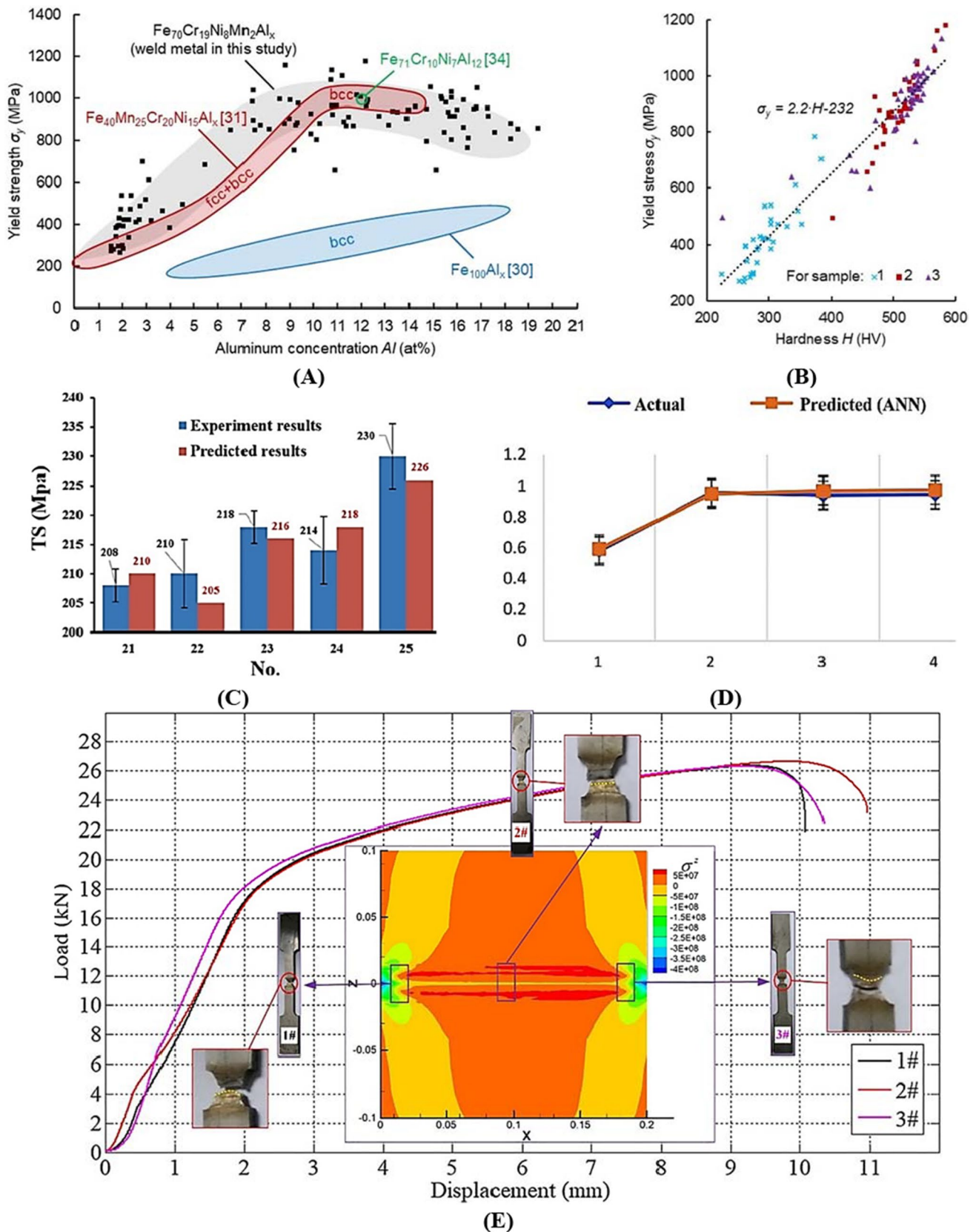
Fig. 29 The yield strength modeling of LBW process. **A** The yield strength versus Al concentration. **B** The yield strength versus hardness of St-Al weld metals [143]. **C** Comparison of experimental and predicted tensile strength [162]. **D** Comparison of experimental and predicted tensile strength via ANN [164]. **E** The curves of tensile strength for samples [142]

aluminum alloy with a thickness of 1.5 mm. This model revealed that the St-Al weld metal exhibits a gradual increase in hardness with a rise in Al concentration from 0 to 9%.

The hardness of the LBW process was analyzed for aluminum alloy 2024-T4 and Al 2024-O with a thickness of 2 mm with offline thermal elastic–plastic finite element model, as shown in part D of Fig. 30 [32]. Although different studies have proposed numerical modeling for the hardness of the LBW process, some of which are provided in Fig. 30 and Table 12, it is reported that Vickers hardness (HV) can be approximated to a linear relationship with residual stress as follows [32, 172–176]:

$$HV = k.\tilde{\sigma} + b \qquad (11)$$

Considering Table 12, except for study [122], most of the presented hardness models for the LBW process are offline and numerical based with the error of 5 to 38.70%. Although the numerical models are conducted for different materials, including types of steel, Al alloy, and Ti alloy with various thicknesses of 1.5 to 6 mm, further studies for polymer material with online and exact methods are needed. Hence, a closed-packed formula was provided in studies based on residual stress [32], Al compositions [143], and martensite fraction [154], which indicates the effect of material composition and residual stress on weld joint hardness. Besides, the interaction of these parameters and the effect of the rest of the material composition, phase transformation, solidification modes, and other mechanical, metallurgical, and even geometrical characteristics on weld hardness remained and can be considered in future models.

5.3 Residual stress

In general, residual stresses are divided into microscopic and macroscopic [177]. The origin of these stresses can be classified into three main sets mechanical, thermal, and metallurgical [178]. While mechanical and thermal residual stresses are macroscopic residual stresses, metallurgical residual stresses are often microscopic kind. The creation and distribution of microscopic residual stresses within the body are influenced by the processing of raw materials [179]; on the other hand, macroscopic residual stresses are caused by the mechanical behavior of various parts [180]. The most important factors, which bring about the weld residual stresses, are temperature deforming, degrees of temperature inhibition, mechanical constraints, and local and non-uniform heating factors [181].

In the early 1970s, Ueda and Hibbit et al. [182, 183] proposed the thermoplastic–plastic finite element analysis (FEA) for simulating the welding temperature field, residual stress, and deformation. Nowadays, many studies consider finite element analyses to simulate the welding process to study the welding residual stress distribution and deformation of welded joints [184]. Although different studies have proposed numerical modeling for residual stress of the LBW process, some of which are provided in Fig. 31 and Table 13, it is reported that relations for residual stress are as follows [74, 185]:

$$\sigma = -\frac{E}{2(1+\nu)} cot\theta_0 \frac{\pi}{180} \frac{\partial(2\theta)}{\partial sin^2\psi} \qquad (12)$$

where σ is the calculated residual stress. E, ν, and θ_0 are the elastic modulus, the Poisson ratio, and the diffraction angle in the unstressed state, respectively, which are determined by the physical properties of the material. $\partial(2\theta)/\partial sin^2\psi$ reflects the variation of lattice strain in different ψ angular directions. Although for low-carbon steel, because solid-state phase transformation has an insignificant influence on the residual stress welding [186], in the study by Sun et al. [70], the phase changes were not taken into account in the model. It is also mentioned that the creep behavior was neglected because the period with high temperature during the entire thermal cycle was very short. Hence, the total strain increments decomposed into three components, including elastic strain (ε^e), plastic strain (ε^p), and thermal strain (ε^{th}) as follows:

$$\left\{ d\varepsilon^{total} \right\} = \{d\varepsilon^e\} + \{d\varepsilon^p\} + \left\{ d\varepsilon^{th} \right\} \qquad (13)$$

$$\varepsilon_x = \frac{\partial u}{\partial x} + \frac{1}{2}\left\{ \left(\frac{\partial u}{\partial x}\right)^2 + \left(\frac{\partial v}{\partial x}\right)^2 + \left(\frac{\partial w}{\partial x}\right)^2 \right\} \qquad (14)$$

$$\varepsilon_y = \frac{\partial v}{\partial y} + \frac{1}{2}\left\{ \left(\frac{\partial u}{\partial y}\right)^2 \left(\frac{\partial v}{\partial y}\right)^2 \left(\frac{\partial w}{\partial y}\right)^2 \right\} \qquad (15)$$

$$\varepsilon_z = \frac{\partial w}{\partial z} + \frac{1}{2}\left\{ \left(\frac{\partial u}{\partial z}\right)^2 \left(\frac{\partial v}{\partial z}\right)^2 \left(\frac{\partial w}{\partial z}\right)^2 \right\} \qquad (16)$$

$$\gamma_{xy} = \frac{\partial u}{\partial y} + \frac{\partial v}{\partial x} + \left\{ \left(\frac{\partial u}{\partial x}\right)\left(\frac{\partial u}{\partial y}\right) + \left(\frac{\partial v}{\partial x}\right)\left(\frac{\partial v}{\partial y}\right) + \left(\frac{\partial w}{\partial x}\right)\left(\frac{\partial w}{\partial y}\right) \right\} \qquad (17)$$

$$\gamma_{yz} = \frac{\partial v}{\partial z} + \frac{\partial w}{\partial y} + \left\{ \left(\frac{\partial u}{\partial y}\right)\left(\frac{\partial u}{\partial z}\right) + \left(\frac{\partial v}{\partial y}\right)\left(\frac{\partial v}{\partial z}\right) + \left(\frac{\partial w}{\partial y}\right)\left(\frac{\partial w}{\partial z}\right) \right\} \qquad (18)$$

$$\gamma_{yz} = \frac{\partial u}{\partial z} + \frac{\partial w}{\partial x} + \left\{ \left(\frac{\partial u}{\partial z}\right)\left(\frac{\partial u}{\partial x}\right) + \left(\frac{\partial v}{\partial z}\right)\left(\frac{\partial v}{\partial x}\right) + \left(\frac{\partial w}{\partial z}\right)\left(\frac{\partial w}{\partial x}\right) \right\} \qquad (19)$$

where ε_x, ε_y, and ε_z are Green–Lagrange strain in the x, y, and z directions. The shear strains on the x–y, y–z, and z–x planes are considered as γ_{xy}, γ_{yz}, and γ_{zx}, respectively. u, v,

Fig. 30 Hardness modeling of LBW process. **A** Comparison of actual microstructure and hardness values with temperature profile and estimation of martensite fraction provided by numerical analysis (Mansur, de Figueiredo [54]). **B** Comparison of the experimental and simulation for Vickers hardness [154]. **C** Hardness of the St-Al weld metal as a function of the aluminum concentration [143]. **D** Hardness map of the entire weld joint for (top) Al 2024-T4 and (bottom) Al 2024-O [32]
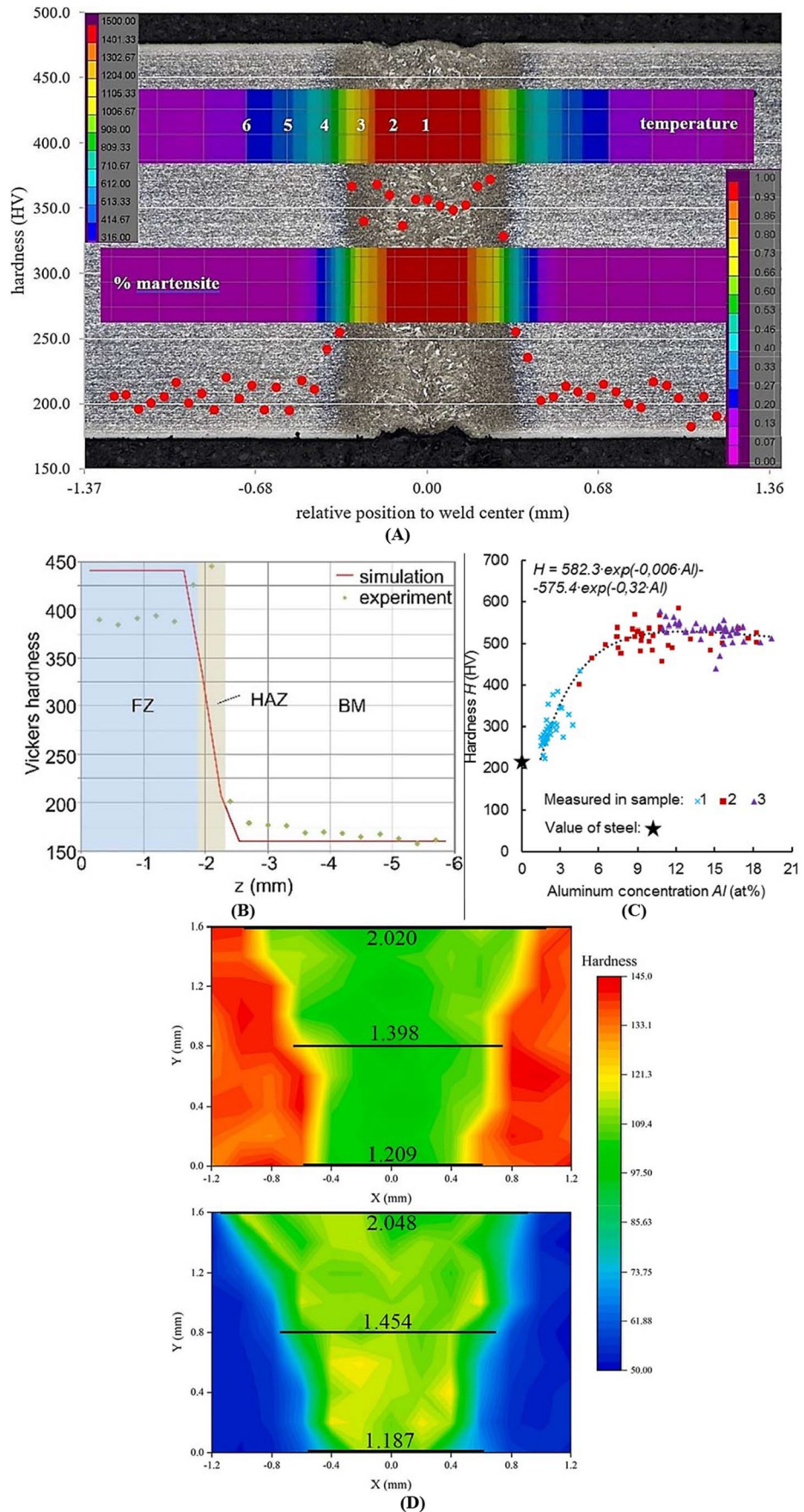
Table 12 Summary of presented studies based on weld hardness and types of modeling and error

Row	Year	Material	Thickness (mm)	Types of modeling based on			Formula	Max Hardness (HV)	Error (%)	Ref
				Monitoring	Approach	Method				
1	2021	Al 2024T4-Al2024O	2	Off	Num	FEM	$HV = -0.0195\sigma + 117.22$	145	5	[32]
2	2021	DP 600 Steel	1.6	Off	Num	SYSWELD	NR	500	NR	[54]
3	2021	Ti-Grade 5	2	Post	Reg	ANOVA	NR	329	5.00	[122]
4	2021	SS 304-AA6082 T6	1.5	Off	Num	ANSYS	$Hardness = 582.3 \times \exp(-0.006 \times Al) - 574.4 \times \exp(-0.32 \times Al)$	600	38.70	[143]
5	2021	AH36 steel	6	Off	Num	CFD-FEM	$Hardness = \sum_{i=0}^{4}\left(\alpha_i F_m^{\,i}\right)$	440	22.22	[154]

***σ is the residual stress

and w express the displacement in x, y, and z directions, respectively. In Eqs. (12)–(19), the first-order terms indicate linear behavior, and the second-order terms provide nonlinear response such as buckling [70]. The results revealed no difference between transverse residual distribution on the top and bottom surface, and the maximum absolute value is approximately 50 MPa.

The thermal-plastic analysis was considered to model the transverse and longitudinal residual stress of 316L stainless steel multilayer in another study [74]. The experimental (based on X-ray diffraction) measured and model results of transverse and longitudinal residual stress along the test, transverse residual stress contour extracted from the model, and residual stress along the thickness directions are illustrated in parts A, B, and C of Fig. 11, respectively. The residual stress results sharply changed at the interlayer position, which expresses that the grain size and orientation in the re-melting zone changed directly. The considered models of studies [74, 139, 187] were the same and based on the transient thermal–elastic–plastic finite element theory and inherent strain analysis (ISA) with ANSYS software with different heat sources.

Thermo-elastoplastic models with isotropic and kinematic hardening were applied to model the residual stress of the LBW process [126]. Although these models perform in the same way for the first traction, once the material is plastically deformed, the isotropic hardening model will expand the elasticity domain, which leads to an increase the yield strength. In contrast, the kinematic hardening model will displace the center of the elastic domain, which is always performed to represent the Bauschinger effect and is consequently recommended for cyclic loading. The comparison between the experimental and numerical models of transversal and longitudinal with both hardening modes for laser scanning speeds of 600, 1600, and 2600 mm/min is shown in Fig. 31. Comparing parts A to F of Fig. 31, a significant effect of hardening patterns is noted in the HAZ, where the material has been plasticized and experienced cyclic loading. Hence, by increasing laser scanning speed, the maximum residual stresses increase, and a rise of 100 MPa is provided between the longitudinal residual stresses for speeds of 600 mm/min and 2600 mm/min (Fig. 32).

Comparing the presented residual weld stress, provided in Table 13, it can be deduced that except for study [135] (which is post-process regression based), most of the modeling is based on offline numerical based on the FEM approach with an error range of 2.6 to 23.4%. Although the presented models are not restricted to the materials, different types of steel and Al alloy with thicknesses of 1.33 to 20 mm have been considered. It should be noted that firstly, a closed-packed formula was not presented in the literature; instead, a secondary gap of the offline dynamic model, which could predict the residual stress, is detected.
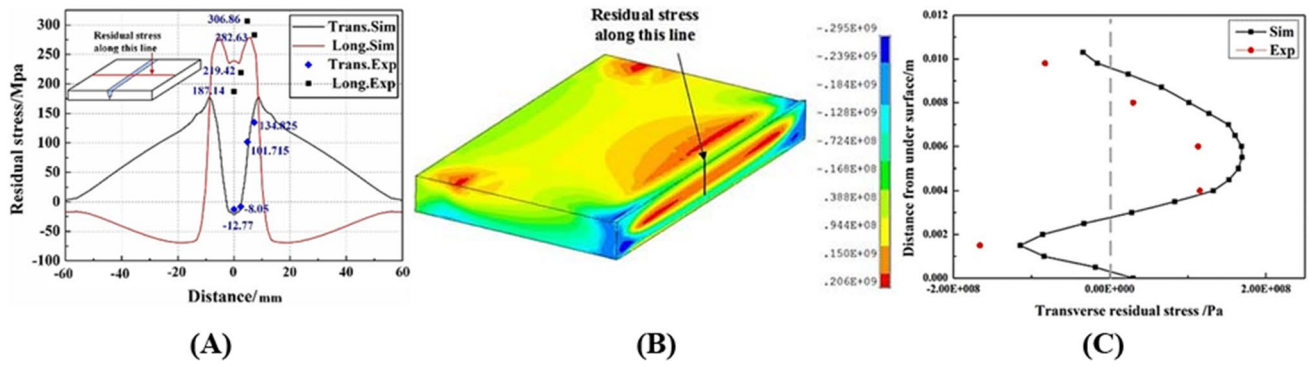
Fig. 31 Residual stress modeling of LBW process. **A** Comparison analysis between simulation and experimental. **B** Transverse residual stress contour. **C** Residual stress along the thickness direction [74]

Table 13 Summary of presented studies based on weld residual stress and types of modeling and error

Row	Year	Material	Thickness	Types of modeling based on			Formula	Max		Ref
				Monitoring	Approach	Method		Stress (MPa)	Error (%)	
1	2014	Q235	2.3	Off	Num	FEM	NA	300	NR	[70]
2	2016	Q235 Steel	6	Off	Num	FEM	NA	200	2.6	[72]
3	2016	SS 316L	5	Off	Num	FEM	NA	452.3	5.95	[139]
4	2017	SS 316L	5	Off	Num	ANSYS	NA	396	11.0	[187]
5	2017	316L	3.8	Off	Num	ANSYS	NA	720	23.4	[140]
6	2017	SS301L	1.33	Off	Num	ABAQUS	NA	550	NR	[141]
7	2018	Steel EH36	4	Off	Num	ANSYS	NA	650	15.6	[117]
8	2019	SS316L	5	Off	Num	ANSYS	NA	400	5.84	[142]
9	2019	SS316L	10	Off	Num	ANSYS	NA	190	NR	[74]
10	2021	HT780 steel	20	Off	Num	FEM	NA	500	NR	[77]
11	2021	SS 316LN	5.6	Off	Num	SYSWELD	NA	400	NR	[144]
12	2021	DP 600	1.6	Off	Num	SYSWELD	NA	600	NR	[54]
13	2021	AH36 steel	6	Off	Num	CFD-FEM	NA	600	75	[154]
14	2022	SS301L	0.6	Off	Num	FE	-	690.08	9.4	[124]
15	2022	Al 2024T4-Al2024O	2	Off	Num	FEM	Von Mises	300	5	[32]
16	2022	SS316L	10	Off	Num	SYSWELD	NA	452	5	[126]
17	2023	SS316L	5	Off	Num	ANSYS	NA	214	10	[188]
18	2023	Steel 710	6	Off/Post	Num/Reg	FEM/RFA	RS	936.47	3.1	[135]

$^{†††}635.74 + 121.00A + 62.96B - 27.73C - 24.69D + 9.11AB - 340.31AC - 12.36AD + 115.19BC - 68.54BD + 83.16CD + 4.97A^2 + 28.11B^2 + 33.13C^2 - 37.42D^2$

6 Gap of studies and future trends

To access new development, such as Industry 4.0. revolution, the laser beam welding (LBW) process is a perfect candidate [189]. Since many progresses are being made in the technology coming from LBW manufacturers, most sectors have been focused on it. One of the most appealing applications is automotive, particularly e-mobility, which

is expected to expand at a compound annual growth factor (CAGR) of 49.38% from 2020 to 2025 [190]. Electric vehicle (EV) welding applications are the main drivers in copper and aluminum laser welding growth in different parts, as shown in Fig. 33.

In the previous sections, the modeling of geometrical, metallurgical, and mechanical characteristics of the LBW process, which is one of the main challenges of the LBW

process, was presented, and some of the case studies were discussed. Studies tend to agree broadly on impacts for LBWCM to predict the weld characteristics accurately. The graphical presentation of LBWCM based on a number of publications and the year of them, divided into (1) 1990–2000, (2) 2001–2010, and (3) 2011–2023, is illustrated in Fig. 34.

As can be seen in Fig. 34, most LBW models were presented in 2011–2023 with 86.11% of total publications. This indicates that the most growth of LBWCM is for the last decades; thus, it is nowadays trend. Considering the CAGR of 49.38% of EVs from 2020 to 2025, the rise of 86.11% of LBWCM from 2011 to 2023 is perceptible by comparing Fig. 33 with Fig. 34. Although metallurgical and mechanical (except strength) were not considered in 1990–2010, a noticeable number of studies have been conducted on this area in 2011–2023, which also expresses the need of it. Further details of the share of metallurgical, mechanical, and
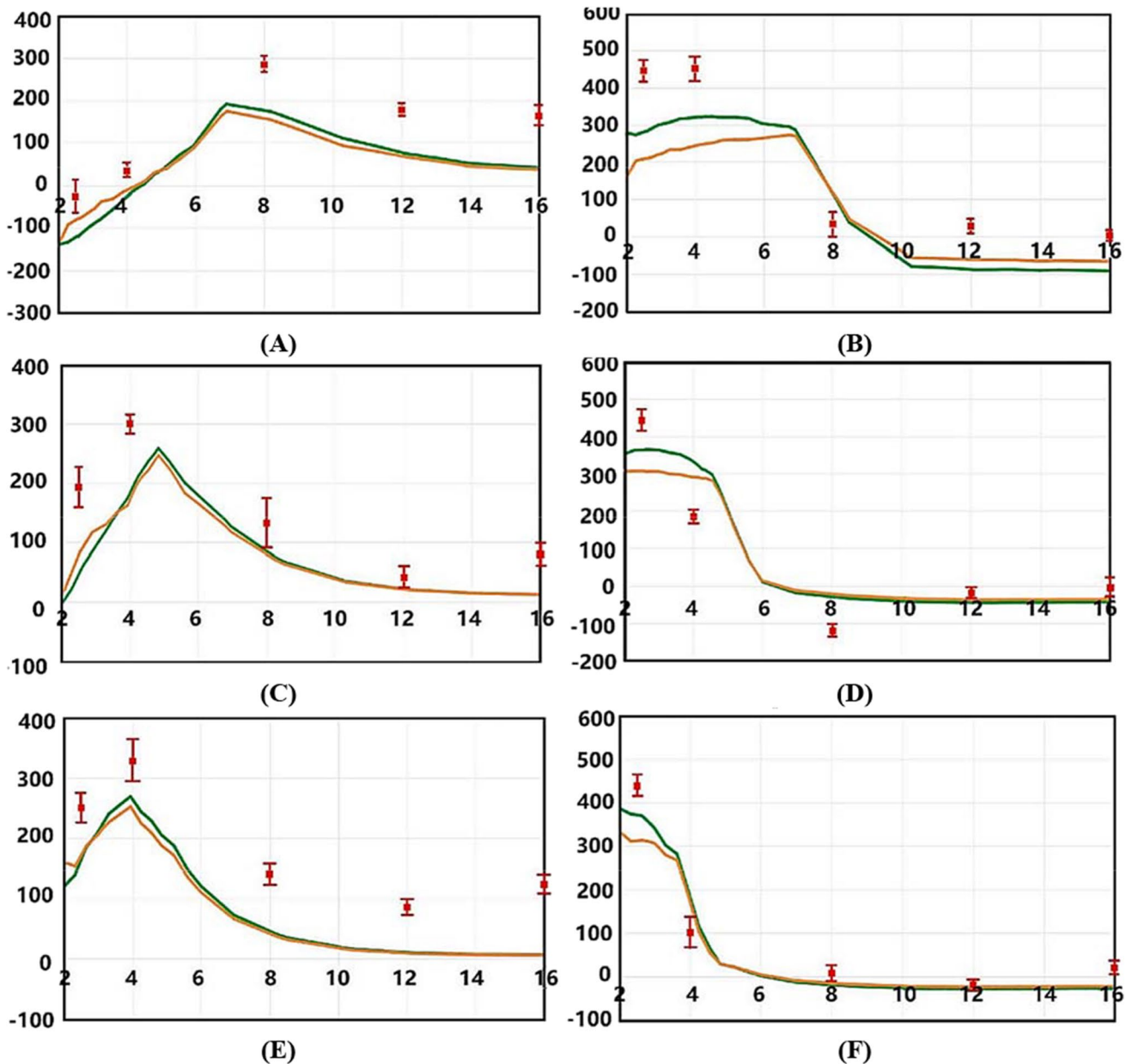
Fig. 32 The comparisons of transversal and longitudinal residual stress. **A** Transversal with a laser scanning speed of 600 mm/min. **B** Longitudinal with a laser scanning speed of 600 mm/min. **C** Transversal with a laser scanning speed of 1600 mm/min. **D** Longitudinal with a laser scanning speed of 1600. **E** Transversal with a laser scanning speed of 1600 mm/min. **F** Longitudinal with a laser scanning speed of 2600 mm/min with experimental measurement (red square), isotropic hardening model (green line), and kinematic hardening (orange line) [126]
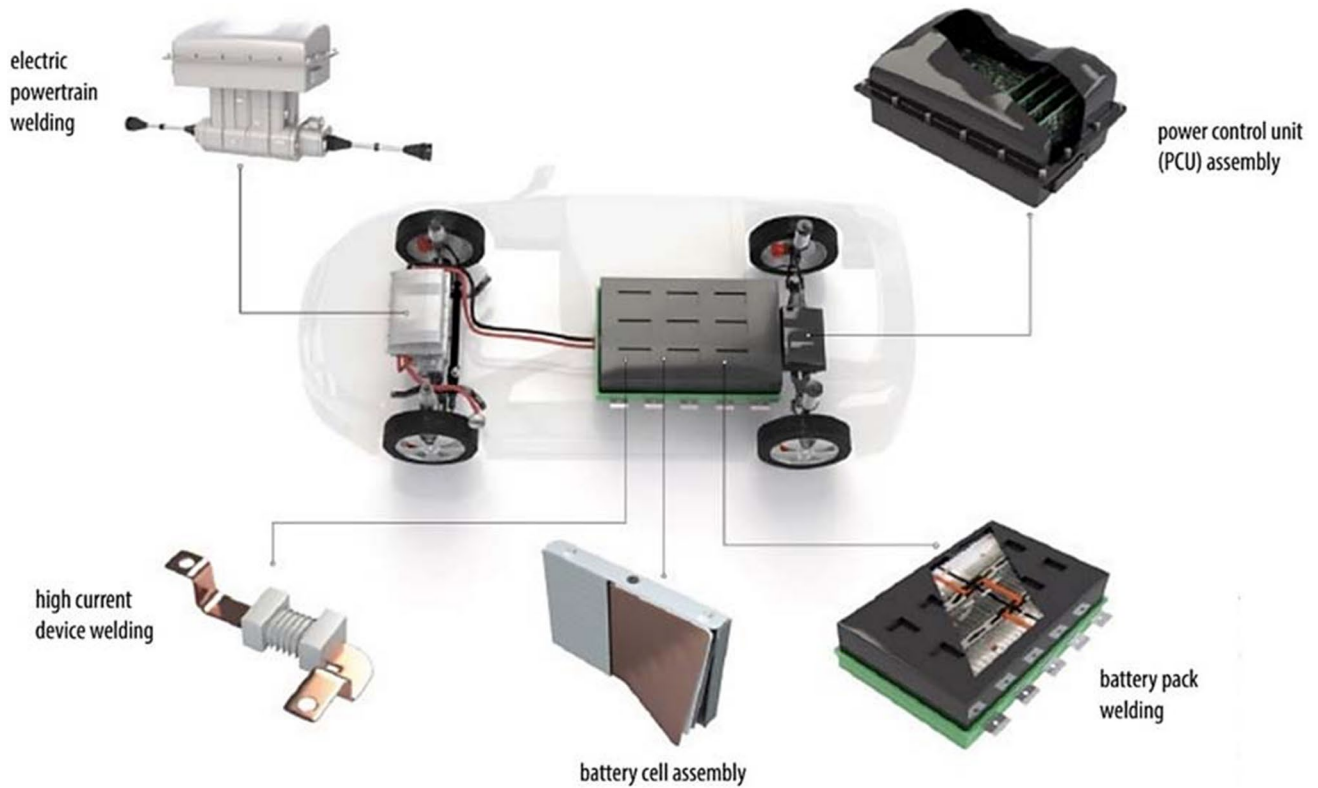
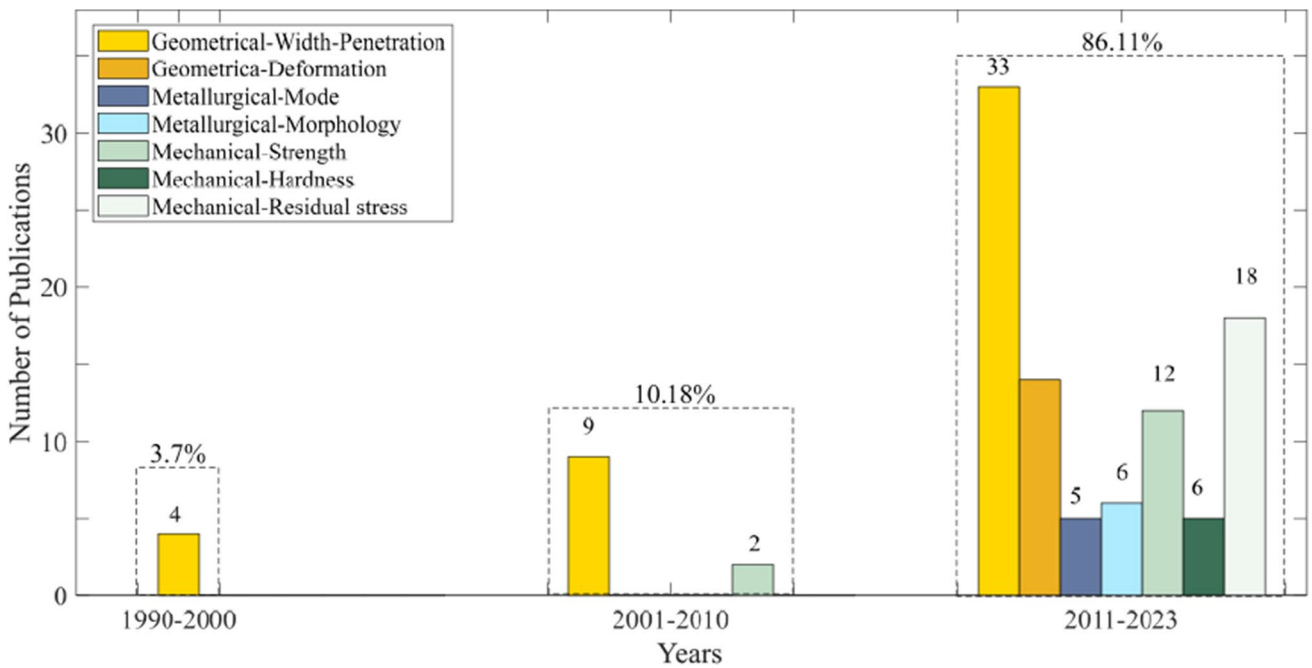**Fig. 33** Presence of the LBW process in various parts of manufacturing of EV [189]

Fig. 34 Graphical presentation of published LBW process modeling versus years, including geometrical characteristics (weld width-penetration and deformation), metallurgical characteristics (solidification mode and morphology), and mechanical characteristics (strength, hardness, and residual stress)
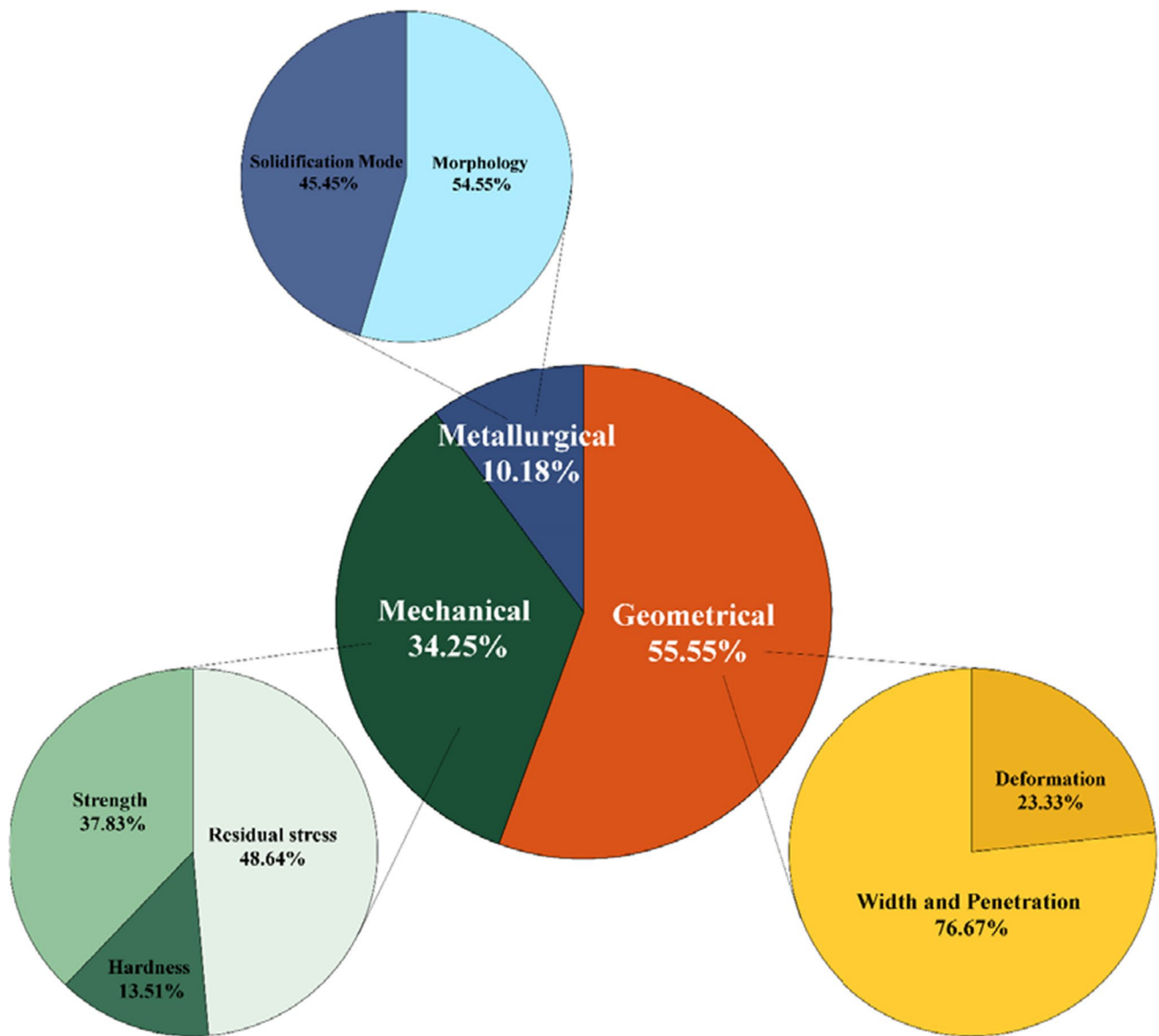
Fig. 35 Graphical presentation of share of metallurgical, mechanical, and geometrical characteristic modeling in total publications for LBW process

geometrical characteristics of LBW modeling in total publications are provided in Fig. 35.

Figure 35 reveals different deductions about LBWCM. Firstly, the geometrical characteristics have the most shares with the share of 55.55%, while metallurgical models are the least (10.18%), and mechanical model contributes 34.25% share of models. Since the geometry, which is the appearance of the weld joint, can be measured with non-destructive methods with no high technology tools, most of the studies have focused on modeling this. Hence, there is no complex process to model weld width and penetration, since they are the depth and width of the melt pool, which solidifies after the cooling process. On the other hand, to model and predict metallurgical

and mechanical weld characteristics, besides requirements of destructive high-tech tools, it is essential to have a deep perception of the physical phenomena of melt pool, such as five mechanisms absorption, heat conduction, vapor dynamic, melt dynamics, and phase transitions and complicated coupled non-linear equations such as continuity, momentum, energy, and mass fraction, which have been discussed in Sects. 2.3 and 2.4.

Secondly, although weld width and penetration have 76.67% of the share of geometrical characteristics models, as can be seen in Fig. 35, the deformation models has been increased noticeably in the last decades (orange bar of Fig. 34). Thirdly, in mechanical characteristic modeling, there is a considerable gap of study in hardness models
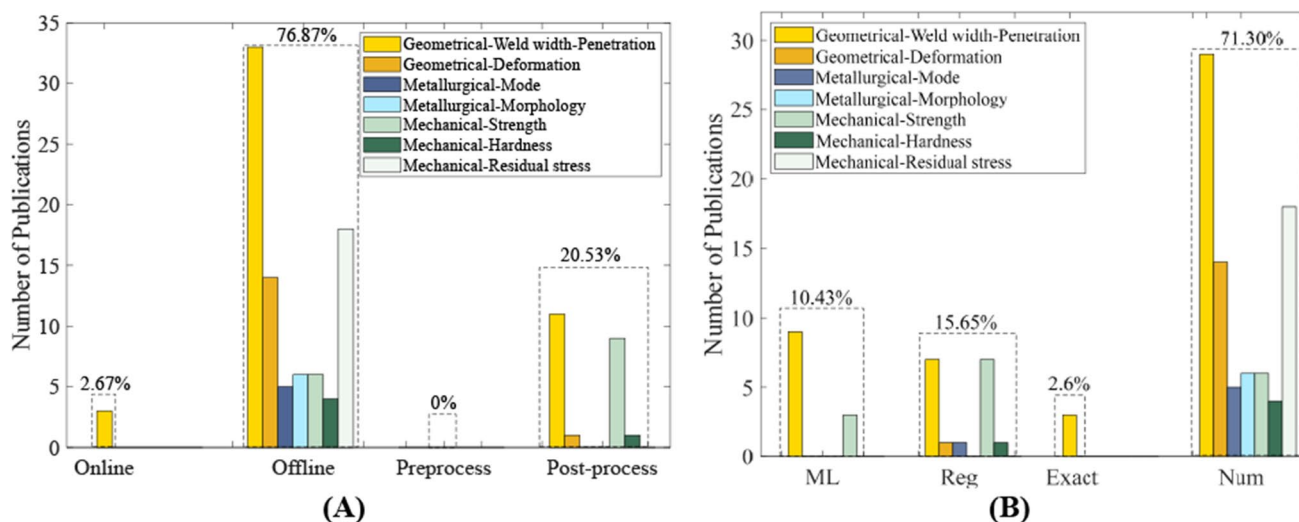
Fig. 36 Graphical presentation of geometrical, metallurgical, and mechanical characteristic modeling of LBW process based on **A** monitoring the process and **B** applying the approaches

since this characteristic has the most negligible share of mechanical models (13.51%). Metallurgical modeling, with the enormous concept of gap study, is divided into solidification modes and morphology models nearly equal. This indicates that there is still a long way to provide in-depth solidification and morphology models, which predict the metallurgical characteristics with high accuracy.

Besides characteristics, the LBWCM can be divided into monitoring and methods as discussed with details in Sects. 2.2 and 2.4, respectively. The LBW process presented models based on types of monitoring, including pre-process, in-process (offline and online), and post-process, which are illustrated in part A of Fig. 36. While there is no pre-process characteristics model, online in-process models have the most minor share of publications, 2.67%. Due to the high sensitivity of the LBW process, the repeatability of the process is questioned with the smallest change of the process parameters and the creation of instability. The instabilities during the LBW process caused by changes in environmental conditions can lead to changes in the melt pool conditions and weld characteristics. Although there are various reasons for the instability of the process, the most essential factor is applying the high energy density laser energy in a small area of the melt pool. Combining this with the presence of all four phases of material, including solid, liquid, gas, and plasma, in a small melt pool area, leads to extensive and tremendous requirements for online models for the LBW process. This makes the gap of studies for a model, which could predict the metallurgical characteristics of the laser beam welding process, crucial and inevitable.

The presented published geometrical, metallurgical, and mechanical characteristics models based on types of

approach, including empirical-based (such as machine learning (ML), regression (Reg)) and theoretical-based (exact, and numerical (Num)), are shown in part B of Fig. 36. Except for strength models, the rest of the characteristic models are mainly conducted based on numerical methods, with a 71.30% share of models. The exact approach, which can provide a deep perception of the process, is considered just for modeling weld width and penetration. This express is a noticeable gap of study in the applied exact theoretical-based approach to conducting the metallurgical and mechanical characteristics and deformation of the weld joints.

In conclusion, it can be deduced that although various models have been presented for different weld joint characteristics, including geometrical, mechanical, and metallurgical, there remains a gap in the study. Firstly, a comprehensive model, which could predict all the characteristics at the same time, is lacking; secondly, an online model (that considers the variable process instabilities) is required; and lastly, an exact-based model which provides the vision of physics of the process is needed.

7 Conclusions

Owing to numerous industrial applications, unique advantages, and complexity of its process, the laser beam welding process requires to be studied continuously and precisely to provide a model, which can be predicted. Perception of laser beam welding process modeling (LBWPM) leads to an increase in the performance of weld joints. In the current study, a comprehensive review of types of LBWPM, including characteristics (geometrical (weld width, penetration, and deformation), metallurgical (solidification mode, phase

transformation, and morphology), and mechanical (strength, hardness, and residual stress)), length scale, approach, and monitoring, was presented, and some of the case studies were analyzed. The gap of studies and future trends of LBWPM based on case studies revealed some noticeable deductions as follows:

- Considering studies from 1990, most of LBWPM are presented in laser decades (2011–2023), with 86.11% of entire publications. Although metallurgical and mechanical (except strength) were not considered in 1990–2010, a noticeable number of studies have been conducted on this area in 2011–2023, which also expresses the needs of it.
- It is revealed that the geometrical characteristics have the most shares (55.55%), while metallurgical models are the least (10.18%), and mechanical model contributes 34.25% share of presented models. Although weld width and penetration have 76.67% of the share of geometrical characteristics models, the deformation models have increased noticeably in the last decades. In mechanical characteristic modeling, there is a considerable gap of study in hardness models since this characteristic has the most minor share of mechanical models (13.51%). Metallurgical models, with an enormous concept of gap study, are divided into solidification modes and morphology models nearly equal. This indicates that there is still a long way to provide in depth in this area.
- While there is no pre-process characteristics model for the LBW process, online in-process models have the most negligible share of publications, 2.67%. Due to the high sensitivity and instability of the LBW process, the gap of studies for a model, which could predict the metallurgical characteristics of the laser beam welding process, is crucial and inevitable.
- Except for strength models, the rest of the characteristic's models are mainly conducted based on numerical methods, with a 71.30% share of models. The exact approach, which can provide an in-depth perception of the process, is considered just for modeling weld width and penetration. This expresses a noticeable gap of study in the applied exact theoretical-based approach to conducting the metallurgical and mechanical characteristics and deformation of the weld joints.
- In conclusion, it can be deduced that although various models have been presented for different weld joint characteristics, including geometrical, mechanical, and metallurgical, the following are needed: firstly, a comprehensive model, which could predict all the characteristics at the same time; secondly, an online model (that considers the variable process instabilities); and lastly, an exact-based model which provides the vision of physics of the process.

Declarations

References

1. Jokinen T, Karhu M, Kujanpää V (2003) Welding of thick austenitic stainless steel using Nd: yttrium–aluminum–garnet laser with filler wire and hybrid process. J Laser Appl 15(4):220–224
2. Cao X-J, Jahazi M, Immarigeon J, Wallace W (2006) A review of laser welding techniques for magnesium alloys. J Mater Process Technol 171(2):188–204
3. Blackburn J (2012) Laser welding of metals for aerospace and other applications. Elsevier, Welding and joining of aerospace materials, pp 75–108
4. Hong K-M, Shin YC (2017) Prospects of laser welding technology in the automotive industry: a review. J Mater Process Technol 245:46–69
5. Subashini L, Prabhakar KP, Ghosh S, Padmanabham G (2020) Comparison of laser-MIG hybrid and autogenous laser welding of M250 maraging steel thick sections—understanding the role of filler wire addition. Int J Adv Manuf Technol 107:1581–1594
6. Wang J, Fu X, Zhang L, Zhang Z, Liu J, Chen S (2021) A short review on laser welding/brazing of aluminum alloy to steel. Int J Adv Manuf Technol 112:2399–2411
7. Sadeghian A, Iqbal N (2022) A review on dissimilar laser welding of steel-copper, steel-aluminum, aluminum-copper, and steel-nickel for electric vehicle battery manufacturing. Opt Laser Technol 146:107595
8. Myhr O, Grong Ø, Fjær H, Marioara C (2004) Modelling of the microstructure and strength evolution in Al–Mg–Si alloys during multistage thermal processing. Acta Mater 52(17):4997–5008
9. Ninh NT, Wahab MA (1995) The effect of residual stresses and weld geometry on the improvement of fatigue life. J Mater Process Technol 48(1–4):581–8
10. Sun X, Stephens EV, Khaleel MA (2008) Effects of fusion zone size and failure mode on peak load and energy absorption of advanced high strength steel spot welds under lap shear loading conditions. Eng Fail Anal 15(4):356–367
11. da Silva BL, Ferreira J, Araújo J (2012) Influence of notch geometry on the estimation of the stress intensity factor threshold

by considering the theory of critical distances. Int J Fatigue 42:258–270

12. Konjatić P, Kozak D, Gubeljak N (2012) The influence of the weld width on fracture behaviour of the heterogeneous welded joint. Trans Tech Publ, Key Engineering Materials

13. Morris Jr J (2001) The influence of grain size on the mechanical properties of steel

14. Zhang X, Mi G, Wang C (2020) Microstructure and performance of hybrid laser-arc welded high-strength low alloy steel and austenitic stainless steel dissimilar joint. Opt Laser Technol 122:105878

15. Farrar R, Harrison P (1987) Acicular ferrite in carbon-manganese weld metals: an overview. J Mater Sci 22:3812–3820

16. Ohkita S, Horii Y (1995) Recent development in controlling the microstructure and properties of low alloy steel weld metals. ISIJ Int 35(10):1170–1182

17. Jin D, Hou C, Shen L (2021) Effect of welding residual stress on the performance of CFST tubular joints. J Constr Steel Res 184:106827

18. Zhang YH, Smith S, Wei L, Johnston C, Stacey A (2013). Measurement and modelling of residual stresses in offshore circumferential welds. Int Conf Offshore Mech Arct Eng, Am Soc Mech Eng

19. Talabi SI, Owolabi OB, Adebisi JA, Yahaya T (2014) Effect of welding variables on mechanical properties of low carbon steel welded joint. Adv Prod Eng Manag 9(4):181–186

20. Dowden J (2009) The theory of laser materials processing. Heat Mass Trans Modern Technol: 95–128

21. Yang J, Oliveira J, Li Y, Tan C, Gao C, Zhao Y, Yu Z (2022) Laser techniques for dissimilar joining of aluminum alloys to steels: a critical review. J Mater Process Technol 301:117443

22. Gonçalves LF, Duarte FM, Martins CI, Paiva MC (2021) Laser welding of thermoplastics: an overview on lasers, materials, processes and quality. Infrared Phys Technol 119:103931

23. Parimanik SR, Mahapatra TR, Mishra D (2023) A Systematic Literature Review on Laser Welding of NiTi SMA. Lasers Manuf Mater Proc 10(1):77–117

24. Junke JI, Jihao XU, Chenghu JI, SHENG L, Haolei RU, Hongbo XI (2023). Laser welding process and strength enhancement of carbon fiber reinforced thermoplastic composites and metals dissimilar joint: a review. Chinese J Aeronautics

25. Norouzian M, Elahi MA, Plapper P (2023). A review: suppression of the solidification cracks in the laser welding process by controlling the grain structure and chemical compositions. J Adv Join Proc: 100139

26. Kang S, Lee K, Kang M, Jang YH, Kim C (2023) Weld-penetration-depth estimation using deep learning models and multisensor signals in Al/Cu laser overlap welding. Opt Laser Technol 161:109179

27. Franco A, Romoli L, Musacchio A (2014) Modelling for predicting seam geometry in laser beam welding of stainless steel. Int J Therm Sci 79:194–205

28. Kozak J (2022) Prediction of weld deformations by numerical methods-review. Pol Marit Res 29(1):97–107

29. Hashemzadeh M, Garbatov Y, Soares CG (2022) Hybrid-laser welding-induced distortions and residual stresses analysis of large-scale stiffener panel. Ocean Eng 245:110411

30. Mohan A, Ceglarek D, Franciosa P, Auinger M (2023). Numerical study of beam oscillation and its effect on the solidification parameters and grain morphology in remote laser welding of high-strength aluminium alloys. Sci Technol Weldd Join: 1–10

31. Hargreaves J, Moore S, Yuan G, Liu D, Tipping H, Abbott R, Tufnail J, Dawson H, Martin TL (2023). Microstructural modelling and characterisation of laser-keyhole welded Eurofer 97. Materials & Design: 111614

32. Gao S, Geng S, Jiang P, Han C, Ren L (2022) Numerical study on the effect of residual stress on mechanical properties of laser welds of aluminum alloy 2024. Opt Laser Technol 146:107580

33. Zhang Z, Huang Y, Qin R, Ren W, Wen G (2021) XGBoost-based on-line prediction of seam tensile strength for Al-Li alloy in laser welding: experiment study and modelling. J Manuf Process 64:30–44

34. Chen L, Yang T, Zhuang Y, Chen W (2021) The multi-objective optimization modelling for properties of 301 stainless steel welding joints in ultra-narrow gap laser welding. Weld World 65(7):1333–1345

35. Frostevarg J (2018) Factors affecting weld root morphology in laser keyhole welding. Opt Lasers Eng 101:89–98

36. Nabavi SF, Farshidianfar MH, Farshidianfar A, Beidokhti B (2021). Physical-based methodology for prediction of weld bead characteristics in the laser edge welding process. Optik: 166917

37. Wei L, Dean D, Murakawa H (2005) Measurement of inherent deformations in typical weld joints using inverse analysis (Part2) Prediction of welding distortion of large structure. Trans JWRI 34(1):113–123

38. Villaret V, Deschaux-Beaume F, Bordreuil C, Fras G, Chovet C, Petit B, Faivre L (2013) Characterization of gas metal arc welding welds obtained with new high Cr–Mo ferritic stainless steel filler wires. Mater Des 51:474–483

39. Kou S (2003) Welding metallurgy. New Jersey, USA 431(446):223–225

40. Abioye T, Olugbade T, Ogedengbe T (2017) Welding of dissimilar metals using gas metal arc and laser welding techniques: a review. J Emerg Trends Eng Appl Sci 8(6):225–228

41. Jackson K (1971) Solidification. American Society for Metals: Metals Park, OH: 141

42. Inoue H, Koseki T, Okita S, Fuji M (1997) Solidification and transformation behaviour of austenitic stainless steel weld metals solidified as primary austenite: study of solidification and subsequent transformation of Cr-Ni stainless steel weld metals (1st Report). Weld Int 11(11):876–887

43. Farshidianfar MH (2017) Real-time closed-loop control of microstructure and geometry in laser materials processing. University of Waterloo, PhD

44. Saluja R, Moeed K (2012) The emphasis of phase transformations and alloying constituents on hot cracking susceptibility of type 304L and 316L stainless steel welds. Int J Eng Sci Technol 4(5):2206–2216

45. Suutala N (1983) Effect of solidification conditions on the solidification mode in austenitic stainless steels. Metall Trans A 14(1):191–197

46. Pujar M, Dayal R, Gill T, Malhotra S (2005) Evaluation of microstructure and electrochemical corrosion behavior of austenitic 316 stainless steel weld metals with varying chemical compositions. J Mater Eng Perform 14(3):327–342

47. Kotecki D, Siewert T (1992) WRC-1992 constitution diagram for stainless steel weld metals: a modification of the WRC-1988 diagram. Weld J 71(5):171–178

48. Zhang Z, Li B, Zhang W, Lu R, Wada S, Zhang Y (2020) Real-time penetration state monitoring using convolutional neural network for laser welding of tailor rolled blanks. J Manuf Syst 54:348–360

49. Singh SS, Praneeth RV, Sankalp VS, Sashank SS (2022). Welding, mechanical properties and microstructure of different grades of austenitic stainless steels: a review. Mater Today: Proc

50. Masubuchi K (2013) Analysis of welded structures: residual stresses, distortion, and their consequences. Elsevier

51. Sirohi S, Pandey SM, Tiwari V, Bhatt D, Fydrych D, Pandey C (2023) Impact of laser beam welding on mechanical behaviour of 2.25 Cr–1Mo (P22) steel. Int J Press Vessel Piping 201:104867

52. Naik AB, Reddy AC (2018) Optimization of tensile strength in TIG welding using the Taguchi method and analysis of variance (ANOVA). Therm Sci Eng Prog 8:327–339

53. Sokolov M, Salminen A, Kuznetsov M, Tsibulskiy I (2011) Laser welding and weld hardness analysis of thick section S355 structural steel. Mater Des 32(10):5127–5131

54. Mansur VM, de Figueiredo Mansur RA, de Carvalho SM, de Siqueira RHM, de Lima MSF (2021) Effect of laser welding on microstructure and mechanical behaviour of dual phase 600 steel sheets. Heliyon 7(12):e08601

55. Barsoum Z, Jonsson B (2011) Influence of weld quality on the fatigue strength in seam welds. Eng Fail Anal 18(3):971–979

56. Bachmann M, Artinov A, Meng X, Putra SN, Rethmeier M (2023). Challenges in dynamic heat source modeling in high-power laser beam welding. J Laser Appl 35(4).

57. Stache NC, Stollenwerk A, Gedicke J, Olowinsky A, Knepper A, Aach T (2009) Automatic calibration of a scanner-based laser welding system. J Laser Appl 21(1):10–15

58. Luo M, Shin YC (2015) Vision-based weld pool boundary extraction and width measurement during keyhole fiber laser welding. Opt Lasers Eng 64:59–70

59. Cai W, Wang J, Jiang P, Cao L, Mi G, Zhou Q (2020) Application of sensing techniques and artificial intelligence-based methods to laser welding real-time monitoring: a critical review of recent literature. J Manuf Syst 57:1–18

60. Kaierle S, Ungers M, Franz C, Mann S, Abels P (2010) Understanding the laser process: new approaches for process monitoring in laser materials processing. Wiley Online Library 7:49–52

61. Kawahito Y, Ohnishi T, Katayama S (2009) In-process monitoring and feedback control for stable production of full-penetration weld in continuous wave fibre laser welding. J Phys D Appl Phys 42(8):085501

62. You D, Gao X, Katayama S (2014) WPD-PCA-based laser welding process monitoring and defects diagnosis by using FNN and SVM. IEEE Trans Industr Electron 62(1):628–636

63. Otto A, Schmidt M (2010) Towards a universal numerical simulation model for laser material processing. Phys Procedia 5:35–46

64. Geiger M, Leitz K-H, Koch H, Otto A (2009) A 3D transient model of keyhole and melt pool dynamics in laser beam welding applied to the joining of zinc coated sheets. Prod Eng Res Devel 3(2):127–136

65. Abderrazak K, Salem WB, Mhiri H, Lepalec G, Autric M (2008) Modelling of CO_2 laser welding of magnesium alloys. Opt Laser Technol 40(4):581–588

66. Francois MM, Sun A, King WE, Henson NJ, Tourret D, Bronkhorst CA, Carlson NN, Newman CK, Haut T, Bakosi J, Gibbs JW (2017) Modeling of additive manufacturing processes for metals: Challenges and opportunities. Curr Opin Solid State Mater Sci 21(4):198–206

67. (2023). Sub-projects structure. from https://www.for5134.science/en/teilprojekte/. Accessed 2023/10/03

68. Duggirala A, Kalvettukaran P, Acherjee B, Mitra S (2021) Numerical simulation of the temperature field, weld profile, and weld pool dynamics in laser welding of aluminium alloy. Optik 247:167990

69. Faraji AH, Maletta C, Barbieri G, Cognini F, Bruno L (2021) Numerical modeling of fluid flow, heat, and mass transfer for similar and dissimilar laser welding of Ti-6Al-4V and Inconel 718. Int J Adv Manuf Technol 114(3):899–914

70. Sun J, Liu X, Tong Y, Deng D (2014) A comparative study on welding temperature fields, residual stress distributions and deformations induced by laser beam welding and CO_2 gas arc welding. Mater Des 63:519–530

71. Gobbi C (2016) Low cost thermal imaging system for welding applications. University of Waterloo, Master of Applied Science

72. Mi G, Xiong L, Wang C, Hu X, Wei Y (2016) A thermal-metallurgical-mechanical model for laser welding Q235 steel. J Mater Process Technol 238:39–48

73. Gao Z, Jiang P, Mi G, Cao L, Liu W (2018) Investigation on the weld bead profile transformation with the keyhole and molten pool dynamic behavior simulation in high power laser welding. Int J Heat Mass Transf 116:1304–1313

74. Chen L, Mi G, Zhang X, Wang C (2019) Numerical and experimental investigation on microstructure and residual stress of multi-pass hybrid laser-arc welded 316L steel. Mater Des 168:107653

75. Assuncao E, Williams S, Yapp D (2012) Interaction time and beam diameter effects on the conduction mode limit. Opt Lasers Eng 50(6):823–828

76. Assuncao E, Williams S (2014) Effect of material properties on the laser welding mode limits. J Laser Appl 26(1):012008

77. Farrokhi F, Endelt B, Kristiansen M (2019) A numerical model for full and partial penetration hybrid laser welding of thick-section steels. Opt Laser Technol 111:671–686

78. Wiklund, G., Akselsen, O., Sørgjerd, A.J. and Kaplan, A.F., 2014. Geometrical aspects of hot cracks in laser-arc hybrid welding. J Laser Appl 26(1)

79. Kristiansen M, Farrokhi F, Kristiansen E, Villumsen S (2017) Application of hybrid laser arc welding for the joining of large offshore steel foundations. Phys Procedia 89:197–204

80. Farrokhi F, Nielsen SE, Schmidt R, Pedersen S, Kristiansen M (2015) Effect of cut quality on hybrid laser arc welding of thick section steels. Phys Procedia 78:65–73

81. Bunaziv I, Frostevarg J, Akselsen OM, Kaplan AF (2018) Process stability during fiber laser-arc hybrid welding of thick steel plates. Opt Lasers Eng 102:34–44

82. Reisgen U, Olschok S, Weinbach M, Engels O (2017). Welding of high thickness steel plates using a fiber coupled diode laser with 50 kW of output power. Lasers Manuf Conf, München, Germany.

83. Pan Q, Mizutani M, Kawahito Y, Katayama S (2016) High power disk laser-metal active gas arc hybrid welding of thick high tensile strength steel plates. J Laser Appl 28(1):012004

84. Gebhardt MO, Gumenyuk A, Quiroz Penaranda V, Rethmeier M (2012) Laser/GMA hybrid welding of thick-walled precision pipes. Weld Cut 11(5):312–318

85. Cao X, Wanjara P, Huang J, Munro C, Nolting A (2011) Hybrid fiber laser–Arc welding of thick section high strength low alloy steel. Mater Des 32(6):3399–3413

86. Farrokhi F, Larsen RM, Kristiansen M (2017) Single-pass hybrid laser welding of 25 mm thick steel. Phys Procedia 89:49–57

87. Vollertsen F, GrÜnenwald S, Rethmeier M, Gumenyuk A, Reisgen U, Olschok S (2010) Welding thick steel plates with fibre lasers and GMAW. Weld World 54(3):R62–R70

88. Rethmeier M, Gook S, Lammers M, Gumenyuk A (2009) Laser-hybrid welding of thick plates up to 32 mm using a 20 kW fibre laser. Quart J Jpn Weld Soc 27(2):74s–79s

89. Li G, Zhang C, Gao M, Zeng X (2014) Role of arc mode in laser-metal active gas hybrid welding of mild steel. Mater Des 61:239–250

90. Morgan S, and S Williams (2002). Hybrid laser conduction welding. 55th Annual Assembly of International Institute of Welding

91. Kawahito Y, Mizutani M, Katayama S (2009) High quality welding of stainless steel with 10 kW high power fibre laser. Sci Technol Weld Joining 14(4):288–294

92. Ramasamy S, Albright C (2001) CO_2 and Nd–YAG laser beam welding of 5754–O aluminium alloy for automotive applications. Sci Technol Weld Join 6(3):182–190

93. Steen WM, Mazumder J (2010). Laser material processing, springer science & business media

94. Xie X, Zhou J, Long J (2021) Numerical study on molten pool dynamics and solute distribution in laser deep penetration welding of steel and aluminum. Opt Laser Technol 140:107085

95. Yuce C, Karpat F, Yavuz N (2019) Investigations on the microstructure and mechanical properties of laser welded dissimilar galvanized steel–aluminum joints. Int J Adv Manuf Technol 104(5):2693–2704

96. Wang Y, Jiang P, Zhao J, Geng S (2021) Effects of energy density attenuation on the stability of keyhole and molten pool during deep penetration laser welding process: A combined numerical and experimental study. Int J Heat Mass Transf 176:121410

97. Unni AK, Muthukumaran V (2022) Modeling of heat transfer, fluid flow, and weld pool dynamics during keyhole laser welding of 316 LN stainless steel using hybrid conical-cylindrical heat source. Int J Adv Manuf Technol 122(9):3623–3645

98. Zhang L, Zhang J, Zhang G, Bo W, Gong S (2011) An investigation on the effects of side assisting gas flow and metallic vapour jet on the stability of keyhole and molten pool during laser full-penetration welding. J Phys D Appl Phys 44(13):135201

99. Tenner F, Brock C, Gürtler F-J, Klämpfl F, Schmidt M (2014) Experimental and numerical analysis of gas dynamics in the keyhole during laser metal welding. Phys Procedia 56:1268–1276

100. Lankalapalli KN, Tu JF, Gartner M (1996) A model for estimating penetration depth of laser welding processes. J Phys D Appl Phys 29(7):1831

101. Lampa C, Kaplan AF, Powell J, Magnusson C (1997) An analytical thermodynamic model of laser welding. J Phys D Appl Phys 30(9):1293

102. Lankalapalli KN, Tu JF, Leong KH, Gartner M (1999). Laser weld penetration estimation using temperature measurements

103. Tsai F-R, Kannatey-Asibu E Jr (2000) Modeling of conduction mode laser welding process for feedback control. J Manuf Sci Eng 122(3):420–428

104. Zhao H, DebRoy T (2001) Weld metal composition change during conduction mode laser welding of aluminum alloy 5182. Metall and Mater Trans B 32(1):163–172

105. Park YW, Park H, Rhee S, Kang M (2002) Real time estimation of CO2 laser weld quality for automotive industry. Opt Laser Technol 34(2):135–142

106. Casalino G, Minutolo FMC (2004) A model for evaluation of laser welding efficiency and quality using an artificial neural network and fuzzy logic. Proc Inst Mech Eng, Part B: J Eng Manuf 218(6):641–646

107. Du H, Hu L, Liu J, Hu X (2004) A study on the metal flow in full penetration laser beam welding for titanium alloy. Comput Mater Sci 29(4):419–427

108. Benyounis K, Olabi A, Hashmi M (2005) Effect of laser welding parameters on the heat input and weld-bead profile. J Mater Process Technol 164:978–985

109. Balasubramanian K, Buvanashekaran G, Sankaranarayanasamy K (2010) Modeling of laser beam welding of stainless steel sheet butt joint using neural networks. CIRP J Manuf Sci Technol 3(1):80–84

110. Hann DB, Iammi J, Folkes J (2010). Keyholing or conduction–prediction of laser penetration depth. Proceedings of the 36th International MATADOR Conference, Springer

111. Tobar M, Lamas M, Yáñez A, Sánchez-Amaya J, Boukha Z, Botana F (2010) Experimental and simulation studies on laser conduction welding of AA5083 aluminium alloys. Phys Procedia 5:299–308

112. Hann D, Iammi J, Folkes J (2011) A simple methodology for predicting laser-weld properties from material and laser parameters. J Phys D Appl Phys 44(44):445401

113. Luo M, Shin YC (2015) Estimation of keyhole geometry and prediction of welding defects during laser welding based on a vision system and a radial basis function neural network. Int J Adv Manuf Technol 81(1):263–276

114. Zhang Y, Gao X, Katayama S (2015) Weld appearance prediction with BP neural network improved by genetic algorithm during disk laser welding. J Manuf Syst 34:53–59

115. Petković D (2017) Prediction of laser welding quality by computational intelligence approaches. Optik 140:597–600

116. Artinov A, Bachmann M, Rethmeier M (2018) Equivalent heat source approach in a 3D transient heat transfer simulation of full-penetration high power laser beam welding of thick metal plates. Int J Heat Mass Transf 122:1003–1013

117. Rong Y, Mi G, Xu J, Huang Y, Wang C (2018) Laser penetration welding of ship steel EH36: a new heat source and application to predict residual stress considering martensite phase transformation. Mar Struct 61:256–267

118. Lei Z, Shen J, Wang Q, Chen Y (2019) Real-time weld geometry prediction based on multi-information using neural network optimized by PCA and GA during thin-plate laser welding. J Manuf Process 43:207–217

119. Liu B, Jin W, Lu A, Liu K, Wang C, Mi G (2020) Optimal design for dual laser beam butt welding process parameter using artificial neural networks and genetic algorithm for SUS316L austenitic stainless steel. Opt Laser Technol 125:106027

120. Li Z, Rostam K, Panjehpour A, Akbari M, Karimipour A, Rostami S (2020) Experimental and numerical study of temperature field and molten pool dimensions in dissimilar thickness laser welding of Ti6Al4V alloy. J Manuf Process 49:438–446

121. Khan MS, Shahabad S, Yavuz M, Duley W, Biro E, Zhou Y (2021) Numerical modelling and experimental validation of the effect of laser beam defocusing on process optimization during fiber laser welding of automotive press-hardened steels. J Manuf Process 67:535–544

122. Le-Quang T, Faivre N, Vakili-Farahani F, Wasmer K (2021) Energy-efficient laser welding with beam oscillating technique–A parametric study. J Clean Prod 313:127796

123. Nabavi SF, Farshidianfar MH, Farshidianfar A, Beidokhti B (2021) Physical-based methodology for prediction of weld bead characteristics in the laser edge welding process. Optik 241:166917

124. Liu Z, Jin X, Li J, Hao Z, Zhang J (2022) Numerical simulation and experimental analysis on the deformation and residual stress in trailing ultrasonic vibration assisted laser welding. Adv Eng Softw 172:103200

125. Busto V, Coviello D, Lombardi A, De Vito M, Sorgente D (2022) Thermal finite element modeling of the laser beam welding of tailor welded blanks through an equivalent volumetric heat source. Int J Adv Manuf Technol 119(1):137–148

126. Jia Y, Saadlaoui Y, Hamdi H, Sijobert J, Roux J-C, Bergheau J-M (2022) An experimental and numerical case study of thermal and mechanical consequences induced by laser welding process. Case Stud Therm Eng 35:102078

127. Dave F, Ali MM, Mokhtari M, Sherlock R, McIlhagger A, Tormey D (2022) Effect of laser processing parameters and carbon black on morphological and mechanical properties of welded polypropylene. Opt Laser Technol 153:108216

128. Fan X, Qin G, Jiang Z, Wang H (2023) Comparative analysis between the laser beam welding and low current pulsed GMA assisted high-power laser welding by numerical simulation. J Mater Res Technol 22:2549–2565

129. Ke W, Zeng Z, Oliveira J, Peng B, Shen J, Tan C, Song X, Yan W (2023) Heat transfer and melt flow of keyhole, transition and conduction modes in laser beam oscillating welding. Int J Heat Mass Transf 203:123821

130. Tan C, Liu Y, Xu B, Wang H, Liu F, Gong X, Zeng Z, Chen B, Song X (2023) Numerical and experimental study of thermal fluid flow and keyhole dynamic in laser welding of aluminum alloy assisted by electromagnetic field. Opt Laser Technol 157:108718

131. Zhao J, Wang J, Kang X, Wang X, Zhan X (2023) Effect of beam oscillation and oscillating frequency induced heat accumulation on microstructure and mechanical property in laser welding of Invar alloy. Opt Laser Technol 158:108831

132. Lu Y, Deng Y, Shi L, Jiang L, Gao M (2023) Numerical simulation of thermal flow dynamics in oscillating laser welding of aluminum alloy. Opt Laser Technol 159:109003

133. Tien NT, Lo Y-L, Raza MM, Chen C-Y, Chiu C-P (2023) Optimization of processing parameters for pulsed laser welding of dissimilar metal interconnects. Opt Laser Technol 159:109022

134. Zhao X, Chen J, Zhang W, Chen H (2023) A study on weld morphology and periodic characteristics evolution of circular oscillating laser beam welding of SUS301L-HT stainless steel. Opt Laser Technol 159:109030

135. Surwase SS, Bhosle SP (2023). Investigating the effect of residual stresses and distortion of laser welded joints for automobile chassis and optimizing weld parameters using random forest based grey wolf optimizer. Weld Int. 1–22

136. Huang H, Tsutsumi S, Wang J, Li L, Murakawa H (2017) High performance computation of residual stress and distortion in laser welded 301L stainless sheets. Finite Elem Anal Des 135:1–10

137. Murakawa H, Deng D, Ma N (2010) Concept of inherent strain, inherent stress, inherent deformation and inherent force for prediction of welding distortion and residual stress. Trans JWRI 39(2):103–105

138. Kim JW, Jang BS, Kim YT, San Chun K (2013) A study on an efficient prediction of welding deformation for T-joint laser welding of sandwich panel PART I: proposal of a heat source model. Int J Naval Arch Ocean Eng 5(3):348–363

139. Rong Y, Huang Y, Zhang G, Mi G, Shao W (2017) Laser beam welding of 316L T-joint: microstructure, microhardness, distortion, and residual stress. Int J Adv Manuf Technol 90(5):2263–2270

140. Rong Y, Zhang G, Huang Y (2017) Study on deformation and residual stress of laser welding 316L T-joint using 3D/shell finite element analysis and experiment verification. Int J Adv Manuf Technol 89:2077–2085

141. Huang H, Wang J, Li L, Ma N (2016) Prediction of laser welding induced deformation in thin sheets by efficient numerical modeling. J Mater Process Technol 227:117–128

142. Xu J, Chen C, Lei T, Wang W, Rong Y (2019) Inhomogeneous thermal-mechanical analysis of 316L butt joint in laser welding. Opt Laser Technol 115:71–80

143. Evdokimov A, Doynov N, Ossenbrink R, Obrosov A, Weiß S, Michailov V (2021) Thermomechanical laser welding simulation of dissimilar steel-aluminum overlap joints. Int J Mech Sci 190:106019

144. Ragavendran M, Vasudevan M (2021) Effect of laser and hybrid laser welding processes on the residual stresses and distortion in AISI type 316L (N) stainless steel weld joints. Metall Mater Trans B 52(4):2582–2603

145. Barat K, Kumar CN, Patil G, Panbarasu K, Venkateswarlu K (2023) Defectometry, distortion analysis and metallurgical properties in the keyhole and conduction mode of laser beam welding of Al–Mg–Sc alloy butt joints. Opt Laser Technol 162:109248

146. Bodaghi F, Movahedi M, Kokabi A (2023) Estimation of solidification cracking susceptibility in Al–Si–Cu alloy weld: effects of anisotropic permeability and deformation orientation. J Market Res 23:2351–2361

147. Kou S (2003) Solidification and liquation cracking issues in welding. Jom 55:37–42

148. Liu J, Rao Z, Liao S, Wang P-C (2014) Modeling of transport phenomena and solidification cracking in laser spot bead-on-plate welding of AA6063-T6 alloy. Part II—simulation results and experimental validation. Int J Adv Manuf Technol 74:285–296

149. Soysal T, Kou S (2020) Role of liquid backfilling in reducing solidification cracking in aluminium welds. Sci Technol Weld Join 25(5):415–421

150. Wang L, Gao M, Zhang C, Zeng X (2016) Effect of beam oscillating pattern on weld characterization of laser welding of AA6061-T6 aluminum alloy. Mater Des 108:707–717

151. Balasubramanian K, Raghavendran S, Balusamy V (2011) Studies on the effect of mechanical vibration on the microstructure of the weld metal. Int J Tech Eng Syst 2(3):253–256

152. Kurz W, Fisher D (1981) Dendrite growth at the limit of stability: tip radius and spacing. Acta Metall 29(1):11–20

153. Du Z, Sun X, Ng FL, Chew Y, Tan C, Bi G (2021) Thermo-metallurgical simulation and performance evaluation of hybrid laser arc welding of chromium-molybdenum steel. Mater Des 210:110029

154. Han SW, Cho WI, Zhang LJ, Na SJ (2021) Coupled simulation of thermal-metallurgical-mechanical behavior in laser keyhole welding of AH36 steel. Mater Des 212:110275

155. Tan W, Bailey NS, Shin YC (2011) A novel integrated model combining cellular automata and phase field methods for microstructure evolution during solidification of multi-component and multi-phase alloys. Comput Mater Sci 50(9):2573–2585

156. Wang L, Wei Y, Zhan X, Yu F, Cao X, Gu C, Ou W (2017) Simulation of dendrite growth in the laser welding pool of aluminum alloy 2024 under transient conditions. J Mater Process Technol 246:22–29

157. Geng S, Jiang P, Ai Y, Chen R, Cao L, Han C, Liu W, Liu Y (2018) Cellular automaton modeling for dendritic growth during laser beam welding solidification process. J Laser Appl 30(3):032406

158. Lingda X, Guoli Z, Gaoyang M, Chunming W, Ping J (2021) A phase-field simulation of columnar-to-equiaxed transition in the entire laser welding molten pool. J Alloy Compd 858:157669

159. Ren Y, Lin X, Fu X, Tan H, Chen J, Huang W (2017) Microstructure and deformation behavior of Ti-6Al-4V alloy by high-power laser solid forming. Acta Mater 132:82–95

160. Benyounis KY, Olabi AG, Hashmi MSJ (2008) Multi-response optimization of CO2 laser-welding process of austenitic stainless steel. Opt Laser Technol 40(1):76–87

161. Chen L, Yang T, Zhuang Y, Chen W (2021) The multi-objective optimization modelling for properties of 301 stainless steel welding joints in ultra-narrow gap laser welding. Weld World 65:1333–1345

162. Li Y, Xiong M, He Y, Xiong J, Tian X, Mativenga P (2022) Multi-objective optimization of laser welding process parameters: the trade-offs between energy consumption and welding quality. Opt Laser Technol 149:107861

163. Park YW, Rhee S (2008) Process modeling and parameter optimization using neural network and genetic algorithms for aluminum laser welding automation. Int J Adv Manuf Technol 37(9):1014–1021

164. Banerjee N, Biswas A, Kumar M, Sen A, Maity S (2022) Modeling of laser welding of stainless 1679 steel using artificial neural networks. Materials Today: Proceedings

165. Hall E (1951) The deformation and ageing of mild steel: III discussion of results. Proc Phys Soc. Sect B 64(9):747

166. Rodrıguez R, Gutierrez I (2003) Correlation between nanoindentation and tensile properties: influence of the indentation size effect. Mater Sci Eng, A 361(1–2):377–384

167. Tiryakioğlu M (2015) On the relationship between Vickers hardness and yield stress in Al–Zn–Mg–Cu Alloys. Mater Sci Eng, A 633:17–19

168. Tiryakioğlu M, Robinson J, Salazar-Guapuriche M, Zhao Y, Eason P (2015) Hardness–strength relationships in the aluminum alloy 7010. Mater Sci Eng, A 631:196–200

169. Zou J, Han J, Yang W (2020) Investigating the influences of indentation hardness and brittleness of rock-like material on its mechanical crushing behaviors. Math Probl Eng 2020:1–16

170. Zhou J, Mandal S, Chen F, Quest M, Hume D (2018). Reservoir geomechanic heterogeneity index (RGHI): Concept, methodology, and application. SPE/AAPG/SEG Unconv Resourc Technol Conf, OnePetro

171. Zoeram AS, Mousavi SA (2014) Laser welding of Ti–6Al–4V to nitinol. Mater Des 61:185–190

172. Sines G, Carlson R (1952) Hardness measurements for determination of residual stresses. ASTM Bull 180:35–37

173. Tsui T, Oliver W, Pharr G (1996) Influences of stress on the measurement of mechanical properties using nanoindentation: part I, Experimental studies in an aluminum alloy. J Mater Res 11(3):752–759

174. Bolshakov A, Oliver WC, Pharr GM (1996) Influences of stress on the measurement of mechanical properties using nanoindentation: part II. Finite element simulations. J Mater Res 11(3):760–768

175. Khan M, Fitzpatrick M, Hainsworth S, Edwards L (2011) Effect of residual stress on the nanoindentation response of aerospace aluminium alloys. Comput Mater Sci 50(10):2967–2976

176. Huber N, Heerens J (2008) On the effect of a general residual stress state on indentation and hardness testing. Acta Mater 56(20):6205–6213

177. Sabokrouh M, Farahani M (2019) Correlation between the weld residual stresses and its tensile and impact strength. J Appl Comput Mech 5(4):727–734

178. Farahani M, Sattari-Far I, Akbari D, Alderliesten R (2012) Numerical and experimental investigations of effects of residual stresses on crack behavior in Aluminum 6082–T6. Proc Inst Mech Eng C J Mech Eng Sci 226(9):2178–2191

179. Farahani M, Sattari-Far I (2011) Effects of residual stresses on crack-tip constraints. Scientia Iranica 18(6):1267–1276

180. Francis J, Bhadeshia H, Withers P (2007) Welding residual stresses in ferritic power plant steels. Mater Sci Technol 23(9):1009–1020

181. Zargar SH, Farahani M, Givi MKB (2016) Numerical and experimental investigation on the effects of submerged arc welding sequence on the residual distortion of the fillet welded plates. Proc Ins Mech Eng, Part B: J Eng Manuf 230(4):654–661

182. Ueda Y, Yamakawa T (1971). Analysis of thermal elastic-plastic stress and strain during welding by finite element method. Japan Welding Society Transactions 2(2)

183. Hibbitt HD, Marcal PV (1973) A numerical, thermo-mechanical model for the welding and subsequent loading of a fabricated structure. Comput Struct 3(5):1145–1174

184. Zhang Y, Su W, Dong H, Li T, Cao H (2022). Effect of welding sequence and constraint on the residual stress and deformation of thick welded butt joint made of Q345qD steel. Adv Civil Eng 2022

185. Prevey PS (1986) X-ray diffraction residual stress techniques. ASM Int, ASM Handbook 10:380–392

186. Deng D (2009) FEM prediction of welding residual stress and distortion in carbon steel considering phase transformation effects. Mater Des 30(2):359–366

187. Rong Y, Huang Y, Xu J, Zheng H, Zhang G (2017) Numerical simulation and experiment analysis of angular distortion and residual stress in hybrid laser-magnetic welding. J Mater Process Technol 245:270–277

188. Vemanaboina H, Babu MM, Prerana IC, Gundabattini E, Yelamasetti B, Saxena KK, Salem KH, Khan MI, Eldin SM, Agrawal MK (2023). Evaluation of residual stresses in CO2 laser beam welding of SS316L weldments using FEA. Mater Res Exp

189. Moglia F, Raspa A (2020) New Trends in Laser Beam Welding: How automotive applications are driving the future of laser technologies. Photonics Views 17(5):26–29

190. Mo T, Li Y, Lau K-T, Poon CK, Wu Y, Luo Y (2022) Trends and emerging technologies for the development of electric vehicles. Energies 15(17):6271